



## 저작자표시-비영리-변경금지 2.0 대한민국

이용자는 아래의 조건을 따르는 경우에 한하여 자유롭게

- 이 저작물을 복제, 배포, 전송, 전시, 공연 및 방송할 수 있습니다.

다음과 같은 조건을 따라야 합니다:



저작자표시. 귀하는 원저작자를 표시하여야 합니다.



비영리. 귀하는 이 저작물을 영리 목적으로 이용할 수 없습니다.



변경금지. 귀하는 이 저작물을 개작, 변형 또는 가공할 수 없습니다.

- 귀하는, 이 저작물의 재이용이나 배포의 경우, 이 저작물에 적용된 이용허락조건을 명확하게 나타내어야 합니다.
- 저작권자로부터 별도의 허가를 받으면 이러한 조건들은 적용되지 않습니다.

저작권법에 따른 이용자의 권리는 위의 내용에 의하여 영향을 받지 않습니다.

이것은 [이용허락규약\(Legal Code\)](#)을 이해하기 쉽게 요약한 것입니다.

[Disclaimer](#)

**Ph.D. Dissertation of engineering**

**Ultra-Flexible Piezoelectric  
Nanogenerator and Mechanical Bending  
Sensor Using Solution Processed ZnO  
Nanomaterials**

**용액공정으로 제작한 산화아연 나노물질 기반  
초유연 압전 나노발전기 및 기계적 벤딩 센서**

**December 2016**

**Program in Nano Science and Technology  
Graduate School of Convergence Science and  
Technology, Seoul National University**

**Sung Yun Chung**

**Ultra-Flexible Piezoelectric  
Nanogenerator and Mechanical Bending Sensor  
Using Solution Processed ZnO Nanomaterials**

**Supervisor Youn Sang Kim**

**Submitting a Ph.D. Dissertation of Public Administration**

**Decemeber 2016**

**Program in Nano Science and Technology  
Graduate School of Convergence Science and Technology, Seoul  
National University**

**Sung Yun Chung**

**Confirming the Ph.D. Dissertation written by  
Sung Yun Chung**

**December 2016**

**Chair                      박 원 철                      (seal)**

**Vice Chair              김 연 상                      (seal)**

**Examiner                송 윤 규                      (seal)**

**Examiner                이 태 일                      (seal)**

**Examiner                강 종 윤                      (seal)**

## **Abstract**

# **Ultra-Flexible Piezoelectric Nanogenerator and Mechanical Bending Sensor Using Solution Processed ZnO Nanomaterials**

Sung Yun Chung

Program in Nano Science and Technology

The Graduate School

Seoul National University

With world-wide crisis of energy resources depletion and global warming, exploring of renewable ‘green’ energy matches the upsurge of interest in scientific fields. On the larger scale, petroleum, coal, natural gas, hydroelectric and nuclear are the well-known current world energy resources, which are now in mortal danger for their shortage. However, development of alternative energy such as solar, wind, geothermal, hydrogen, and biomass has recently been flourished. However, on the smaller scale, requiring the entire packages in nanometer scale, the nano energy system is applicable to personal mobile electronics, micro-



electromechanical systems, nanorobotics, and body implantable devices. For portable, light-weighted device as well as persistent use without batteries, self-powered system should be adopted in a field of energy harvesting and sensing technologies. In this regard, piezoelectric nano-elements can be a fundamental solution to offer self-powered active system for driving wireless and mobile electronics.

Piezoelectric nanodevice that converts mechanical energy into electricity is emerging field in recent energy researches because of availability of destroyed energy from ambient environment. Adopting this piezoelectric energy conversion theorem is promising for power generation in new method form for the future. The first piezoelectric nanogenerator was invented by Z. L. Wang et al., which was demonstrated using ZnO nanowire array in 2006. ZnO is particularly appealing material because of its coupling effect of piezoelectric and semiconducting properties, high elasticity, abundant configurations of nanostructure, transparency, and biocompatibility. However, ZnO nanomaterials are mostly synthesized via vapor liquid solid method or sputtering with vacuum process, which requires high cost and complex equipment system. Solution process of ZnO nanomaterials has advantages for simple and low cost, and also can be deposited over a large area with mass production. In this point of view, I demonstrated piezoelectric nanodevices with solution processed ZnO nanomaterials and analyzed the output performance as well as the mechanism of the piezoelectric phenomena.

Firstly, using solution-processed ZnO thin film, an ultra-flexible piezoelectric patch-shaped nanogenerator was demonstrated for use as embedded muscle or cloths scavengers. The entire process of the patch, also called as nanogenerator, was conducted by solution process including piezoelectric active material,

electrodes, and p-type polymer blend for efficient piezoelectric energy generation. The highly elastic thin film nanogenerator allowed piezoelectric energy generation through mechanical rolling and muscles stretching of human arms.

Secondly, using solution-processed ZnO nanorods, a piezoelectric bending motion sensor was developed for simultaneous recognition of bending curvature and speed with systematic analysis based on a database of output performance with statistical measurement. For bendability, a polydimethylsiloxane sandwiched ZnO nanorods layer was adapted as well as hybrid electrode of flexible Ag nanowire and single-wall carbon nanotubes. This highly bendable piezoelectric bending motion sensor is expectable for the realization of artificial skin, wearable electronics, and biomimetic robot system.

In summary, via solution processing of ZnO nanomaterials, piezoelectric active material was synthesized and applied to ultra-flexible nanogenerator and sensor to fabricate piezoelectric nanodevices for versatile, cost-effective system. These piezoelectric nanodevices have potential to be integrated into multi-functional nanosystem with self-powered capability.

주요어: zinc oxide (ZnO), solution process, piezoelectric nanogenerator, piezoelectric sensor, ultra-flexible, ZnO thin film, ZnO nanorods, all-solution-process, bending motion sensing.

학 번 : 2010-22677

# Contents

|   |             |
|---|-------------|
| <b>Abstract .....</b>                                     | <b>I</b>    |
| <b>Contents .....</b>                                     | <b>IV</b>   |
| <b>List of tables and figures .....</b>                   | <b>VII</b>  |
| <b>Abbreviations .....</b>                                | <b>XVII</b> |
| <br>  |             |
| <b>Chapter 1. Introduction .....</b>                      | <b>1</b>    |
| 1.1 References .....                                      | 8           |
| <br>  |             |
| <b>Chapter 2. Literature review and theories .....</b>    | <b>9</b>    |
| 2.1 Introduction of piezoelectricity .....                | 9           |
| 2.1.1 Direct/converse piezoelectric effect... ..          | 12          |
| 2.1.2 Poling and hysteresis curve for polarization .....  | 19          |
| 2.1.3 Piezoelectric constants .....                       | 25          |
| 2.1.4 Piezoelectric materials.....                        | 32          |
| 2.1.4.1 Perovskite materials .....                        | 34          |
| 2.1.4.2 Wurtzite materials .....                          | 35          |
| 2.1.4.3 Quartz .....                                      | 36          |
| 2.1.4.4 Polymer based materials.....                      | 36          |
| 2.2 ZnO.....  | 40          |
| 2.2.1 Piezoelectric properties of ZnO nanomaterials ..... | 43          |
| 2.2.2 Synthesis of ZnO nanomaterials .....                | 48          |
| 2.2.2.1 ZnO thin film.....                                | 51          |

|   |    |
|---|----|
| 2.2.2.2 ZnO nanorods .....                    | 53 |
| 2.3 Piezoelectric devices.....                | 61 |
| 2.3.1 Principle of piezoelectric devices..... | 61 |
| 2.3.2 Types of piezoelectric devices .....    | 64 |
| 2.3.2.1 Nanogenerators.....                   | 64 |
| 2.3.2.2 Sensors .....                         | 69 |
| 2.4 References .....                          | 71 |

## **Chapter 3. ZnO thin film piezoelectric nanogenerator ..... 75**

|  |     |
|--|-----|
| 3.1 Introduction .....   | 75  |
| 3.2 Experimental .....   | 78  |
| 3.2.1 Preparation of ZnO thin film.....  | 78  |
| 3.2.2 Fabrication of ZnO thin film piezoelectric nanogenerator.....            | 81  |
| 3.2.3 Characterizations.....   | 81  |
| 3.3 Results and discussion.....  | 84  |
| 3.3.1 Characteristics of ZnO thin film.....                                    | 84  |
| 3.3.2 Output performance of ZnO thin film piezoelectric<br>nanogenerator ..... | 94  |
| 3.3.3 Operation mechanism.....   | 102 |
| 3.3.4 Stability and muscle-driven test .....                                   | 106 |
| 3.4 References.....  | 109 |

## **Chapter 4. ZnO nanorod piezoelectirc bending motion sensor ..... 111**

|  |     |
|--|-----|
| 4.1 Introduction .....   | 111 |
| 4.2 Experimental .....   | 112 |
| 4.2.1 Synthesis of bi-axially grown ZnO nanorods.....          | 113 |
| 4.2.2 Fabrication of Ag NW-SWCNT electrodes .....              | 113 |
| 4.2.3 Fabrication of piezoelectric bending motion sensor ..... | 116 |
| 4.2.4 Characterizations .....                                  | 116 |
| 4.3 Results and discussion.....                                | 118 |
| 4.3.1 Chracterstics of bi-axially grown ZnO nanorods .....     | 118 |
| 4.3.2 Characteristics of hybrid Ag NW-SWCNT .....              | 126 |
| 4.3.3 Measurement of output voltage signals.....               | 135 |
| 4.3.4 Output analysis based on piezoelectric effect .....      | 144 |
| 4.3.5 Sensing of bending curvature and speed .....             | 147 |
| 4.4 References .....   | 151 |

## **Chapter 5. Conclusion ..... 153**

## **초록(국문) ..... 155**

## List of tables and figures

**Table 1** Application of direct/converse piezoelectric effect.

**Table 2** Piezoelectric constants expressing the piezoelectric properties.

**Table 3** Piezoelectric materials and their properties.

**Figure 1.1** Needs for personal/mobile electronics (*from Ref. [55] Copyright 2012 Wiley Publishing Group*). (b) Output powers for wireless electronics (*from Ref. [56] Copyright 2015 Elsevier Publishing Group*). (c) Global market for energy harvesting forecast (*from Intech, 2013*)

**Figure 1.2** Perspectives of piezoelectric devices for potential future applications (*from Ref. [57] Copyright 2008 Wiley Publishing Group*) .

**Figure 1.3** Future perspective of electronics for nanodevice and nanosystem for multi-functionalities (*from Ref. [55] Copyright 2012 Wiley Publishing Group*).

**Figure 2.1** Induced charges in quartz crystal under mechanical compressive and/or tensile stress along the electrical  $X_1$  axis (*from Ref. [3], Copyright 2013 IOPscience Publishing Group*).

**Figure 2.2** Net balance of electric charge in crystal as a result of application of mechanical stress.

**Figure 2.3** Schematic image of direct piezoelectric effect. (a) Piezoelectric material after poling process. (b) Piezoelectric material under tension, and (c) compression (*from Ref. [5], Copyright 2012 Intech Publishing Group*).

**Figure 2.4** Schematic image of converse piezoelectric effect. (a) Piezoelectric material after poling process. (b) Piezoelectric material when a voltage of the same polarity of the poling voltage is applied, and (c) piezoelectric material when a

voltage of the opposite polarity of the poling voltage is applied (*from Ref. [5], Copyright 2012 Intech Publishing Group*).

**Figure 2.5** Crystal structure of piezoelectric ceramics applied (a) temperature above the Curie point and (b) temperature below Curie point (*from Ref. [2], Copyright Intech Publishing Group*).

**Figure 2.6** Poling a piezoelectric ceramic (a) random orientation of polar domains prior to polarization, (b) polarization after application of an electric field, and (c) remnant polarization after removal of an electric field (*from Ref. [2], Copyright Intech Publishing Group*).

**Figure 2.7** (a) Typical polarization (P) – electric field (E) hysteresis plot showing the effect of an electric field on polarization and (b) strain versus electric field plot showing relative increase/decrease in dimension (strain) in direction of polarization (*from Ref. [2], Copyright Intech Publishing Group*).

**Figure 2.8** Direction of forces affecting a piezoelectric materials and examples of piezoelectric materials for definition of direction of polarization and mechanical stress (*from Ref. [2], Copyright Intech Publishing Group*).

**Figure 2.9** Illustration of -33 mode and -31 mode operation for piezoelectric materials (*from Ref. [7], Copyright 2012 SAGE Publishing Group*).

**Figure 2.10** The classification of crystal structures into piezoelectric, pyroelectrics, and ferroelectrics.

**Figure 2.11** Various piezoelectric materials including (a-b) perovskite materials, (c) wurtzite materials, (d) quartz, and (e) polymer based materials (*from Fujitsu, cea, Ref. [11], Copyright 2012 Nature Publishing Group, Book: The origin of Earth's Radioactivity, Ref. [13], Copyright 2015 Intech Publishing Group*).

**Figure 2.12** Various ZnO nanostructures grown in polar  $\pm$  (0001) surfaces (*from*

*Ref. [20] Copyright 2012 MRS Publishing Group).*

**Figure 2.13** Wurtzite structure of ZnO oriented along the [0001] direction. (b) Tetrahedral coordination between Zn and O atoms under no mechanical strain. (c) Distortion of the tetrahedral structure under compressive strain, showing the displacement of the positive and negative mass of center (*from Ref. [18] Copyright 2011 Springer Publishing Group*).

**Figure 2.14** (a) The piezoelectric coefficient ( $e_{33}$ ) of several perovskite and wurtzite materials as a function of cross thickness ( $t$ ) or diameter ( $d$ ) (*from Ref. [12] Copyright 2014 RSC Publishing Group*). (b) Experimentally measured piezoelectric coefficient ( $d_{33}$ ) for ZnO and its comparison to that of the bulk (*from Ref. [27] Copyright 2014 ACS Publishing Group*).

**Figure 2.15** (a-d) FE-SEM images of tensile test on a 20 nm-thick ZnO NWs. (e) A stress-strain response of the 20nm-thick ZnO NWs under repeated loading and unloading (*from Ref. [28] Copyright 2010 Springer Publishing Group*).

**Figure 2.16** (a-e) FE-SEM images of buckling test on 46 nm-thick ZnO NW (f) A plot of applied force versus axial displacement of ZnO nanowire (*from Ref. [28] Copyright 2010 Springer Publishing Group*).

**Figure 2.17** (a) ZnO-H<sub>2</sub>O system as a function of precursor concentration and pH. (b) Aggregation and nucleation of domains of the wurtzite structured ZnO (*from Ref. [18] Copyright 2011 Springer Publishing Group*).

**Figure 2.18** FE-SEM image of ink-jet printed ZnO thin film onto SiO<sub>2</sub> annealed at 150 °C (*from Ref. [36] Copyright 2008 ACS Publishing Group*).

**Figure 2.19** Schematic diagram of the kinetically controlled ZnO NRs synthesis system (*from Ref. [37] Copyright 2012 RSC Publishing Group*).

**Figure 2.20** Schematic diagram of ZnO NRs synthesis based on (a) one-pot heat-



up process and (b) kinetically controlled process by a syringe pump (*from Ref. [37]* Copyright 2012 RSC Publishing Group).

**Figure 2.21** FE-SEM images of ZnO NRs grown by (a) and (c) normal one-pot heat-up process and (b) and (d) kinetically controlled process. Size distribution of ZnO NRs using a kinetically controlled process with (e) 2.5mM and (f) 12.5mM chemical reagents concentration (zinc nitrate and HMTA) (*from Ref. [37]* Copyright 2012 RSC Publishing Group).

**Figure 2.22** Sequential steps for formation of ZnO NRs based on OA. (a) Zinc hydroxide complexes from zinc nitrate and HMTA, (b) Ellipsoidal ZnO NPs, (c) ZnO nanocrystal seed, (f) and (g) growth of ZnO nanocrystal by additional zinc hydroxide compounds, and (h) final ZnO NRs (*from Ref. [37]* Copyright 2012 RSC Publishing Group).

**Figure 2.23** Comparison of operational mechanism between piezoelectric devices based on Schottky contact structure and sandwich structure (*from Ref. [38]* Copyright 2015 Elsevier Publishing Group).

**Figure 2.24** Horizontal ZnO NW array based flexible PENGs. (a) PENG with single ZnO NW on a flexible substrate (*from Ref. [39]* Copyright 2009 Nature Publishing Group). (b) PENG with integration of lateral ZnO NW arrays (*from Ref. [40]* Copyright 2010 Nature Publishing Group). (c) PENG with randomly-laterally-aligned ZnO NWs (*from Ref. [41]* Copyright 2010 ACS Publishing Group). (d) PENG with rational unipolar assembly of conical ZnO NWs (*from Ref. [42]* Copyright 2010 ACS Publishing Group).

**Figure 2.25** Vertical ZnO NW array based flexible PENGs. (a) Fully rollable PENG based on grapheme substrate with vertical ZnO arrays (*from Ref. [43]* Copyright 2010 Wiley Publishing Group). (b) Super-flexible PENG based on

ultrathin Al foil with vertical ZnO NW arrays as an active deformation sensor (*from Ref. [44] Copyright 2011 ACS Publishing Group*). (c) PENG with randomly-laterally-aligned ZnO NWs. (d) High-output PENG made of a free cantilever beam with multi-stacked ZnO NW structure (*from Ref. [45] Copyright 2013 Wiley Publishing Group*).

**Figure 2.26** ZnO fiber based flexible PENGs. (a) PENG with radially coiled ZnO NWs around textile fibers (*from Ref. [46] Copyright 2008 Nature Publishing Group*). (b) hybrid-fiber PENG consists of ZnO NWs and PVDF film for use as a human elbow patch (*from Ref. [47] Copyright 2012 Wiley Publishing Group*). (d) PENG with ZnO thin film arrays on the surface of carbon fiber (*from Ref. [48] Copyright 2011 Wiley Publishing Group*).

**Figure 2.27** Various piezoelectric sensors using diverse piezoelectric nanomaterials such as (a) pressure sensor (*from Ref. [49] Copyright 2014 Wiley Publishing Group*), (b) deformation sensor (*from Ref. [50] Copyright 2013 Wiley Publishing Group*), (c) transportation monitoring system (*from Ref. [51] Copyright 2013 Elsevier Publishing Group*), (d) biosensor (*from Ref. [52] Copyright 2014 Wiley Publishing Group*), (e) sound sensor (*from Ref. [53] Copyright 2015 Science Publishing Group*), and (f) climate sensor (*from Ref. [54] Copyright 2015 Wiley Publishing Group*).

**Figure 3.1** Fabrication process of the all-solution-processed flexible thin film PENG with an active area of  $0.8 \times 0.5 \text{ cm}^2$ . Further details of this fabrication process are written in the experimental section.

**Figure 3.2** Preparation of ZnO precursor and thin film.

**Figure 3.3** AFM images of (a-b) one-time and (c-d) two-times spin-coated ZnO thin films.

**Figure 3.4** A schematic diagram of the all-solution-processed flexible thin film PENG on a plastic substrate.

**Figure 3.5** Cross-sectional FE-SEM image of ITO-ZnO-P3HT/PCBM-PEDOT:PSS stacks.

**Figure 3.6** AFM images of the ZnO thin film on ITO/PET film. Average surface roughness ( $R_a$ ) is 1.47nm.

**Figure 3.7** The HRTEM image shows the deposition of the poly-crystalline ZnO nanostructure with the tendency for c-axis orientation with a (002) lattice plane.

**Figure 3.8** EDX spectrum acquired from the layer of ZnO thin film in figure 3.7.

**Figure 3.9** (a) The XRD pattern of ZnO deposited on ITO layer with annealing temperature of 120 °C (b) The GIXRD analysis at the ZnO deposited ITO layer with annealing temperature of 90 °C and 150 °C (black = 90 °C, red= 150 °C).

**Figure 3.10** One cycle of the rolling system went through three tighten (i-ii) – swap (iii-iv) – release (v-vi) steps with a mechanical rolling machine.

**Figure 3.11** Measured output voltage and current density of the all-solution-processed flexible thin film PENG from the mechanical rolling (a), (b).

**Figure 3.12** Measured output voltage and current density of the all-solution-processed flexible thin film PENG from the mechanical bending motions (a), (b).

**Figure 3.13** The PENG was in (a) forward (black in graph) and (b) reverse (red in graph) connections with the measurement instrument for the switching- polarity tests.

**Figure 3.14** (a) Schematic illustration of ZnO NG. (b) Measured output voltage from ZnO NG. (c) Schematic illustration of ZnO-P3HT/PCBM NG. (d) Measured output voltage from ZnO-P3HT/PCBM NG. (e) Schematic illustration of ZnO-P3HT/PCBM-PEDOT:PSS NG. (f) Measured output voltage from ZnO-

P3HT/PCBM-PEDOT:PSS NG.

**Figure 3.15** Operational mechanism of the PENG. Rolling motion of the PENG through the three tighten-swap-release steps. The as-fabricated thin film based PENG with (i) no force applied. (i-ii) Tighten step of the PENG through the rolling motion undergoes the electron -flow from the ITO electrode through the external circuit. (ii-iv) The swap step of the PENG through the rolling motion induces more electron-flow through the Schottky barrier. (iv-v) The release step of the PENG with electron-flow back to the ITO electrode to neutralize the current flow.

**Figure 3.16** Operational mechanism of the PENG. (b) Bending motion of the PENG with (i) static, (ii) bending and (iii) release steps. A small portion of electron-flow was induced from the bending step compared to swap step of the rolling motion.

**Figure 3.17** Long-term stability test to confirm the mechanical endurance of the PENG. (a) The output voltage and (b) current density for the period of 2000s (about 666times) operation of the PENG.

**Figure 3.18** (a) Measured output voltage from (b) the muscle-stretching of the PENG.

**Figure 4.1** A schematic procedure of the bi-axially grown ZnO NRs based piezoelectric bending motion sensor. (a) UVO treatment of PET substrate. (b) Spray-coating of Ag NW-SWCNT onto PET substrate. (c) Spin-coating of PDMS-hexane solution and post-annealing at 85 °C for 30 min. (d) Rubbing ZnO NR using a brush onto the PDMS layer. (e) The spin-coating and annealing process of PDMS-hexane. (f) The spray-coating of Ag NW-SWCNT electrode.

**Figure 4.2** (a) FE-SEM image of bi-axially grown ZnO NRs. (b) Photograph of rubbing process for ZnO deposition onto PDMS layer using a soft paint brush. (c)

Randomly rubbed bi-axially grown ZnO NRs onto PDMS layer.

**Figure 4.3** Piezoelectric potential simulation results of bi-axially grown ZnO NR  
(Reference: *Energy Environ. Sci.*, 2014, 7, 3994).

**Figure 4.4** Powder XRD pattern of bi-axially grown ZnO NRs.

**Figure 4.5** XPS spectra of (a) Zn-2p and (b) O-1s peaks.

**Figure 4.6** TGA-DSC curves of the ZnO NRs.

**Figure 4.7** Customized spray-coating setup for Ag NW-SWCNT composite film.

The Ag NW-SWCNT solution was injected at feeding rate of 0.2 ml/min with an air pressure of 2 bar onto the UVO-treated PET films for 5 min, annealing at 100 °C.

**Figure 4.8** 9:1, 8:2, 7:3 (g : g) of 0.05 wt% Ag NWs and g of 1.3 wt% SWCNT were mixed to investigate any deformation or cracks before and after mechanical bending. Optical microscope images of bottom electrodes according to the different weight ratio of Ag NW-SWCNT.

**Figure 4.9** 9:1, 8:2, 7:3 (g : g) of 0.05 wt% Ag NWs and g of 1.3 wt% SWCNT were mixed to investigate any deformation or cracks before and after mechanical bending. Optical microscope images of top electrodes according to the different weight ratio of Ag NW-SWCNT.

**Figure 4.10** (a) FE-SEM image of uniformly spray-coated Ag NW-SWCNT. (b) Magnified FE-SEM image of the Ag NW-SWCNT.

**Figure 4.11** (a) HRSTEM image of spray-coated Ag NW-SWCNT (b) The crsytalline lattice of Ag NW-SWCNT in its central region and (c) its FFT patterns.

**Figure 4.12** (a) Differently applied bending curvature. (b) Sheet resistance of top

and bottom electrodes as a function of bending curvature.

**Figure 4.13** (a) Standard output voltage. (b) Definition of a voltage area.

**Figure 4.14** The output voltages of the piezoelectric bending motion sensor with (b) different bending speed at constant bending curvature and with (c) different bending curvature at constant bending speed.

**Figure 4.15** The output voltages of the piezoelectric bending motion sensor with (b) different bending speed at constant bending curvature and with (c) different bending curvature at constant bending speed.

**Figure 4.16** Thickness of PDMS-ZnO NRs sandwiched structure with different weight ratio of 5:5, 6:4 and 7:3 of PDMS : hexane. Total thickness of the PDMS-ZnO NRs was 25.3, 32 and 39  $\mu\text{m}$  each.

**Figure 4.17** Thickness and voltage height of the piezoelectric bending motion sensor with different weight ratio (5:5, 6:4 and 7:3) of PDMS : hexane solution.

**Figure 4.18** The voltage area of the piezoelectric bending motion sensor measured at every 1000 times for 4000 times.

**Figure 4.19** The voltage area according to (d) the bending curvature and (e) rate ( $dR_c/dt$ ) according to the different bending speed and curvature.

**Figure 4.20** Diagram for detection of bending curvature and speed by measuring the voltage area from bending motion of the piezoelectric sensor.

**Figure 4.21** (a-c) Output voltages of the piezoelectric bending motion sensor by finger bending with various bending curvature and speed. Voltage areas according to (d) the bending curvature and (e) rate ( $dR_c/dt$ ) for detection of bending speed and curvature.

## Abbreviations

**MEMS** microelectromechanical systems

**PENG** piezoelectric generator

**ZnO** zinc oxide

**NW** nanowire

**NG** nanogenerator

**NR** nanorod

**PDMS** polydimethylsiloxane

**Ag NW-SWCNT** silver nanowire – single-wall carbon nanotube

**PZT** lead zirconate titanate

**BT** barium titanate

**GaN** gallium nitride

**CdS** cadmium sulfide

**P** polarization

**E** electric field

**S** strain

**PVDF** polyvinylidene fluoride

**MPB** morphotropic phase boundary

**PMN-PT** lead magnesium niobate-lead titanate

**InN** indium nitride

**ZnS** zinc sulfide

**T** trans

**G** gauche

**3D** three dimensional

**PFM** piezoresponse force microscopy

**AFM** atomic force microscope

**FE-SEM** field-emission scanning electron microscope

**KOH** potassium hydroxide

**NaOH** sodium hydroxide

**HMTA** hexamethylenetetramine

**OA** oriented aggregation

**PMMA** poly(methyl methacrylate)

**CNT** carbon nanotube

**Rf-sputtering** radio frequency magnetron sputtering

**ITO** indium tin oxide

**PET** polyethylene terephthalate

**P3HT** poly (3-hexylthiophene-2,5-diyl)

**PCBM** phenyl-C61-butyric acid methyl ester

**PEDOT:PSS** poly (3,4-ethylenedioxythiophene):poly (styrenesulfonate)

**DI** de-ionized

**HRSTEM** high resolution scanning transmission electron microscope

**EDX** energy dispersive X-ray spectrometer

**FFT** fast Fourier transform

**XRD** X-ray diffractometer

**GIXRD** grazing incidence X-ray diffraction

**AC** alternating-current

**UVO** ultraviolet ozone

**SDS** sodium dodecyl sulfonate

**MIM** metal insulator metal



**OM** optical microscope

**XPS** X-ray photoelectron spectrometry

**TGA** thermogravimetry

**DSC** differential scanning calorimeter

**RC** resistor-capacitor

# Chapter 1. Introduction

Recently, there are tremendous needs for personal and mobile electronics for applications in communication, health care and environmental monitoring (figure 1.1 (a)).<sup>1</sup> Individually, the power consumption is low (figure 1.1 (b)), however, demand for the number of such devices is huge. However, until today, power of these electronics is relied on recharging batteries.<sup>2</sup> The amount of batteries is required to be increased with rapid growth of the personal electronics and may result in challenges for recycling and even for replacement of the batteries. Thus, development of energy harvesting from our living environment such as solar energy, thermoelectricity and piezoelectricity has begun and the global market for piezoelectricity is forecasted to be brilliant in 2014-2024 as shown in figure 1.1 (c)).

The nano-piezoelectrics is new area of electronics for novel electronics device, which can be the future energy resources for applications in areas such as implantable devices, wireless sensors, nanorobots, nanosensors, MEMS and personal/mobile electronics as shown in figure 1.2.<sup>3</sup>

Future nanotechnology is likely focused on the integration of these individual nanodevices into a nanosystem with multiple functions such as sensing, communicating, controlling and responding abilities. Therefore, the goal of this nanosystem is to make a self-powered nanosystem with nanometer-scaled powered energy and extremely small entire package (figure 1.3).<sup>1,2</sup>

Elements based on piezoelectric transduction mechanism including piezoelectric nanogenerators, sensors, and actuators which use the conversion effect between mechanical stress and electric field is nowadays hot issue in scientific and industrial fields for the purpose of building self-powered systems.<sup>4</sup> The

piezoelectric element is based on the non-centrosymmetric structured materials such as perovskite and wurtzite materials. Conventionally, the perovskite materials including lead zirconate titanate (PZT) ( $\text{Pb}(\text{Zr}_x\text{Ti}_{1-x})\text{O}_3$ ) and barium titanate (BT) ( $\text{BaTiO}_3$ ) were utilized as piezoelectric active materials in lighters, buzzers and guitar pick-up. However, for flexible and biocompatible, low-cost, and body-implantable properties of piezoelectric materials, oxide semiconductor nanomaterials enables possibly the natural embed into soft cloth or wearable electronics. Especially, the Wurtzite crystals such as ZnO, gallium nitride (GaN), and cadmium sulfide (CdS) nanomaterials are relatively easy to synthesize and biocompatible, allowing applications in implantable and human motion electronics.<sup>5,6,7</sup>

Human motion energy harvesting patches and biosensors via piezoelectric transduction mechanism using highly elastic and biocompatible nanomaterials are the main topic of my research. The nanostructured wurtzite materials based human motion nanodevices has offers few advantages. The nanostructured materials can be subjected to extremely large elastic deformation without deformation or fracture. The nanometer-sized structures allows high resistance to fatigue and possibly extend the lifetime of the device. In addition, the nanostructure can be bent under tiny applied force, which can be applied in low frequencies or weak mechanical disturbance application. The nanostructured wurtzite material also can be easily grown in low temperature via chemical synthesis and easily integrated with the piezoelectric devices. For this, fundamental of piezoelectric effect of ZnO nanomaterials are managed in chapter 2. More precisely, the origin of piezoelectricity is presented, following by the several piezoelectric characteristics and constants for calculation of piezoelectric efficiency

in piezoelectric active materials. Moreover, the properties of ZnO as well as the piezoelectric aspect of ZnO nanomaterials are also reviewed for comprehension of the basic principle of piezopotential generation inside of the nanomaterials.<sup>8,9,10,11</sup> Moreover, the aqueous synthetic route of nanostructures such as ZnO thin film and NR were introduced for knowledge in synthetical mechanism. In addition, the operational mechanism of piezoelectric devices were also analyzed based on the physical principles. The types and applications for future electronics of piezoelectric devices are finally studied for nanodevice and nanosystem for multifunctionalities.

In chapter 3, all-solution-processed flexible thin film piezoelectric patch was demonstrated using simple aqueous ZnO ink as a thin film.<sup>12</sup> A low-temperature process was adopted to deposit piezoelectric ZnO thin film directly onto the plastic substrates without any thermal damage. Moreover, screen-printing of silver paste was applied on the top of the PENG for a top electrode formation. The flexible thin film PENG based on the solution processed ZnO film and silver paste electrode allowed the piezoelectric energy generation through rolling motion and muscle stretching of the patch because of its flexible ultrathin structure. The output voltages and current density through the rolling process is about 0.66V and 55.5nA/cm<sup>2</sup>, which are about 2 times higher than outputs from the bending motion of the PENG.

In chapter 4, with same purpose on self-powered nanosystem, a piezoelectric sensor was also developed with bi-axially grown NRs. The ZnO NRs were grown by hydrothermal method, conducting at very low temperature under 100°C with simple process. The as-synthesized ZnO NRs were hybridized with PDMS as piezoelectric active materials and the electrode of Ag NW-SWCNT utilized in the

piezoelectric bending motion sensor for flexible sensory system. Through the fabrication process, the bending motion sensors for simultaneous recognition of bending curvature and speed was proposed and is expectable to apply in any piezoelectric elements for self-powered sensing system.

Finally, in chapter 5, comprehensive conclusion of chapter 3 and 4 and final goal of this study is presented.

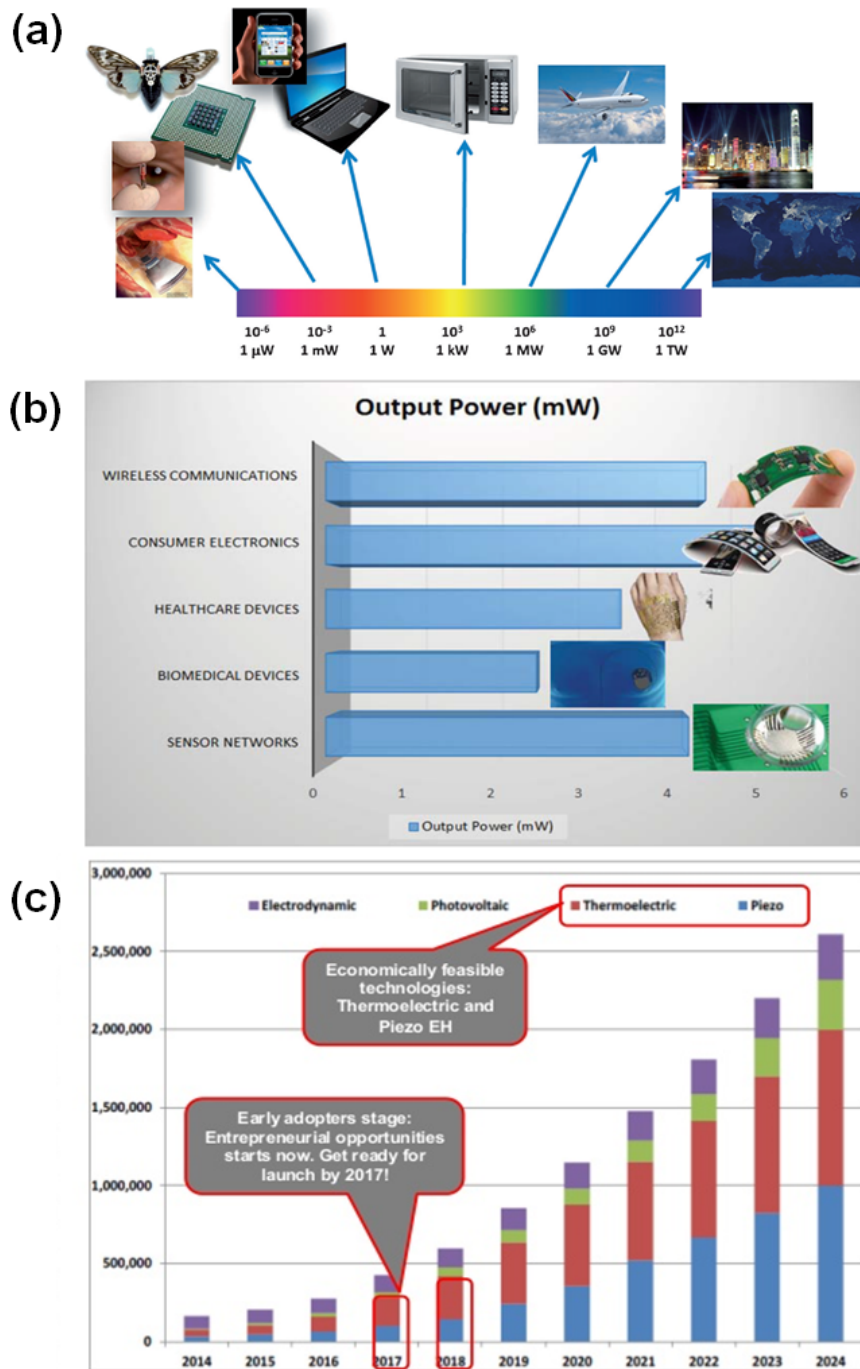


**Figure 1.1** Needs for personal/mobile electronics (from Ref. [55] Copyright 2012 Wiley Publishing Group). (b) Output powers for wireless electronics (from Ref. [56] Copyright 2015 Elsevier Publishing Group). (c) Global market for energy harvesting forecast (from Intech, 2013)

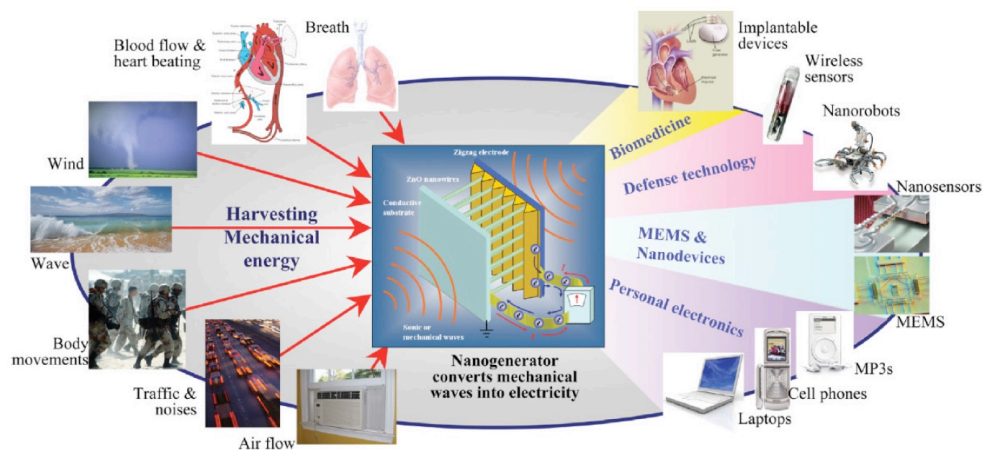


**Figure 1.2** Perspectives of piezoelectric devices for potential future applications

(from Ref. [57] Copyright 2008 Wiley Publishing Group) .

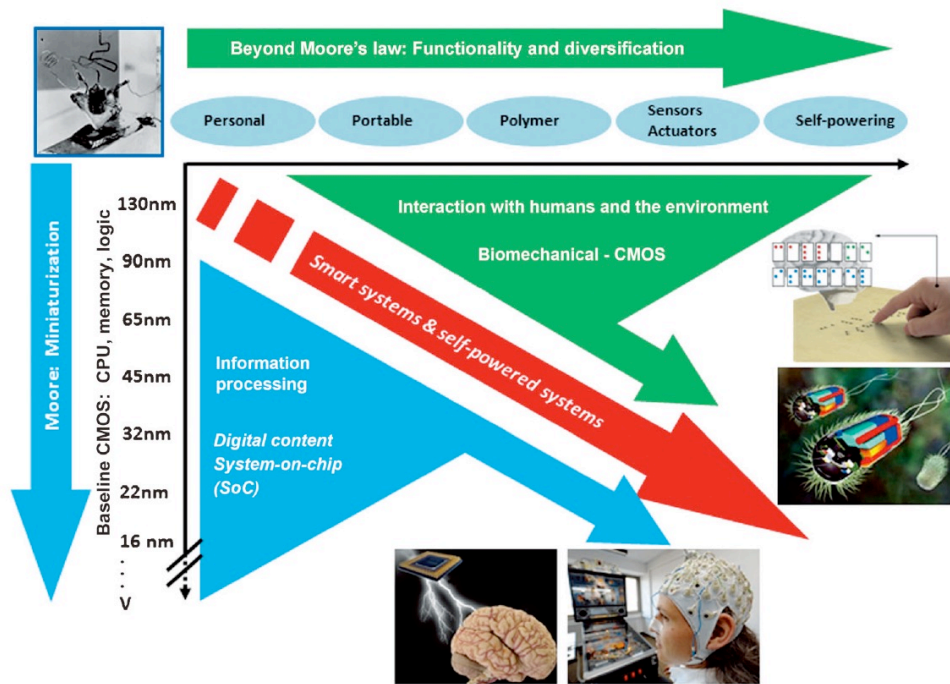


**Figure 1.3** Future perspective of electronics for nanodevice and nanosystem for multi-functionalities (from Ref. [55] Copyright 2012 Wiley Publishing Group).



## 1.1 References

- [1] Z. L. Wang, W. Wu, *Angew. Chem. Int. Ed.* **2012**, 51, 11700.
- [2] S. H. Lee, C. K. Jeong, G. -T. Hwang, K. J. Lee, *Nano Energy* **2015**, 14, 111.
- [3] Z. L. Wang, *Adv. Funct. Mater.* **2008**, 18, 3553.
- [4] Z. L. Wang, *Sci. Am.* **2008**, 298, 82.
- [5] Z. L. Wang, *Nano today* **2010**, 5, 540.
- [6] Z. L. Wang, *Mat. Sci. Eng. R* **2009**, 64, 33.
- [7] Z. L. Wang, R. Yang, J. Zhou, Y. Qin, C. Xu, Y. Hu, S. Xu, *Mat. Sci. Eng. R* **2010**, 70, 320.
- [8] APC International, Ltd., *Piezoelectric ceramics: principles and applications*, APC International, Ltd., Pennsylvania, second edition.
- [9] Z. L. Wang, *Adv. Funct. Mater.* **2008**, 18, 3553.
- [10] Y. Qi, M. C. McAlpine, *Energy Environ. Sci.* **2010**, 3, 1275.
- [11] Z. L. Wang, *J. Phys. Chem. Lett.* **2010**, 1, 1388.
- [12] S. Y. Chung, S. Kim, J.-H. Lee, K. Kim, S.-W. Kim, C.-Y. Kang, S.J. Yoon, Y. S. Kim, *Adv. Mater.* **2012**, 24, 6022.

## **Chapter 2. Literature review and theories**

### **2.1 Introduction of piezoelectricity**

Piezoelectric effect is a phenomenon of certain materials to generate electric charge in response of applied mechanical stress.<sup>1</sup> The word ‘piezoelectricity’ is derived from Greek word ‘piezein’, which means ‘to squeeze’ or ‘to press’.<sup>2</sup> The piezoelectric phenomenon was first discovered in 1880 by the French physicist brothers Pierre and Jacques Curie. Curie brother proved the piezoelectric effect through experimental using tinfoil, glue, wire, and magnets. From crystals of tourmaline, quartz, topaz, and Rochelle salt, electrical polarization was created with mechanical pressure.

The mechanical pressure applied along the certain crystallographic axes in crystal cause generation of electric charge on the crystal surfaces. This electric charge per unit area is polarization, which is proportional to the mechanical pressure, and the polarization is generated only when the pressure is applied.

The piezoelectric effect is created in crystal having no center of symmetry.<sup>3</sup> The piezoelectric phenomenon can be explained in molecular structure of crystal. Without mechanical stress, the centers of mass for the positive and negative charges are at the same position. This molecular structure is ‘symmetrical’. When mechanical stress is applied in quartz along  $X_1$ -axis, the centers of mass for positive and negative charges are split, causing the appearance of dipole moment between certain faces of the crystal. The molecular structure state of the quartz is now in ‘non-centrosymmetrical’. The dipole moment of the crystal creates electrical potential difference, which is the piezoelectric effect. The direction of dipole moment is opposite when compressive and/or tensile stress is applied and

the phenomenon is shown in figure 2.1.

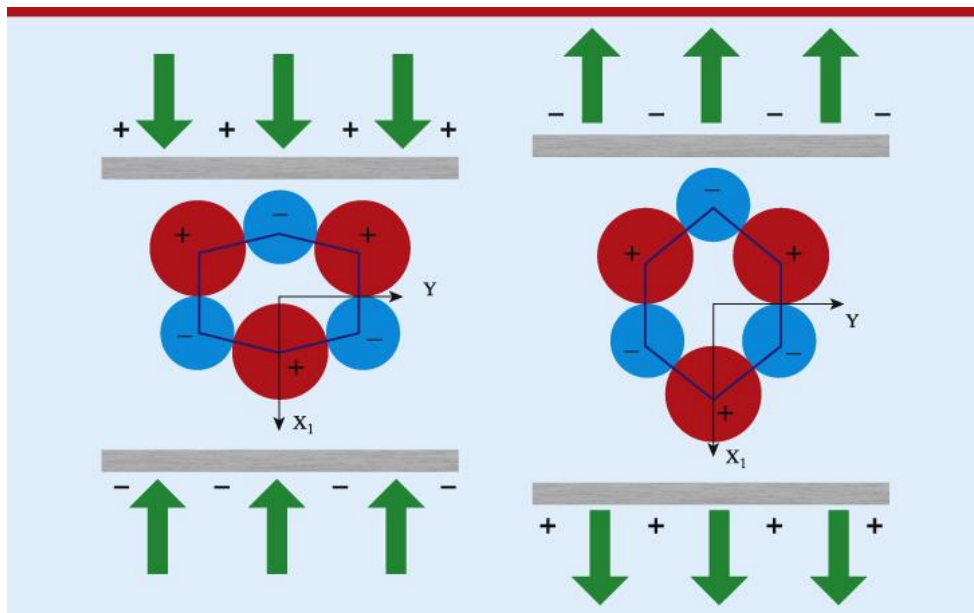


**Figure 2.1** Induced charges in quartz crystal under mechanical compressive and/or tensile stress along the electrical  $X_1$  axis (*from Ref. [3], Copyright 2013 IOPscience Publishing Group*).

### 2.1.1 Direct/converse piezoelectric effect

In 1880, Pierre and Jacques Curie demonstrated that crystals such as tourmaline, quartz, topaz, Rochelle salt generate electrical polarization in response of a mechanical stress. Later in 1881, Gabriel Lippman realized and mathematically derived the converse piezoelectric effect using by thermodynamic principles and again Curie experimentally proved the theories.<sup>4</sup>

Crystals generally have a net balance of electric charges in zero without applying mechanical stress, where the positive and negative charges are at the same. However, with applying mechanical stress, the net balance of electric charges is not zero and the electric charge carriers are transferred through an external circuit load, which created electricity as shown in figure 2.2.

The direct piezoelectric effect is a phenomenon of generation of electric charge by applying a mechanical stress into a crystal.<sup>5</sup> The mechanical stress causes a strain, which can be expressed as an equation

$$T = Y S$$

where T is the mechanical stress, S is the strain, and Y is the Young's modulus.

The electric charge can be measured as electric field or potential across piezoelectric materials. The electric charge is proportional to the stress, and the sign for compression or/and tension is opposite. Therefore, the direct piezoelectric effect may write as equation

$$D = \frac{Q}{A} = d T$$

where D is the dielectric displacement, Q is the electric charge, A is the area, and d is the piezoelectric coefficient.

The dielectric displacement, also called as electric displacement field, is defined

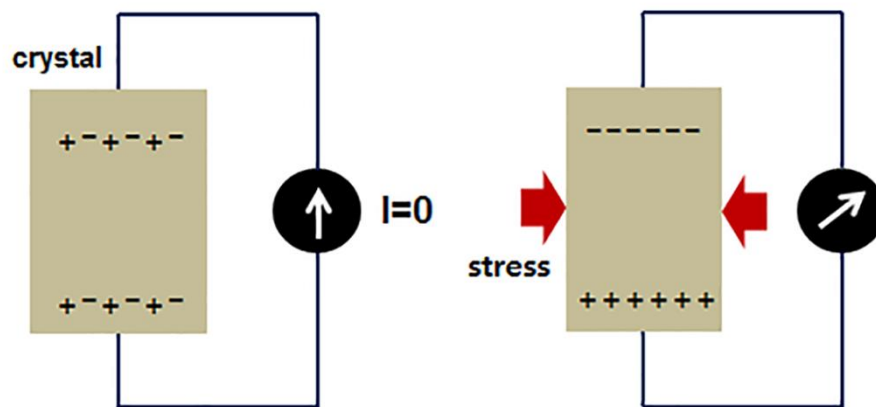


**Figure 2.2** Net balance of electric charge in crystal as a result of application of mechanical stress.

as

$$D = \epsilon_0 E + P$$

where  $\epsilon_0$  is the vacuum permittivity, and  $P$  is the permanent and induced dipole moment inside materials, also known as polarization density. If electric field is inserted into a dielectric material, center of mass for charges is separated including a local electric dipole moment. If no electric field is applied, the equation for direct piezoelectric effect can be described as

$$P = d T (\because D \cong P)$$

Therefore, the electrical polarization ( $C\ m^{-2}$ ) is directly proportional to the applied mechanical stress (Pa).

The piezoelectric material under tension along the polarization direction (poling direction) generates voltage with opposite polarity that of the poling voltage. However, the piezoelectric material under compression along the polarization direction generates voltage of the same polarity as the poling voltage as shown in figure 2.3.

The converse piezoelectric effect is a phenomenon of mechanical deformation by application of an electric field to a crystal. The resultant strains are proportional to an electric field and mechanical deformation of expansion or/and contraction is observed.

$$S = d E$$

where  $S$  is the strain, and  $E$  is the electric field.

If a voltage is applied into the piezoelectric material as the same polarity of the poling voltage, the piezoelectric crystal will be expanded parallel to the poling voltage direction. However, if a voltage is applied into the piezoelectric material as

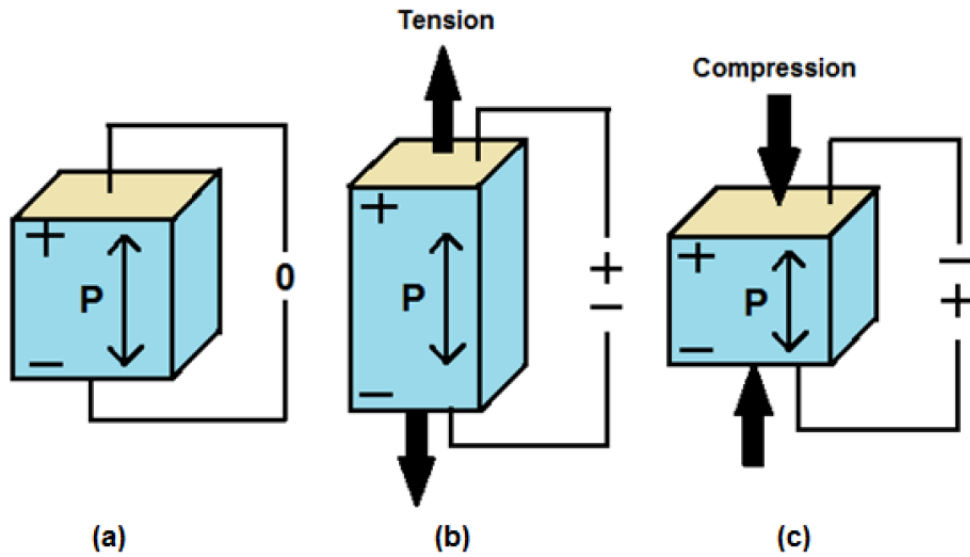


**Figure 2.3** Schematic image of direct piezoelectric effect. (a) Piezoelectric material after poling process. (b) Piezoelectric material under tension, and (c) compression (from Ref. [5], Copyright 2012 Intech Publishing Group).



opposite to the poling voltage, the piezoelectric crystal will be compressed parallel to the poling voltage direction as shown in figure 2.4. For both direct and converse piezoelectric effect, the proportionality constant is the piezoelectric constant  $d$ , which can be expressed as follow

$$d = \frac{D}{T} \text{ ( or } \frac{P}{T} \text{ )} = \frac{S}{E}$$

Therefore, high value of the  $d$  implies high polarization density in response of mechanical stress or high degree of motion or vibration to an applied electric field. Applications of the direct piezoelectric effect is a device of converting mechanical stress into electrical energy such as Ignition units, NGs, pressure sensors, accelerometers, push buttons, and airbag sensors. On the other hand, the converse piezoelectric effect based applications develop motion or vibration as a result of an applied electric field. The examples for converse effect are ultrasonic cleaners, actuators, motors, transducers, micro-pumps, and any ultrasonic machines (table 1).

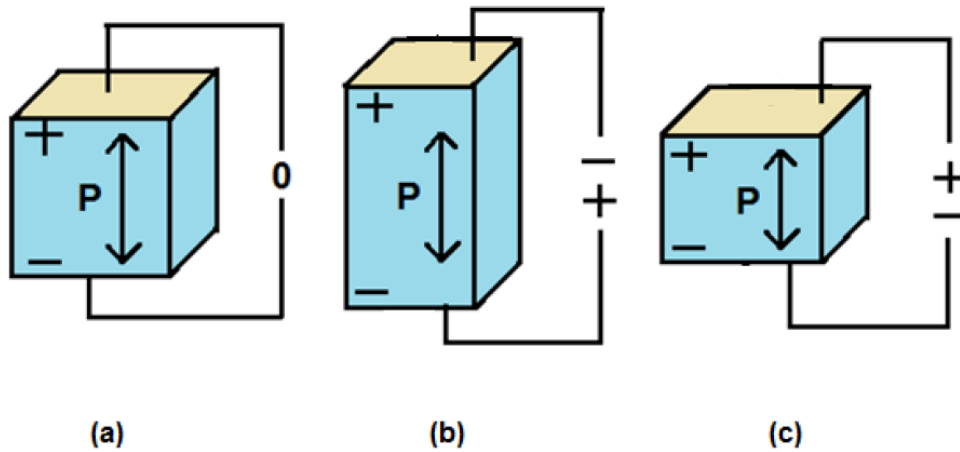


**Figure 2.4** Schematic image of converse piezoelectric effect. (a) Piezoelectric material after poling process. (b) Piezoelectric material when a voltage of the same polarity of the poling voltage is applied, and (c) piezoelectric material when a voltage of the opposite polarity of the poling voltage is applied (*from Ref. [5], Copyright 2012 Intech Publishing Group*).

| <b>Direct piezoelectric effect</b> | <b>Converse piezoelectric effect</b> |
|------------------------------------|--------------------------------------|
| Ignition units                     | Ultrasonic cleaners                  |
| Nanogenerators (NGs)               | Actuators                            |
| Pressure sensors                   | Motors                               |
| Accelerometers                     | Transducers                          |
| Push buttons                       | Micro-pumps                          |
| Airbag sensors                     | Ultrasonic machines                  |

**Table 1** Applications of direct / converse piezoelectric effect.

### 2.1.2 Poling and hysteresis curve for polarization

Traditional piezoelectric ceramics are perovskite crystals, consisting of small and tetravalent metal ion at the center, generally titanium or zirconium, and large and divalent metal ions at the cubic lattice, generally lead or barium, and oxygen ions at the rhomboid lattice.<sup>2</sup> Generally, each perovskite crystals possess critical temperature point whether or not dipole moment exists at the crystal symmetry. Above the Curie temperature, each grain of perovskite crystal exhibits no dipole moment with a simple cubic symmetry. Otherwise, below the Curie temperature, each grain in each crystal carries a dipole moment with tetragonal or rhombohedral symmetry, depending on the composition of the material.

Back to the perovskite crystals, the relative small tetravalent metal at the center is facile to move up-and-down compared to the bigger divalent metal ions or oxygen ions. Accordingly, the movement of tetravalent metal ion confers the polarization of the crystal structure if the temperature is below the Curie point and the example is shown in figure 2.5. For example, if the tetravalent positive metal ions moves to the upside from the center of crystal structure, the upper side of crystal has positive electric charge, otherwise the lower side of crystal possesses negative electric charge and vice versa.

However, the ceramics of piezoelectric materials are ordinary non-piezoelectric without application of an electric field even though the individual crystals might have strong piezoelectric property because the piezoelectric effect can be canceled out from the domain of individual crystals. Precisely, the region of like-oriented dipole moment is defined as a domain, and the dipole moment of each domain is canceled out because of random orientation and finally the overall polarization is

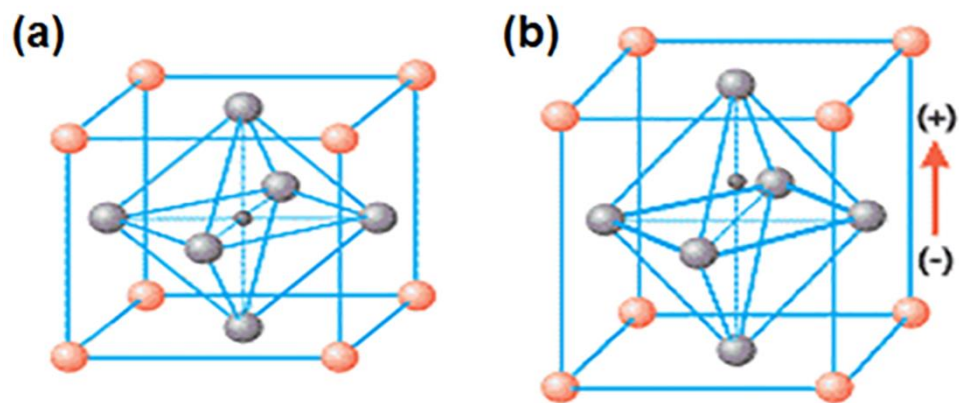


**Figure 2.5** Crystal structure of piezoelectric ceramics applied (a) temperature above the Curie point and (b) temperature below Curie point (*from Ref. [2], Copyright Intech Publishing Group*).

zero balance (figure 2.6 (a)). Accordingly, application of an electric field must be conducted to switch the polar axes of the crystallites inside the ceramic to those direction nearest to that of the electric field. This application of an electric field is so called “poling” process (figure 2.6 (b)). After the poling treatment slightly below the Curie temperature, the ceramic maintain a net dipole moment permanently, which is called as “remnant polarization” (figure 2.6 (c)). The crystals with remnant polarization as a result of the applied electric field will respond to additional applied electric field or mechanical stress until the field or stress is below that needed to switch the polar axis.

Figure 2.7 shows typical polarization (P) – electric field (E) hysteresis curve, which express effect of an electric field on polarization.<sup>6</sup> When the electric field is applied to a piezoelectric ceramic element, the polarization is followed path, (i) to (ii). After removal of the electric field, the path (ii) to (iii) is followed and the piezoelectric crystal retain certain level of polarization, expressed as  $P_r$  (remnant polarization), and permanent deformation of piezoelectric materials that makes it anisotropic is formed. Comprehensively, the poling process shifts the polarization state from (i) to (iii). If a voltage with the same polarity as the electric field is applied, the polarization value will follow the path of (iii) to (ii). However, the curve showing the effect of the electric field on strain (S-E) also follows certain path depending on the electric field. When the P-E path experiences the (iii) to (ii) path, the P-S curve also follows the path (iii) to (ii), which means development of positive strain as a function of the electric field. Accordingly, the piezoelectric materials will expand along the poling axis. Reversely, if a voltage with the opposite polarity as the electric field is applied, the P-E and S-E curves will follow the path (iii) to (iv), resulting in negative strain. Therefore, the piezoelectric

material compressed along the electric field and elongated perpendicular to the poling axis. However, as soon as the electric field is removed, the state of piezoelectric material returns to its poled dimensions ((iii) state on plot P-E and S-E).

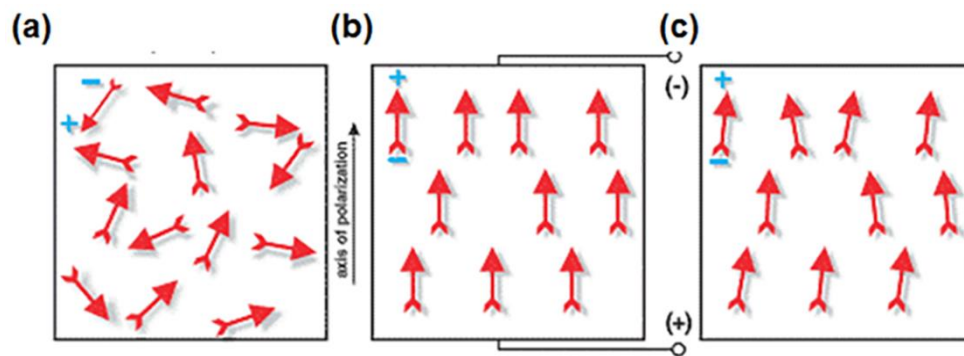


**Figure 2.6** Poling a piezoelectric ceramic (a) random orientation of polar domains prior to polarization, (b) polarization after application of an electric field, and (c) remnant polarization after removal of an electric field (*from Ref. [2], Copyright Intech Publishing Group*).



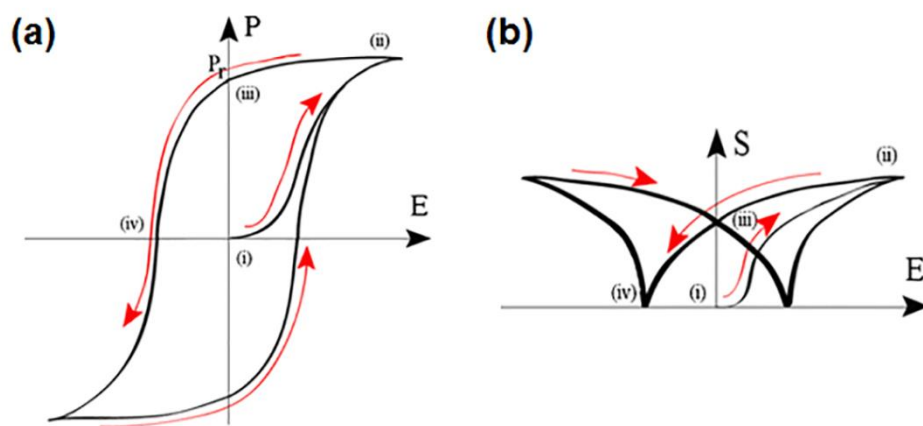


**Figure 2.7** (a) Typical polarization (P) – electric field (E) hysteresis plot showing the effect of an electric field on polarization and (b) strain versus electric field plot showing relative increase/decrease in dimension (strain) in direction of polarization (from Ref. [2], Copyright Intech Publishing Group).

### 2.1.3 Piezoelectric constants

For definition of the piezoelectric effect, the direction of several factors need to be defined with subscript. Because of anisotropic structure of piezoelectric materials, physical constants remark with two subscripts for both the direction of applied mechanical or electrical force and the direction of perpendicular to the applied force. To identify directions of axes, subscripts 1, 2, and 3 represent the direction X, Y, and Z respectively, and subscripts 4, 5, and 6 indicate a shear of the direction X, Y and Z. Otherwise, superscript in constant values indicates a quantity kept constant. For example,  $d_{31}$  is polarization generated in the direction 3 as a result of a stress applied in lateral direction. In case of  $d_{33}$ , the direction of polarization is vertical (direction 3) as a result of a stress applied in vertical direction. Finally,  $d_{15}$  is polarization generated along axis 1 by a sheer stress (figure 2.8).

Generally, the piezoelectric material has 31 mode, where the direction of a mechanical stress applied to an electrode is proportional, otherwise, in 33 mode, a mechanical stress is applied to an electrode in parallel direction (figure 2.9).<sup>7</sup>

Piezoelectric charge constant (d): The polarization generated per unit of mechanical stress (T) applied to a piezoelectric material or the strain occurred in a piezoelectric ceramic per unit of an applied electric field.

$$d = \frac{D}{T} \text{ ( or } \frac{P}{T} \text{ if } E = 0 \text{ ) } = \frac{S}{E}$$

As explained above, the d indicates the proportionality constant of the direct and converse piezoelectric effect. The first subscript of the d value represents the direction of polarization generated in case of the direct piezoelectric effect, otherwise, indicates the direction of applied electric field toward the piezoelectric materials in case of the converse piezoelectric effect. The materials in case of the

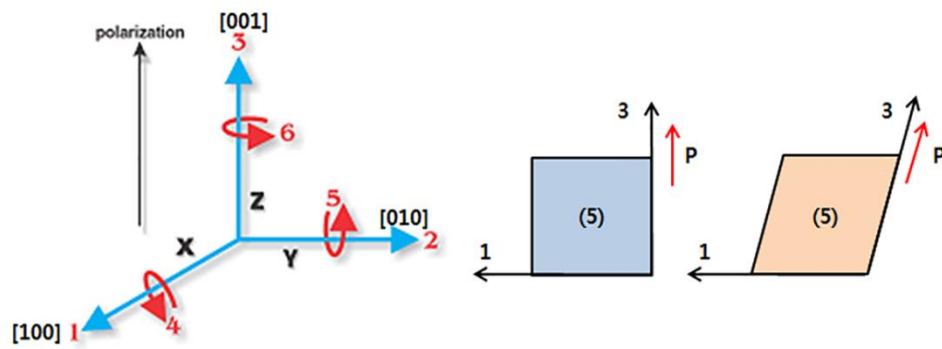


**Figure 2.8** Direction of forces affecting a piezoelectric materials and examples of piezoelectric materials for definition of direction of polarization and mechanical stress (*from Ref. [2], Copyright Intech Publishing Group*).

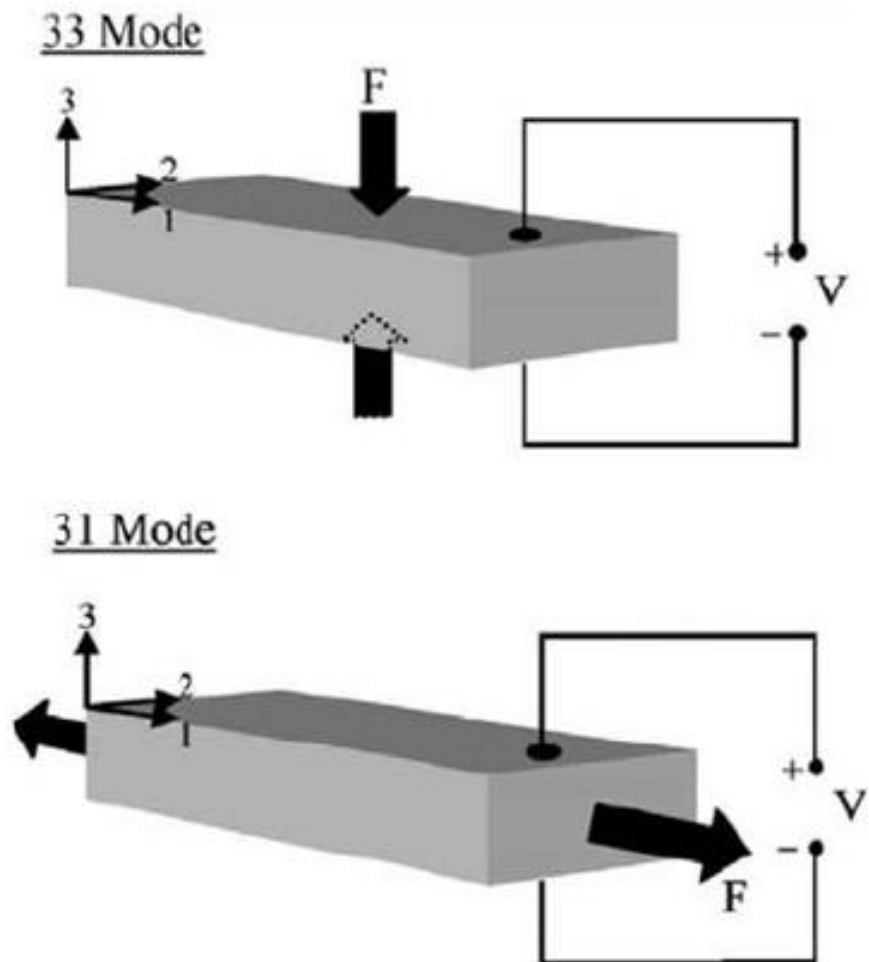


**Figure 2.9** Illustration of -33 mode and -31 mode operation for piezoelectric materials (from Ref. [7], Copyright 2012 SAGE Publishing Group).

converse piezoelectric effect. The second subscript implies the direction of the applied mechanical stress (direct piezo effect) or the direction the strain experienced across the piezoelectric material (converse piezo effect). Since the value of  $d$  indicates extent of induced strain in a piezoelectric material as a result of an electric field applied, it can be an indicator for strain dependence for actuator applications.

**Permittivity ( $\epsilon$ ):** The dielectric displacement per unit of an electric field. The first subscript for the  $\epsilon$  value is the direction of the dielectric displacement, otherwise, the second subscript indicates the direction of an electric field.

$$\epsilon = \frac{D}{E}$$

The  $K$  value is defined as a relative dielectric constant, which is ratio of  $\epsilon$ . The  $\epsilon$  is the amount of charge stored inside of ceramic material, whereas  $\epsilon_0$  is the charge stored by the same electrodes when separated by a vacuum at the same voltage condition.

$$K = \frac{\epsilon}{\epsilon_0}$$

**Piezoelectric voltage constant ( $g$ ):** The electric field produced per unit of mechanical stress applied to a piezoelectric material or the strain occurred in a piezoelectric ceramic per unit of an applied electric displacement.

$$g = \frac{E}{T} = \frac{S}{D}$$

The first subscript of the  $g$  value indicates the direction of electric field generated or the direction of applied electric displacement. The second subscript indicates the

direction of the applied mechanical stress or the direction of strain induced across the piezoelectric material. Since the value of  $g$  is defined as strength of induced electric field as a result of a mechanical stress applied, it can be an indicator for sensing ability for sensor applications.

$$g = \frac{d}{\epsilon^T}$$

$$\text{or } d = g \epsilon^T$$

**Electromechanical coupling factor (k):** An indicator of the effectiveness for converting electrical energy into mechanical energy or converting mechanical energy into electrical energy. The first subscript indicates the direction along which the electrode applied, and the second subscript denotes the direction along which the mechanical energy is applied, or generated.

$$k = \sqrt{\frac{d^2}{\epsilon^T s^E}}$$

**Young's modulus (Y):** The indicator of the stiffness of the piezoelectric material.  $Y$  is the value of the applied stress to the material divided by the resulted strain in the same direction.

$$Y = \frac{T}{S}$$

**Elastic compliance (s):** The strain induced in a piezoelectric material per unit of mechanical stress applied. It is reciprocal of the modulus of elasticity if the stress is applied in the 11 or 33 directions. The first subscript indicates the direction strain and the second subscript is the direction of stress.

$$s = \frac{S}{T}$$

The overall piezoelectric constants were presented in table 2.

| Piezoelectric constant | Equations                           | Superscript             | Subscript 1   | Subscript 2                    |
|------------------------|-------------------------------------|-------------------------|---|--------------------------------|
| $d_{31}$               | $S/E = D/T$                         | .                       | The polarization or electric field in 3 axes          | The stress or strain in 1 axes |
| $g_{31}$               | $E/T = S/D$                         | .                       | The electric displacement or electric field in 3 axes | The stress or strain in 1 axes |
| $\epsilon$             | $D/E$                               | constant stress         | The electric displacement in 3 axes                   | The electric field in 3 axes   |
| $k_{31}$               | $\sqrt{\frac{d^2}{\epsilon^T S^E}}$ | .                       | The electric displacement or electric field in 3 axes | The stress or strain in 1 axes |
| $Y_{33}$               | $T/S$                               | .                       | The stress in 3 axes                                  | The strain in 3 axes           |
| $S_{33}^E$             | $S/T$                               | constant electric field | The strain in 3 axes                                  | The stress in 3 axes           |

**Table 2** Piezoelectric constants expressing the piezoelectric properties (*from Ref. [2], Copyright Intech Publishing Group*).



### **2.1.4 Piezoelectric materials**

The piezoelectric materials can be defined as a special subset out of total crystal classes with particular characteristics (figure 2.10).<sup>8</sup> Of 32 crystal classes, only 21 crystals are non-centrosymmetric. Except one crystal class, whose piezoelectric moduli was canceled out by the operational symmetry elements (432 crystal class), 20 crystals are piezoelectric. 10 out of these are polar crystal classes, which exhibit a spontaneous polarization due to a non-vanishing electric dipole moment inside unit cell of crystal without applying mechanical load. These polar crystals are also pyroelectric, which create an electric field as result of temperature gradient inside the crystals. However, the non-polar crystals having no dipole moment without applying mechanical load have no pyroelectric properties and the typical crystal example is quartz. If the dipole moment of the crystal can be reversed by the application of an electric field, the material is said to be ferroelectric, which are also both piezoelectric and pyroelectric. The representative ferroelectric materials are perovskite materials including PZT and BT, otherwise, the example of non-ferroelectric but polar pyroelectric materials is wurtzite materials such as ZnO and GaN.

For polar crystals, which hold electrical polarization without mechanical stress, the piezoelectric effect manifests itself by changing the magnitude or the direction of polarization or both. However, for non-polar crystal, electrical polarization is only vanished by applying mechanical stress. Therefore, the stress applied on the crystal exchanges the non-polar crystal to a polar crystal classes with having electrical polarization.

Also, the piezoelectric material can be classified based on the distinguishment of

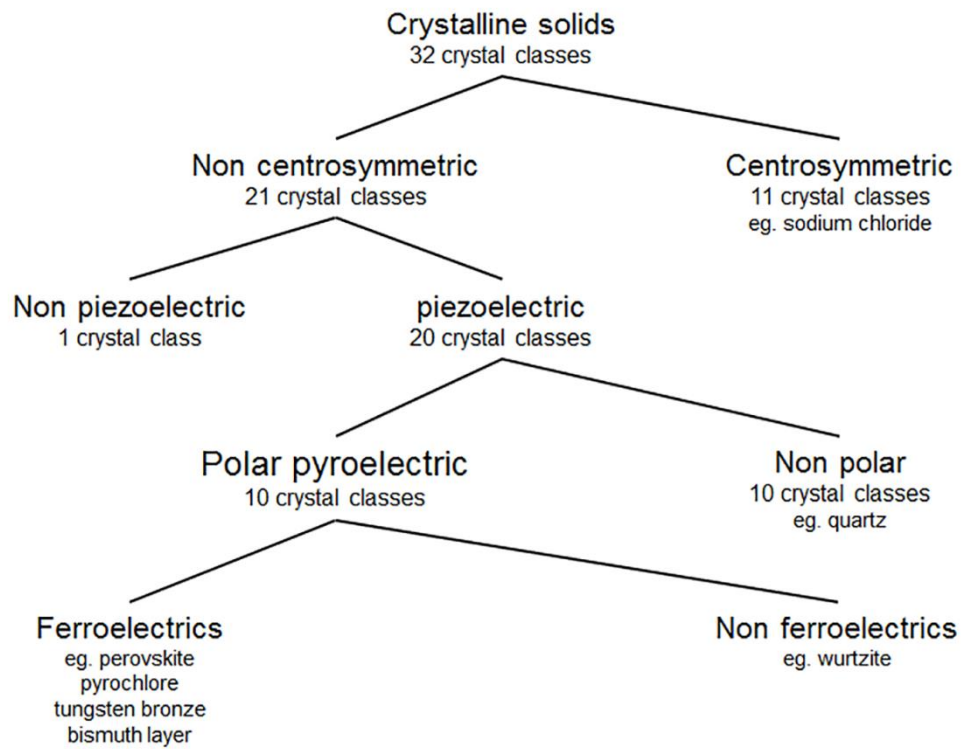


**Figure 2.10** The classification of crystal structures into piezoelectric, pyroelectrics, and ferroelectrics.

natural or synthesized one. The natural piezoelectric crystals are quartz, cane sugar, rochelle salt, topaz, tourmaline group, minerals and dry bone. However, there are two man-made crystals, which are gallium orthophosphate and langasite. The man-made crystals are barium titanate, Lead titanate, lead zirconate titanate, potassium niobate, lithium tantalite, sodium tungstate. The representative piezoelectric polymer material is polyvinylidene fluoride (PVDF).

#### 2.1.4.1 Perovskite materials

The basic chemical formula of perovskite is  $ABO_3$ , where A is divalent metal ions, such as lead ( $Pb^{2+}$ ) or barium ( $Ba^{2+}$ ) located at the lattice of tetragonal, whereas the B represents the tetravalent metal ions such as titanium ( $Ti^{4+}$ ), zirconium ( $Zr^{4+}$ ) located at the center.<sup>9</sup> At high temperature, generally above the Curie temperature, the structure of perovskite is in paraelectric phase, whose space group is  $Pm3m$ , where the A atom is at the corner of the cube, whereas the atom is at the body center and the oxygen is at the face center, as shown in figure 2.11 (a) and (b). However, with cooling the perovskite below its Curie temperature, paraelectric to ferroelectric phase transition occurs, which is accompanied with a specific strain, being induced by the displacement of the B atom relative to the oxygen octahedron network.

The representative perovskite ferroelectric crystals include BT, PZT and relaxor-PT (PMN-PT:  $(1-x)Pb(Mg_{1/3}Nb_{2/3})O_3-xPbTiO_3$ , PZN-PT:  $(1-x)Pb(Zn_{1/3}Nb_{2/3})O_3-xPbTiO_3$ , etc.), and  $(Na_{1/2}Bi_{1/2})TiO_3$  (NBT) and  $(K_{1/2}Na_{1/2})NbO_3$  crystals. BT is the first man-made perovskite, but the piezoelectric properties of BT do not show obvious advantages over its ceramic counterpart because of the cracky properties

and the low Curie temperature. Because of these reasons, the application of BT is limited.

PZT ceramics have been the most widely used piezoelectric material since their discovery. The PZT has high dielectric constant and piezoelectric voltage, which is desirable as a piezoelectric material. However, because of lead atom, the PZT is not biocompatible and not applicable to the bio-implanted devices.

A breakthrough in piezoelectric crystals occurred in 1989, when Shrout reported the solid solution of relaxor (PMN or PZN) and ferroelectric PT can be readily grown in single crystal form following the earlier work of Kuwata et al. in 1982.<sup>10</sup> PMN – xPT ( $x = 0.28\sim 0.33$ ) crystals with morphotropic phase boundary (MPB) compositions exhibit high piezoelectric coefficients ( $d_{33} = 1500$  to  $2500$  pC/N) and electromechanical coupling factors ( $k_{33} > 0.9$ ), higher than PZT-based ceramics with  $d_{33} = 200$  to  $700$  pC/N and  $k_{33} = 0.6$  to  $0.75$ . Because of these outstanding electromechanical properties, the PMN-PT crystals have been utilized as medical transducers by various companies around the world.

#### **2.1.4.2 Wurtzite materials**

The wurtzite materials are another well-known piezoelectric materials, where the piezoelectricity originates from the lack of center symmetry in the wurtzite crystal structure (figure 2.11 (c)).<sup>11</sup> The representative piezoelectric wurtzite materials are ZnO, GaN, indium nitride (InN), and zinc sulfide (ZnS).<sup>12</sup> Although bulk form of the wurtzite material has been less widely used as piezoelectric materials because of the poor piezoelectric properties, nanoscale ZnO and GaN have received considerable attention due to a synergy of their piezoelectric and semiconducting

properties, which has been termed as “piezoelectronics”. The nanoscaled wurtzite materials were utilized in area of piezoelectric NGs, nanotransistors, and nanodiodes. Especially, by Wang group, prototype of ZnO based PENGs was firstly introduced with extensive studies on wurtzite structure. Subsequently, various configurations of ZnO and GaN nanoparticles/wires/tubes/belts have been synthesized and applied to an energy harvesting field.

### 2.1.4.3 Quartz

Quartz is the most frequently used natural piezoelectric crystal. The crystal structure contains  $\text{SiO}_4$  tetrahedral that forms three-dimensional framework with chirality (figure 2.11 (d)).<sup>13</sup> The trigonal  $\alpha$  phase having space group of  $P3_121$ , is piezoelectric at normal temperature and pressure with two coefficient  $d_{11}$  and  $d_{14}$ . Otherwise, at high temperature, the transition from the  $\alpha$  phase to  $\beta$  phase (hexagonal) having space group  $P6_322$ , is piezoelectric with coefficient value of  $d_{14}$ . The general application of quartz is a resonator for tracking time in quartz watches.

### 2.1.4.4 Polymer based materials

The PVDF is consisted of  $\text{CH}_2\text{CF}_2$  chains and is a semi-crystalline polymer.<sup>14</sup> The chains produced large sheets which can be stretched or poled to give them a piezoelectric property. The kind of PVDF polymer structure is at least five forms that depend on the chain conformation of trans (T) and gauche (G) linkages. The crystalline structure of  $\alpha$  and  $\beta$  phase of PVDF is shown in figure 2.11 (e), respectively.<sup>15</sup> The  $\alpha$  phase of PVDF is most abundant form in nature and  $\beta$  phase has a piezoelectric property due to its polar structure with one-way ordered

hydrogen and fluoride atoms along with the carbon backbone.

When an electric field is applied across the sheets, the polymer structure either contracts in thickness and expands along the stretched direction or expands in thickness and contract along the stretched direction depending which way the field is applied.<sup>14</sup> This is because the positive hydrogen atom tends attracting to the negative side of the electric field and repelling from the positive side of the electric field. However, the negative fluorine atoms attract to the positive side of the electric field and repel from the negative side of the electric field. As a results of the application of electric field, from  $\alpha$  to  $\beta$  phase transformation is aroused, and the piezoelectric properties could be obtained.

The overall piezoelectric constants and dielectric constants for each piezoelectric materials were presented in table 3.<sup>16</sup>

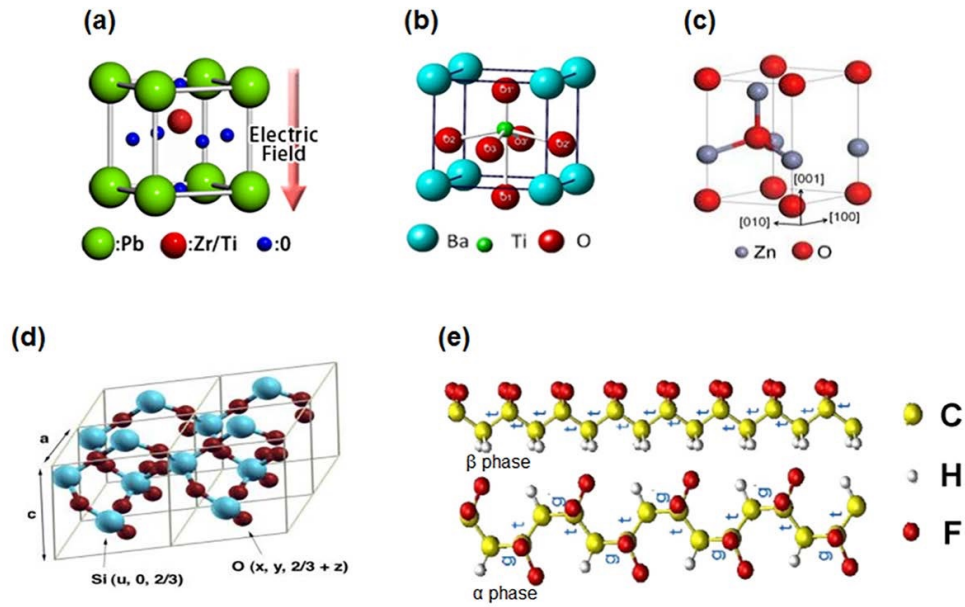


**Figure 2.11** Various piezoelectric materials including (a-b) perovskite materials, (c) wurtzite materials, (d) quartz, and (e) polymer based materials (*from Fujitsu, cea, Ref. [11], Copyright 2012 Nature Publishing Group, Book: The origin of Earth's Radioactivity, Ref. [13], Copyright 2015 Intech Publishing Group*).

| Material           | Structure       | Piezoelectric constant<br>$d_{33}/\text{pC N}^{-1}$ | Dielectric constant<br>$\epsilon$ |
|--------------------|-----------------|---|-----------------------------------|
| PMN-PT             | Single crystal  | ~2000 to 3000                                       | ~6000                             |
| PZT                | Polycrystalline | ~250 to 700   | ~1300 to 3900                     |
| PZT                | Thin film       | ~60 to 130  | ~300 to 1300                      |
| BaTiO <sub>3</sub> | Thin film       | 191   | 1700                              |
| ZnO                | Thin film       | 5.9   | 10.9                              |
| Quartz             | Thin film       | 2.3 ( $d_{11}$ )                                    | 4.5                               |
| PVDF               | Polymer film    | -33   | 13                                |
| PZT-fiber          | Composite       | ~180 to 460   | ~495                              |
| PZT-<br>PVDF       | Composite       | ~13 to 25   | .                                 |

**Table 3** Piezoelectric materials and their properties (*from Ref. [14] Copyright 2010 RSC Publishing Group*).



## 2.2 ZnO

ZnO is a piezoelectric and semiconducting material with having properties of wide band gap of 3.37 eV and a large binding energy of 60 meV at room temperature. ZnO forms abundant configuration of nanostructures, which is applicable to lots of applications.<sup>18</sup> Moreover, ZnO is transparent and flexible and non-toxic, and biocompatible. ZnO has various applications in optics, optoelectronics, actuators, sensors, energy harvesting, biomedical and spintronics.

The basic structure of ZnO is wurtzite crystal, which has hexagonal unit cell with space group  $C6mc$  and lattice parameters  $a = 0.3296$  and  $c = 0.52065$  nm. The ZnO structure is stack of alternating planes of tetrahedrally coordinated  $O^{2-}$  and  $Zn^{2+}$  with layer by layer configuration along the c-axis.<sup>19</sup> The lack of central symmetry of the wurtzite structure results in the piezoelectric properties of ZnO, which is the essential for the mechanic-electric energy conversion in application of ZnO based PENG as well as the strain sensors.

Under non-stress conditions, the positive and negative center of mass coincide with each other so there are no dipoles. Otherwise, when the crystal is subjected to a mechanical force, the positive and center of mass become split, leading to an electric dipole.<sup>20</sup> In crystallographic aspects, the oppositely charged ions produced positively charged Zn-(0001) and negatively charged O-(000 $\bar{1}$ ) polar surfaces, resulting in a dipole moment and spontaneous polarization along the c-axis.<sup>21</sup> The potential created by the polar ions is called “piezoelectric potential” or “piezopotential”.

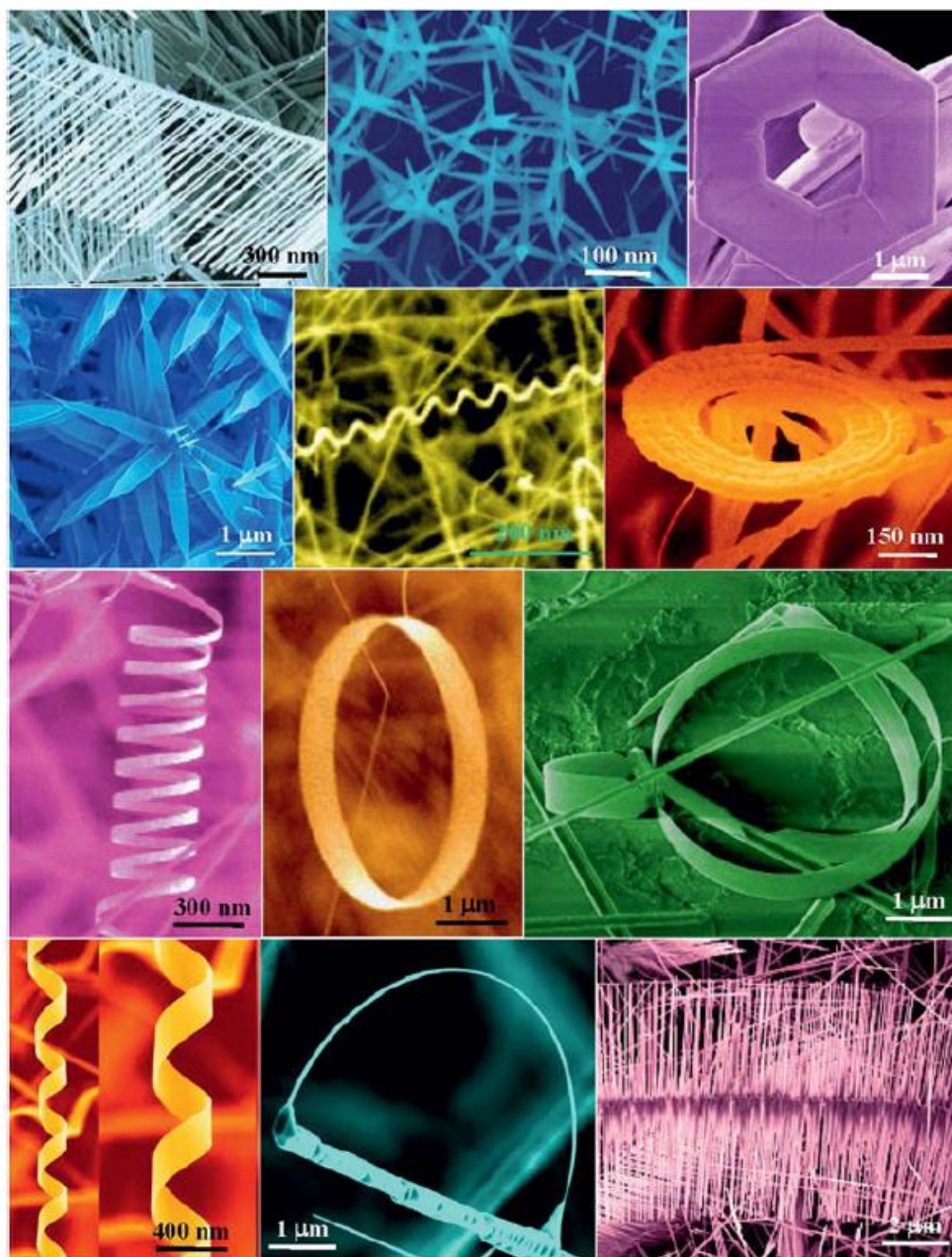


**Figure 2.12** Various ZnO nanostructures grown in polar  $\pm (0001)$  surfaces (*from Ref. [20] Copyright 2012 MRS Publishing Group*).

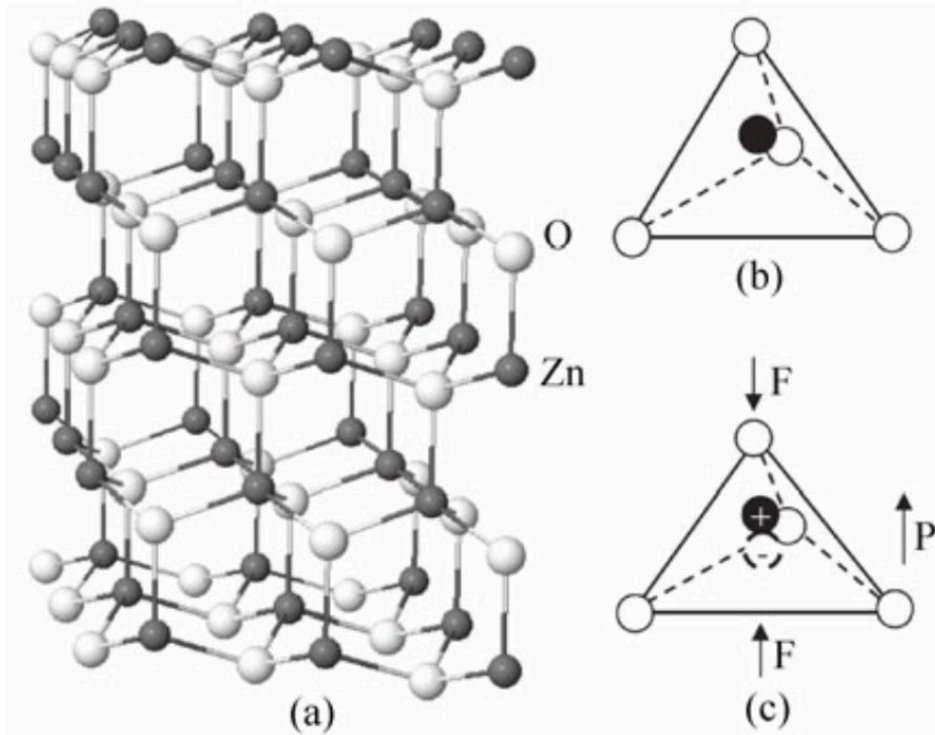


**Figure 2.13** Wurtzite structure of ZnO oriented along the  $[0001]$  direction. (b) Tetrahedral coordination between Zn and O atoms under no mechanical strain. (c) Distortion of the tetrahedral structure under compressive strain, showing the displacement of the positive and negative mass of center (*from Ref. [18] Copyright 2011 Springer Publishing Group*).

### 2.2.1 Piezoelectric properties of ZnO nanomaterials

For piezoelectric nanomaterials, the crystal structure and the equilibrium condition of the outer atom layer might be considerably differed from those of the bulk materials. This phenomenon attributes to the extremely large surface-to-volume ratio of piezoelectric structure at nanoscale. Because of these effects, elastic, piezoelectric and dielectric properties of the surface of the nanomaterials differ from those of the bulk. The size-dependency of the piezoelectric properties has been observed through several experimental results.<sup>22,23,24,25,26</sup>

In figure 2.14 (a), the axial piezoelectric coefficient of three dimensional (3D) perovskite BT and wurtzite ZnO and GaN nanowires is shown as a function of their cross-section thickness  $t$ .<sup>12</sup> The  $e_{33}$  of perovskite BT nanowires decreases with decreasing thickness  $t$ , while the  $e_{33}$  of wurtzite ZnO and GaN nanowires increase with decreasing thickness. The opposite trend of the piezoelectric properties with the scale of perovskite and wurtzite structures can lead to the  $e_{33}$  of a thin wurtzite nanowire exceeding that of its perovskite counterpart.

Otherwise, as shown in figure 2.14 (b), the effective piezoelectric coefficient ( $d_{33}$ ) of ZnO nanobelts was measured using piezoresponse force microscopy (PFM).<sup>27</sup> Compared to the references of bulk (0001) ZnO, the effective piezoelectric coefficient of individual (0001) surface dominated ZnO nanobelts is frequency dependent and much larger (14.3 to 26.7 pm/V) than that of the bulk (0001) ZnO (9.93 pm/V). Therefore, the nanostructured ZnO such as ZnO NWs, NRs and thin film can be an attractive candidate as a building block for piezoelectric nanodevices.

Moreover, tensile test was conducted for the measurement of both force and

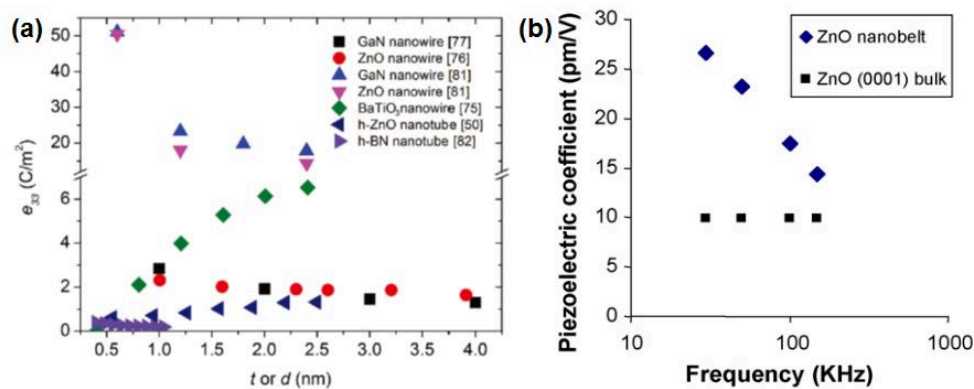


**Figure 2.14** (a) The piezoelectric coefficient ( $e_{33}$ ) of several perovskite and wurtzite materials as a function of cross thickness ( $t$ ) or diameter ( $d$ ) (from Ref. [12] Copyright 2014 RSC Publishing Group). (b) Experimentally measured piezoelectric coefficient ( $d_{33}$ ) for ZnO and its comparison to that of the bulk (from Ref. [27] Copyright 2014 ACS Publishing Group).

elongation of ZnO NW.<sup>28</sup> The diameter of the ZnO NW was 20 nm and two ends of the NW were clamped on a nano-manipulator tip (left) and atomic force microscopes (AFM) cantilever (right), as shown in field emission scanning electron microscope (FE-SEM) images of figure 2.15. The tensile load was applied until fracture as shown in figure 2.15 (e). As a result, the Young's modulus was measured and the value was approximately 169 GPa, which is higher than that of ZnO bulk in (0001) direction (~140GPa).

Buckling test of ZnO NWs was also conducted in opposite manner to the tensile test. The 46 nm thick ZnO NW was bound by electron beam induced deposition and incrementally increasing compressive load was applied (figure 2.16). When the force reached a critical point, the ZnO NW buckled, as shown in figure 2.16 (c). The axial displacement of ZnO NW with change applied compressive force was plotted in figure 2.16 (f). From two tensile and buckling tests, the properties of robust and ultra-flexible ZnO NWs were observed compared to ZnO bulk film. Therefore, the nanostructured ZnO materials will be versatile to be applied in piezoelectric elements.

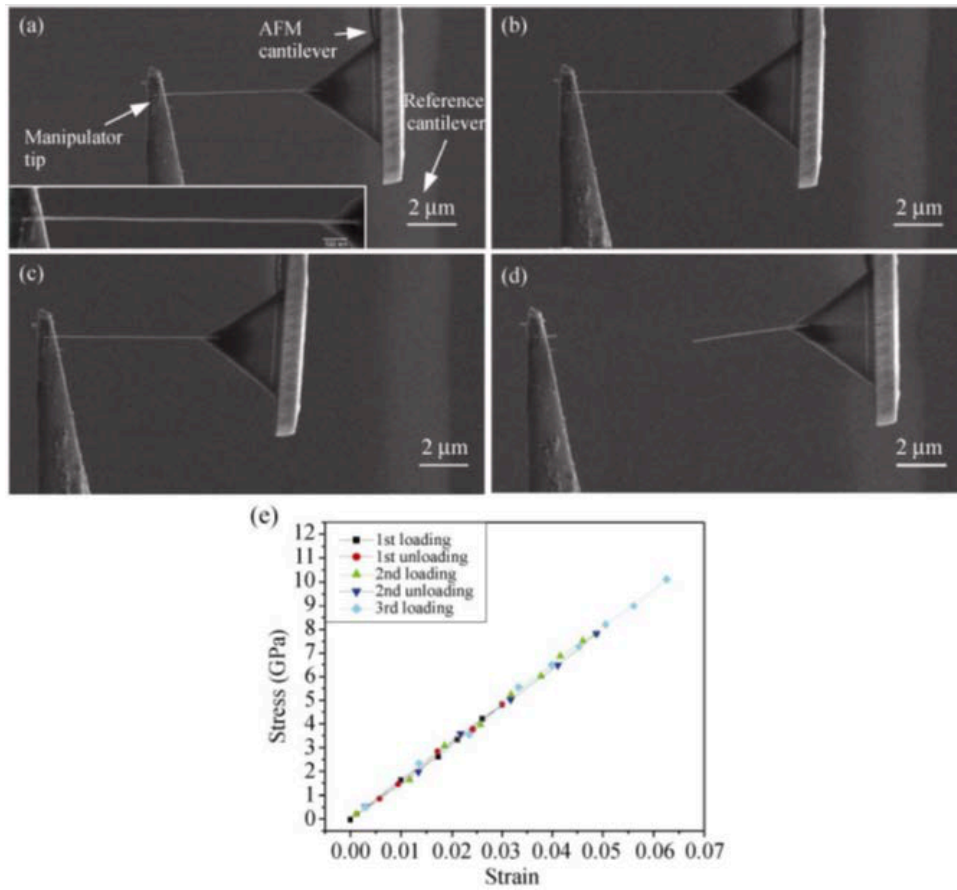


**Figure 2.15** (a-d) FE-SEM images of tensile test on a 20 nm-thick ZnO NWs. (e) A stress-strain response of the 20nm-thick ZnO NWs under repeated loading and unloading (*from Ref. [28] Copyright 2010 Springer Publishing Group*).

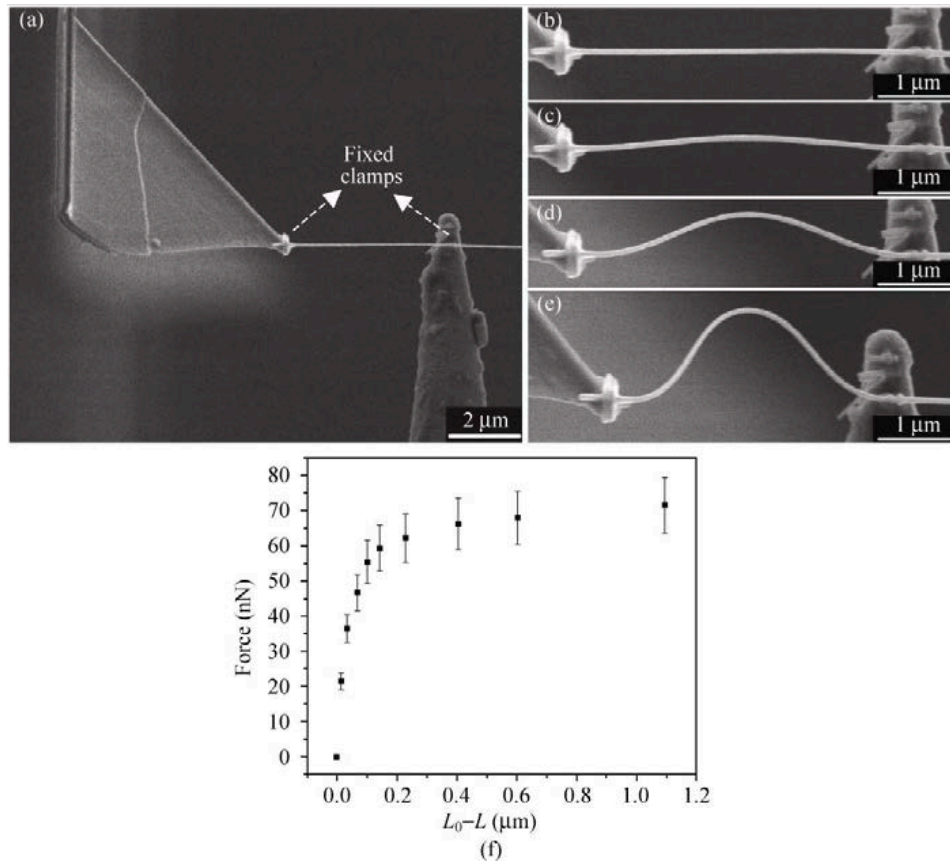


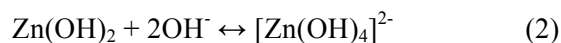
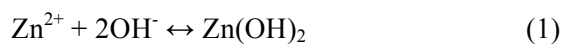
**Figure 2.16** (a-e) FE-SEM images of buckling test on 46 nm-thick ZnO NW (f) A plot of applied force versus axial displacement of ZnO nanowire (*from Ref. [28]* Copyright 2010 Springer Publishing Group).

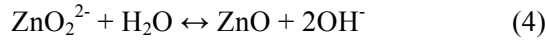
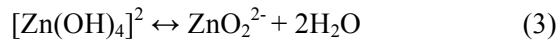


### 2.2.2 Synthesis of ZnO nanomaterials

ZnO is generally crystallized by the hydrolysis of Zn salts in a basic solution, which has strong or weak alkalis. Since  $\text{Zn}^{2+}$  ion coordinates in tetrahedral complexes, it forms 3d electron configuration. Accordingly, it is colorless and has zero crystal field stabilization energy. Wurtzite structure ZnO is generally growing in c-axis direction, which has high energy polar surfaces of  $\pm [0001]$  surface with alternating  $\text{Zn}^{2+}$ -terminated and  $\text{O}^{2-}$ -terminated surfaces. Owing to the high energy of polar surfaces of ZnO, the incoming precursor molecules tend to favorably adsorb on the polar surfaces and generate ZnO nucleus. Subsequently, the precursors form one layer of polar surface and reversed polar surface is also formed by absorption process. For example, after  $\text{Zn}^{2+}$ -terminated surface is formed,  $\text{O}^{2-}$ -terminated surface is formed on to the  $\text{Zn}^{2+}$  polar surface. This process leads to grow ZnO along the  $\pm [0001]$  direction with non-polar  $\{1\bar{1}00\}$  and  $\{2\bar{1}\bar{1}0\}$  surface exposing to the solution.<sup>29</sup>

An alkaline solution is essential for formation of ZnO nanostructure because generally divalent metal ions do not hydrolyze in acidic environments.<sup>18</sup> The normally used alkali compounds are potassium hydroxide (KOH) and sodium hydroxide (NaOH). Otherwise, since  $\text{K}^+$  has a larger ion radius and thus a lower probability of incorporation in the ZnO lattice, the KOH is more preferable to NaOH. Generally, the solubility of ZnO in an alkali solution increases with the alkali concentration and temperature. The main reaction of the ZnO growth is as follows.





As it can be seen in figure 2.17 (a),  $\text{Zn}^{2+}$  ions exist in a series of intermediates, and ZnO can be formed by the dehydration of these intermediates, depending on the pH, concentration of  $\text{Zn}^{2+}$  and temperature. In equation (2), the product is not only  $\text{Zn}(\text{OH})_4^{2-}$ , but also be form in the  $\text{Zn}(\text{OH})^+$ ,  $\text{Zn}(\text{OH})_2$ ,  $\text{Zn}(\text{OH})_3^-$ , depending on the pH value and concentration of  $\text{Zn}^{2+}$ . These intermediates are all in equilibrium with the major forms being different reaction conditions.

The overall growth process is as follows. At the beginning, the  $\text{Zn}^{2+}$  and  $\text{OH}^-$  ions coordinate with each other, and dehydration by proton transfer forms  $\text{Zn}^{2+} \cdots \text{O}^{2-}$   $\text{Zn}^{2+}$  bonds, and leading to an agglomerate in the form of  $[\text{Zn}_x(\text{OH})_y]^{(2x-y)+}$ , which has an octahedral geometry. Then the  $\text{H}_2\text{O}$  molecules formed by dehydration migrate into the solution. After aggregates reach around 150 ions, wurtzite structure of ZnO domains are then nucleated in the center of the aggregates as shown in figure 2.17 (b). The  $\text{O}^{2-}$  in ZnO comes from the base, not from the solvent  $\text{H}_2\text{O}$ .<sup>30</sup> Therefore, the solvent could be organic solvents, such as methanol, ethanol, and butanol, or even ionic liquids.<sup>31,32,33,34,35</sup> The aspect ratio of ZnO nanostructure is controlled by the concentration of  $\text{OH}^-$  and reaction time. Also, the reaction solvent can tune the morphologies of polar inorganic nanocrystals by the crystal-solvent interfacial interactions.

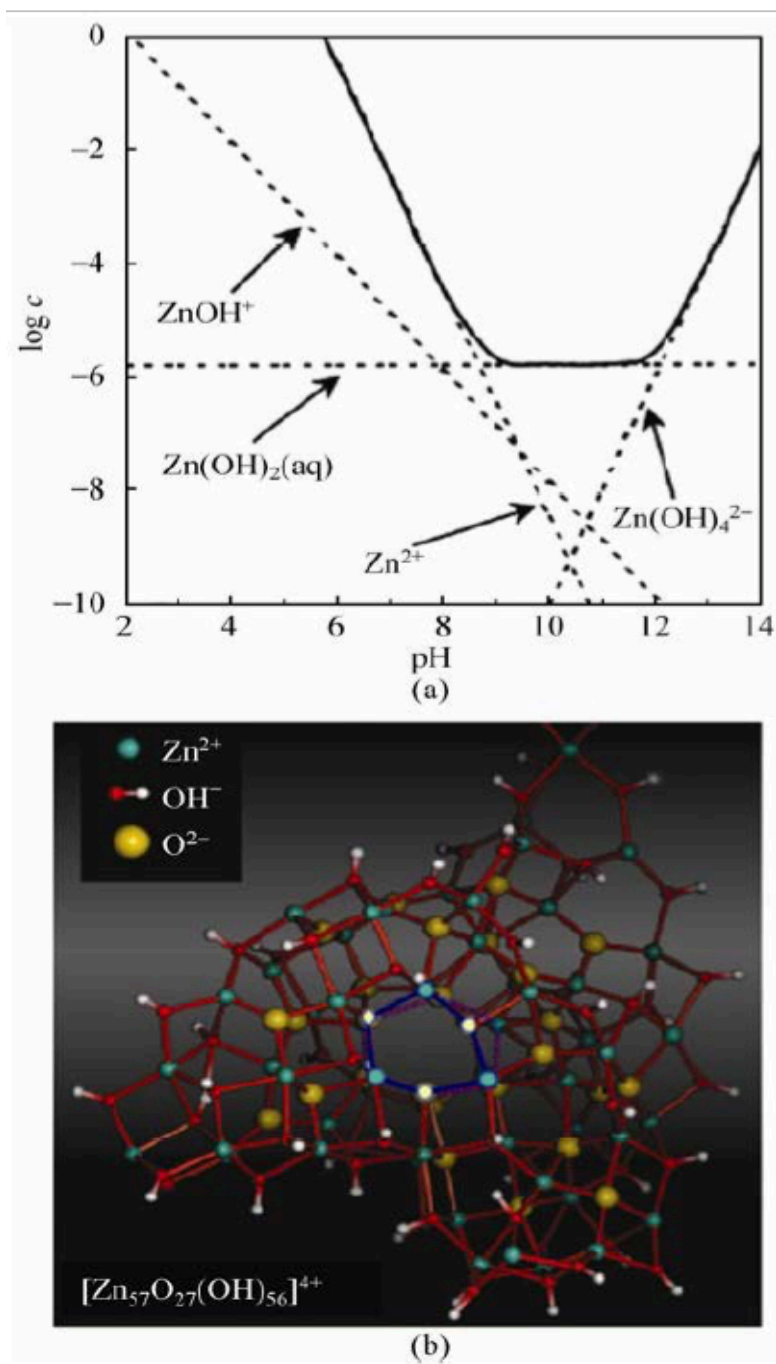
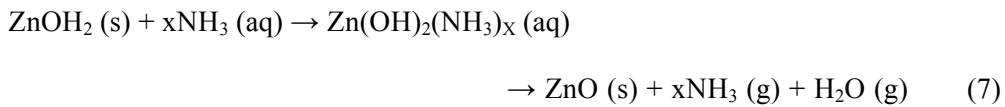
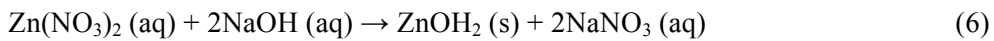


**Figure 2.17** (a) ZnO-H<sub>2</sub>O system as a function of precursor concentration and pH.  
 (b) Aggregation and nucleation of domains of the wurtzite structured ZnO (from Ref. [18] Copyright 2011 Springer Publishing Group).

### 2.2.2.1 ZnO thin film

ZnO thin film in this study was basically fabricated in wet chemical environment.<sup>36</sup> The Zn solution were prepared by dissolving  $\text{Zn}(\text{NO}_3)_2 \cdot 6\text{H}_2\text{O}$  in distilled water in a total concentration of 0.5 M Zn. NaOH was also dissolved in distilled water in 2.5 M and dropwise to the Zn solution. The resulting hydroxide slurry was centrifuged and the supernant was removed. These rinsing and removing steps were repeated to minimize the concentration of  $\text{Na}^+$  and  $\text{NO}_3^-$ . The final hydrated precipitate dissolved in ammonia water and finally the solution was coated and annealed at 150°C for an hour. The example of these experimental is also in literature and the FE-SEM image of ZnO film is shown in figure 2.18. These experimental procedure can be shown as equations as below.



As explained previously, the ZnO is amphoteric in nature and the weak acidity of the  $\text{Zn}^{2+}$  ion affords a wide solubility range. The  $\text{Zn}(\text{OH})_2$  dehydration an oxide crystallization requires low activation energy which is the main cause for low temperature processing. The ammonia is featured compared to other nitrogen-based ligands by its extreme volatility and unstable bonding, which also afford low temperature, rapid and low volume-loss decomposition processes. A dense and homogeneous morphology of thin film is possible in this low temperature process.

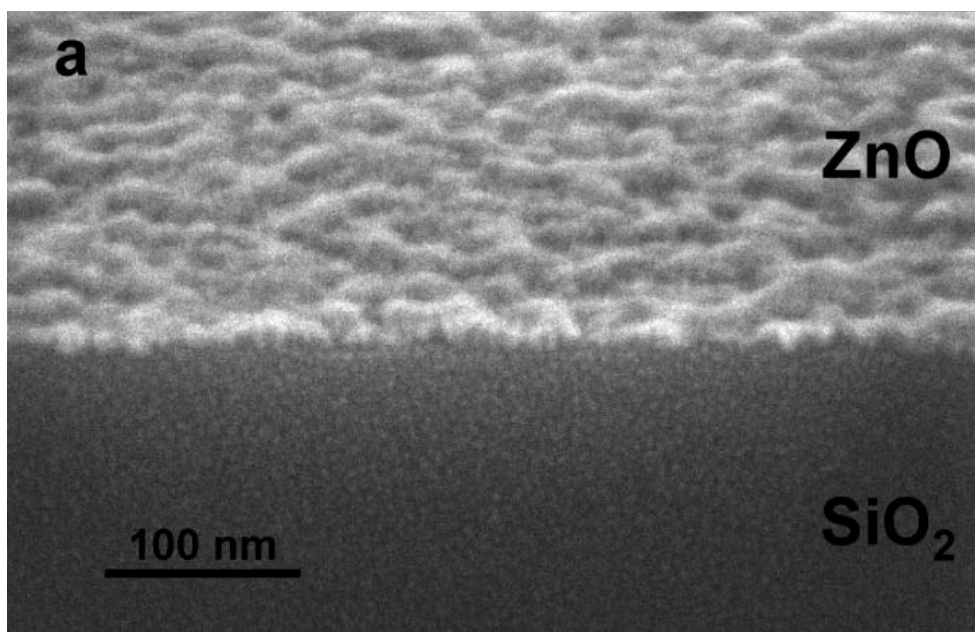
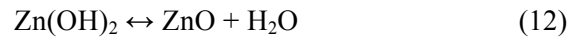
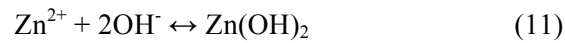
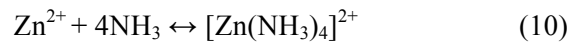
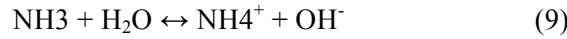


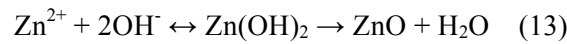
**Figure 2.18** FE-SEM image of ink-jet printed ZnO thin film onto SiO<sub>2</sub> annealed at 150 °C (from Ref. [36] Copyright 2008 ACS Publishing Group).

### 2.2.2.2 ZnO NRs

The hydrothermal growth of ZnO NRs is generally started with chemical reagents of zinc nitrate ( $\text{Zn}(\text{NO}_3)_2$ ) and hexamethylenetetramine (HMTA).<sup>37</sup> The chemical reactions for hydrothermal growth of ZnO NRs are conducted in five steps as below.



A simplified equation of the overall reaction is as follows



The  $\text{Zn}(\text{NO}_3)_2$  provides  $\text{Zn}^{2+}$  ions, otherwise the  $\text{H}_2\text{O}$  molecules in the solution provide  $\text{O}^{2-}$  ions. The function of HMTA during the growth of ZnO NW/NRs is not clearly discovered until now, but it is believed to be act as a weak base and pH buffer. After the hydrolyzation with water and the gradual production of HCHO molecular structure, as shown in equation (6), and (7). If the HMTA hydrolyzes quickly and produced large amount of  $\text{OH}^-$  in a short period of time, the  $\text{Zn}^{2+}$  ions in solutions would precipitate out quickly because of the high pH circumstance and this finally would result in fast consumption of the nutrient and prohibit further growth of ZnO NRs along the c-axis. Also, the HMTA coordinates with  $\text{Zn}^{2+}$  ions and stabilizes aqueous  $\text{Zn}^{2+}$ . Under a pH buffered condition by HMTA, the  $\text{Zn}(\text{OH})_2$  has the minimum solubility and therefore precipitates of  $\text{Zn}(\text{OH})_2$  was created and dehydrated to ZnO nuclei. For the growth of ZnO NRs, the quantity of

the ZnO nuclei depends on the equilibrium concentration of  $\text{Zn(OH)}_2$  under the given conditions.

The growth procedure of ZnO NRs can be controlled by adjusting the reaction parameters such as precursor concentration, growth time and growth temperature to push the reaction equilibrium forwards and backwards. Generally, the precursor concentration determines the density of ZnO NRs and growth time and temperature adjust the ZnO morphology and aspect ratio. The dehydration of  $\text{Zn(OH)}_2$  into ZnO under ultrasonication, or even under sunlight. Also, the reaction (6) can be pushed to the equilibrium forwards by increasing the reaction temperature, since the number of moles of product is larger than that of reactant's one, so there is an increase in entropy during reaction. The rate of hydrolysis of HMTA increases with the decreasing pH and vice versa. The overall reaction carried out faster with increasing reaction temperature for the growth of ZnO NRs.

Importantly, the ZnO morphology is also controlled by the counter ions such as acetate, formate, chloride, nitrate perchlorate and sulfate. Hydrothermal growth using acetate and formate and chloride counter-ions has tendency to form ZnO NRs, otherwise use of nitrate and perchlorate tends to produce NW form, and sulfate to be in flat hexagonal platelet form. This hydrothermal method can be carried out at low temperature with large scale on any substrates regardless of amorphous or crystalline state.

However, for uniform growth of ZnO NRs, kinetically controlled process can be adopted as shown in figure 2.19. Generally, ZnO NRs are through normal heat-up system in a one-pot process. However, for several reasons, this normal method shows poor uniformity of ZnO NRs in their shapes and size compared with the kinetically grown ZnO NRs. Figure 2.20 show the different mechanism of normal

one-pot heat-up process and kinetically controlled process for synthesizing ZnO NRs. In the case of normal one-pot heat-up process, the nucleation for ZnO seed is occurred under increasing temperature condition with rich supplement of  $\text{Zn}^{2+}$  ions since the reaction is conducted in one-pot process. Accordingly, as shown in figure 2.20 (a), the nucleation of ZnO seeds occurs at both low and high supersaturation levels of the zinc compound and as the supplementary rate of  $\text{OH}^-$  ions in the aqueous solution increases by HMTA decomposition with increasing temperature, the zinc compound concentration again reaches a high supersaturation level and secondary nucleation and growth of ZnO NRs occurs. As a result, non-uniform ZnO NRs with various diameters and lengths and multi-branched shaped ZnO NRs are produced as shown in figure 2.21 (a) and (c).

On the other hands, the kinetically controlled process of ZnO NR growth system is conducted with constant feeding of  $\text{Zn}^{2+}$  ions by a syringe pump into constant 85 °C hot temperature HMTA solution. Therefore, the restrictedly injected  $\text{Zn}^{2+}$  ions rapidly reacted with  $\text{OH}^-$  ions and gradually produced zinc compounds. Because of high temperature condition, almost all zinc compounds convert to ZnO seeds based on thermodynamic mechanism. After formation of ZnO seeds, the growth of ZnO NRs occurs spontaneously with continuous injection of  $\text{Zn}^{2+}$  ions. As a result, uniform ZnO NRs are grown with constant diameters and lengths as shown in figure 2.21 (b) and (d).

The growth mechanism of ZnO NRs can be explained by particle-mediated growth and assembly mechanisms, which include the specific mechanism of “oriented aggregation (OA)”. The OA is spontaneous self-organization of adjacent particles with crystallographic orientation. In the particle-particle regime, they attracted by van der Waals forces and reduce the overall energy by removing the



surface energy associated with incomplete bonds. The final oriented aggregates often exhibits a hierarchical structure. Further growth of ZnO nanocrystal was based on the classical primary model mechanism.

The schematic diagram for the sequential steps for the ZnO NR growth by OA mechanism is presented in figure 2.22. In colloidal phase, the ZnO seed particles are rapidly formed by OA mechanism at the initial step. After several seconds, the seed particles brought into oriented assembly and Ostwald ripening with a residual or re-injected zinc source grows the ZnO nanocrystals grown into NR shape by the classical growth mechanism. Therefore, the OA mechanism in very first stage dominates the formation of ZnO seeds.

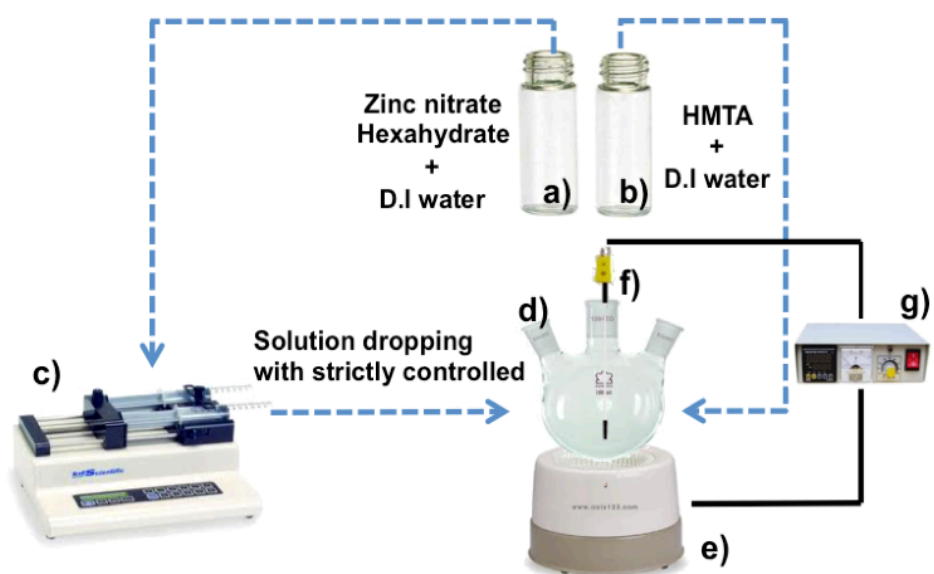


**Figure 2.19** Schematic diagram of the kinetically controlled ZnO NRs synthesis system (from Ref. [37] Copyright 2012 RSC Publishing Group).

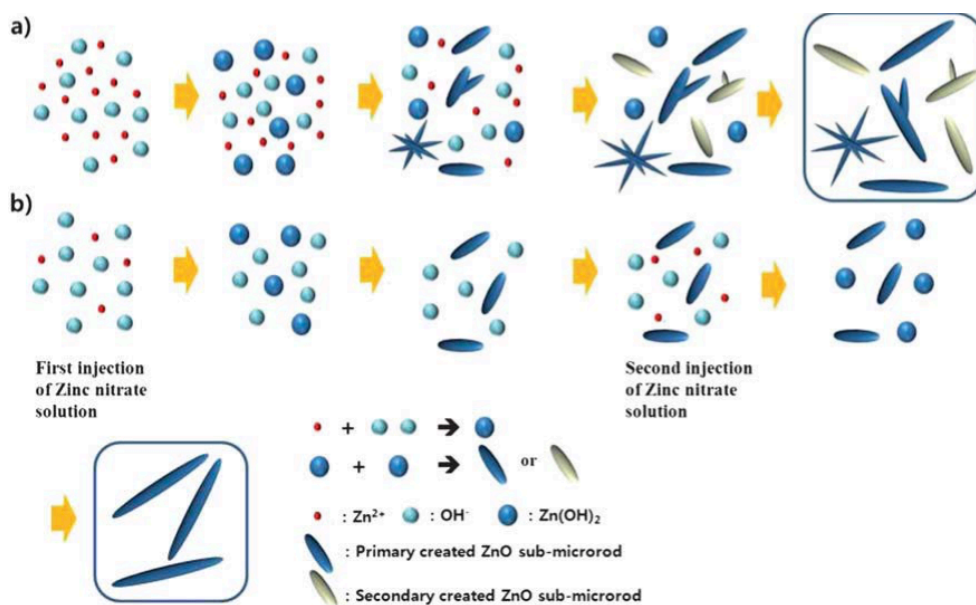


**Figure 2.20** Schematic diagram of ZnO NRs synthesis based on (a) one-pot heat-up process and (b) kinetically controlled process by a syringe pump (*from Ref. [37]* Copyright 2012 RSC Publishing Group).

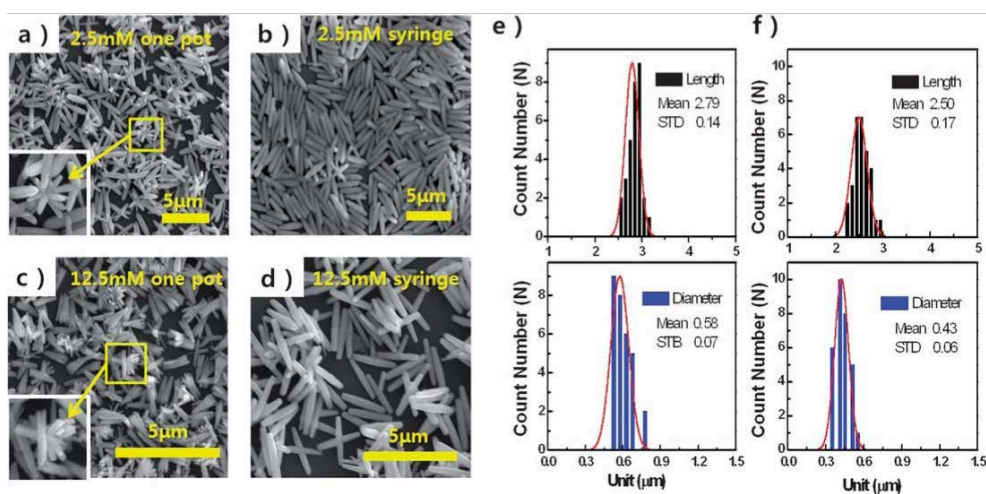


**Figure 2.21** FE-SEM images of ZnO NRs grown by (a) and (c) normal one-pot heat-up process and (b) and (d) kinetically controlled process. Size distribution of ZnO NRs using a kinetically controlled process with (e) 2.5mM and (f) 12.5mM chemical reagents concentration (zinc nitrate and HMTA) (*from Ref. [37]* Copyright 2012 RSC Publishing Group).

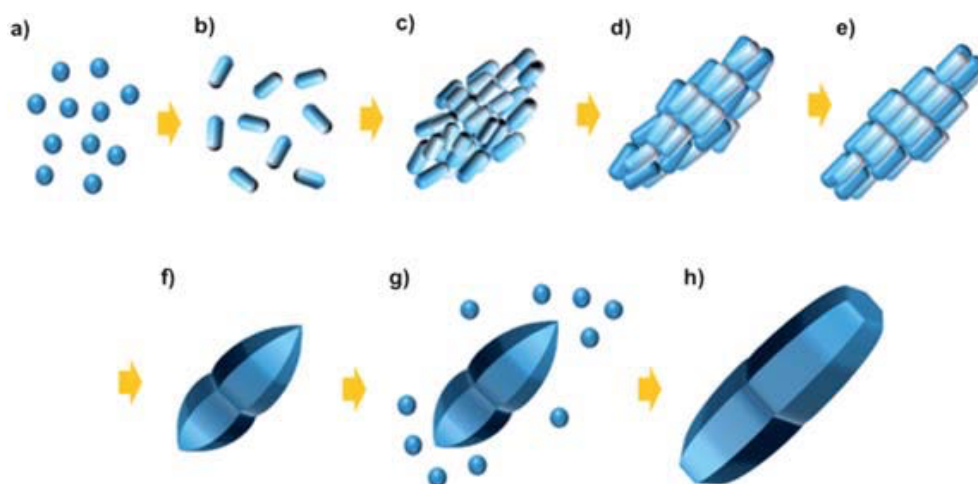


**Figure 2.22** Sequential steps for formation of ZnO NRs based on OA. (a) Zinc hydroxide complexes from zinc nitrate and HMTA, (b) Ellipsoidal ZnO NPs, (c) ZnO nanocrystal seed, (f) and (g) growth of ZnO nanocrystal by additional zinc hydroxide compounds, and (h) final ZnO NRs (*from Ref. [37] Copyright 2012 RSC Publishing Group*).

## 2.3 Piezoelectric devices

### 2.3.1 Principle of piezoelectric devices

In the early stage of PENG, the Schottky contact structure was the main idea for electricity generation.<sup>38</sup> By constituting of a Schottky contact in one side and an ohmic in other metal with the ZnO nanostructures in the middle, this could be introduce the piezoelectric potential changes under mechanical deformation of ZnO nanostructures. When the ZnO nanostructure, generally ZnO NW experiences mechanical deformation, the introduced piezoelectric potential changes the relative position of Fermi levels in two metal and electrons flow from the right electrode to the left electrode through the external circuit, as shown in figure 2.23 (b). The electrons are blocked by the Schottky barrier in the left side and then accumulated in left side metal-ZnO interface. However, when the mechanical deformation are relaxed, the accumulated electrons will flow back to the right electrode through the external circuit, as shown in figure 2.23 (c).

In point of the Schottky barrier, it is sometimes difficult to be stable and reproducible due to the sensitivity to the surrounding environment such as the atmosphere, humidity, etc. Moreover, this design restricts the large-size fabrication since the formation of contact between the ZnO nanostructure and metal is limited the size and also hard. Thus, formation of composite materials of piezoelectric nanstructure and dielectric such as PDMS and poly(methyl methacrylate) (PMMA) will solve the problem in mass production as well as the stability of Schottky contact. This sandwiched structure was firstly introduced in 2010 since the Schottky contact structure were developed in 2006. The hybridized ZnO NW are mixed with dielectric and sandwiched between two electrodes as

shown in figure 2.23 (d-f). When the composite piezoelectric material experiences the compression or tensile stress, the strain introduces aligned dipole moments in the dielectric matrix. In response, electrons transfer between two electrodes due to the built-in electric field as shown in figure 2.23 (e). However, when the strain is released, the electric dipole moment is vanished and the electrons will flow back through the external circuit as shown in figure 2.23 (f).

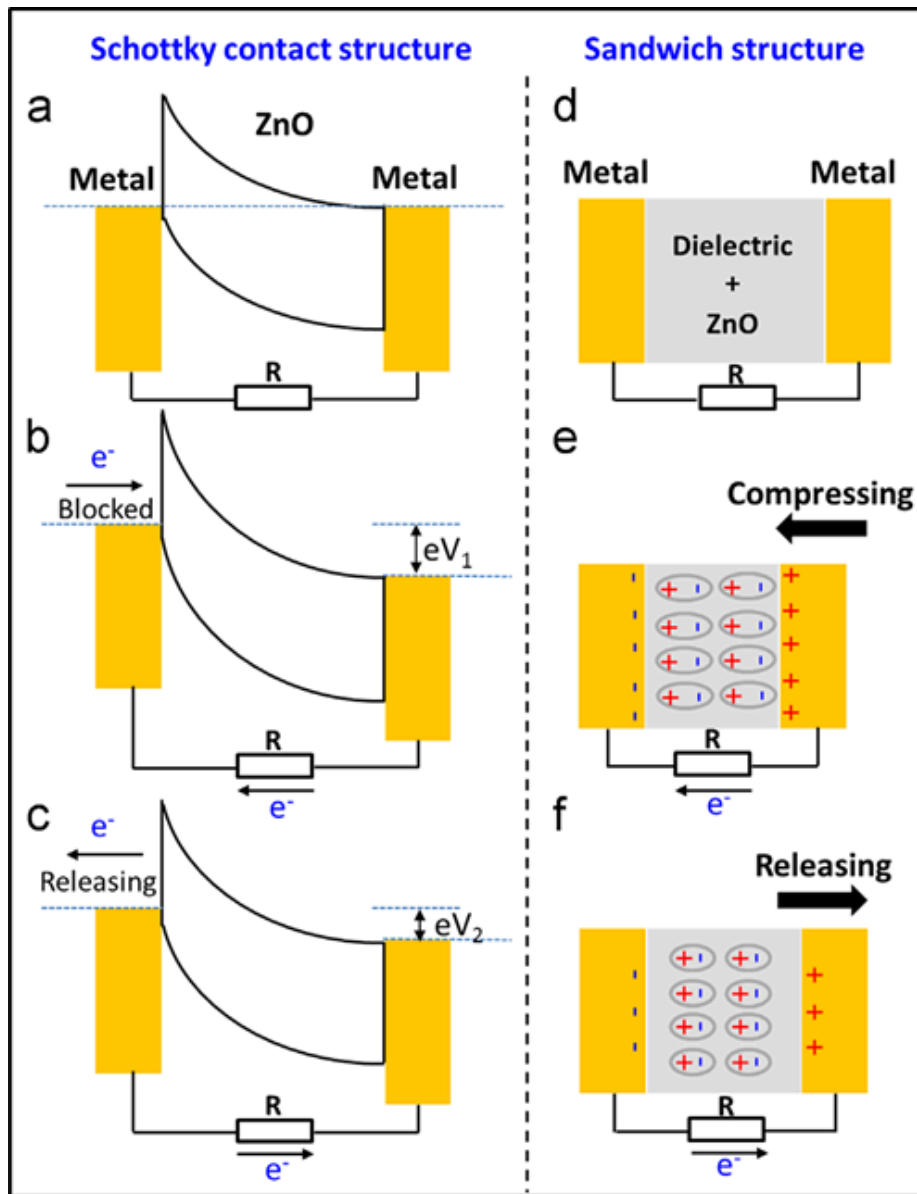


**Figure 2.23** Comparison of operational mechanism between piezoelectric devices based on Schottky contact structure and sandwich structure (from Ref. [38] Copyright 2015 Elsevier Publishing Group).



## 2.3.2 Types of piezoelectric devices

### 2.3.2.1 Nanogenerators

Nanogenerator (NG) is defined as a device, which converts mechanical energy into electricity primarily through piezoelectric effect of nanomaterials. The outstanding feature of NG is its simplistic and diverse structural properties, which can be applied to flexible and stretchable electronics. Thereby, the flexible electronics are applicable to many elastic applications such as wearable electronics, bendable displays and bio-inspired artificial skins. For the realization of fully flexible electronics, the devices should possess the ability to be bent, folded, twisted, and stretched, as well as maintain the original electronic and structural properties. Therefore, the key issue for flexible energy harvesting elements is to choose the suitable materials with good flexibility and mechanical stability. In many researches, nanostructured ZnO was utilized as a piezoelectric material. Especially, the one-dimensional structure of ZnO, such as ZnO NWs and NRs were applied because of the effective piezoelectric properties. At the initial stage of piezoelectric ZnO devices, the ZnO devices structure was designed as a lateral<sup>39,40,41,42</sup> or vertical<sup>43,44,45</sup> configuration as shown in figure 2.24 and 2.25. The bending of flexible substrate induces a uniaxial tensile strain in the lateral (horizontal) ZnO NWs, resulting the piezoelectric potential along the wire, which drives electron inside ZnO NW to flow through the external circuit. Moreover, the output characteristics of lateral ZnO structured piezoelectric devices can be enhanced by integrating large numbers of NWs in a parallel configuration on a single platform. This laterally aligned piezoelectric ZnO NW device is applicable to meet the requirement of horizontal structured devices such as bendable patches and muscle-

driven elements.

On the other hands, the vertical structured NG used vertically as-grown ZnO NWs along the c-axis with (0001) polar direction. This ZnO NWs or NRs are generally grown in solution-process at low temperature under 100°C on substrates of any shape and any material. Therefore, this vertically grown ZnO used piezoelectric device is simple, economic. This vertically aligned ZnO, however, has a contact problem such as contact leakages and high resistance with the top electrode due to the rigid electrode configuration. To solve this problem, carbon nanotube (CNT) and graphene were adopted to use as a top electrode for flexible configuration. This flexible harvester can be integrated into lots of fabric-based applications.

Lastly, ZnO NW has been also utilized for fiber-based PENG (figure 2.26), which generally fabricated to convert vibration into electricity.<sup>46,47,48</sup> The ZnO NW are radially grown around textile fibers and a sliding motion between the two fibers in NG produces the power output owing to the deflection of ZnO NWs. This fiber-based PENG shows distinct advantages for fabrication of flexible and wearable power source which build the basic structure for smart clothes applications.

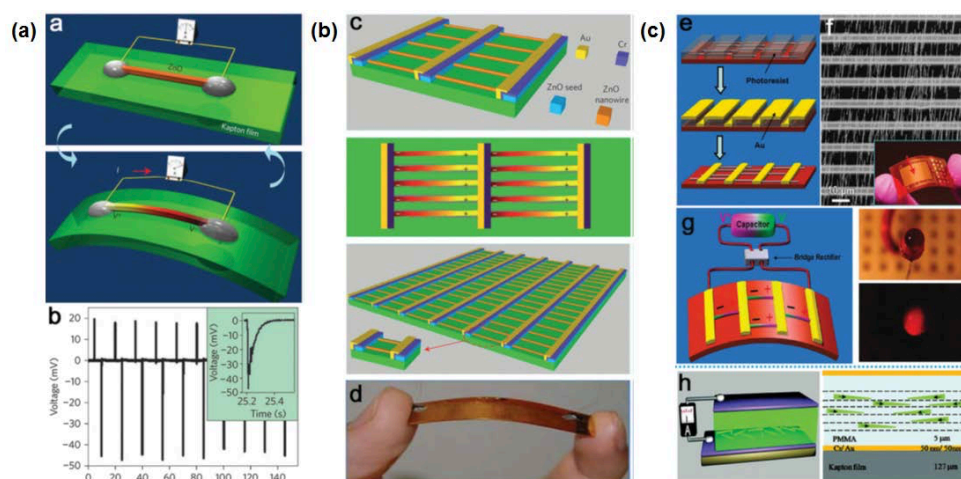


**Figure 2.24** Horizontal ZnO NW array based flexible PENGs. (a) PENG with single ZnO NW on a flexible substrate (*from Ref. [39] Copyright 2009 Nature Publishing Group*). (b) PENG with integration of lateral ZnO NW arrays (*from Ref. [40] Copyright 2010 Nature Publishing Group*). (c) PENG with randomly-laterally-aligned ZnO NWs (*from Ref. [41] Copyright 2010 ACS Publishing Group*). (d) PENG with rational unipolar assembly of conical ZnO NWs (*from Ref. [42] Copyright 2010 ACS Publishing Group*).

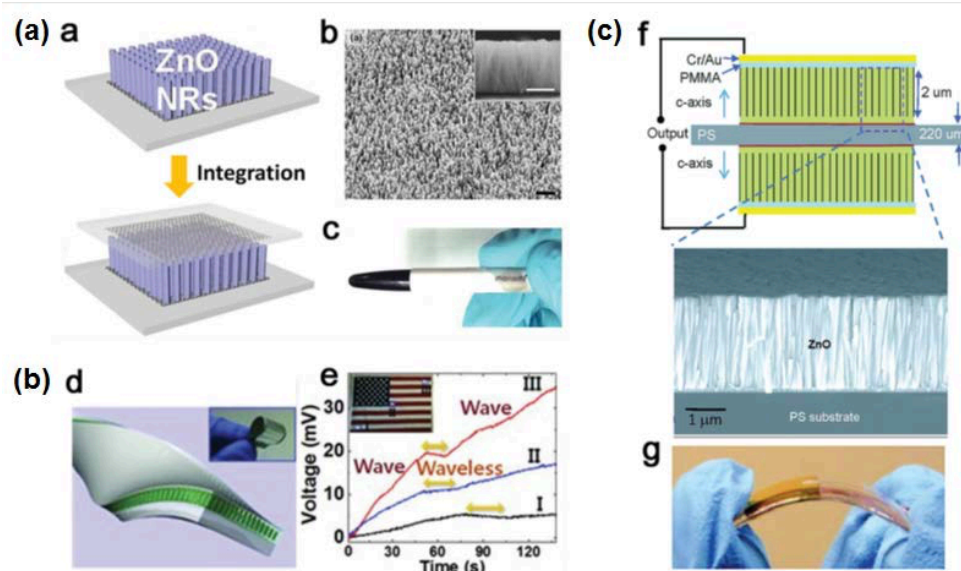


**Figure 2.25** Vertical ZnO NW array based flexible PENGs. (a) Fully rollable PENG based on graphene substrate with vertical ZnO arrays (*from Ref. [43] Copyright 2010 Wiley Publishing Group*). (b) Super-flexible PENG based on ultrathin Al foil with vertical ZnO NW arrays as an active deformation sensor (*from Ref. [44] Copyright 2011 ACS Publishing Group*). (c) PENG with randomly-laterally-aligned ZnO NWs. (d) High-output PENG made of a free cantilever beam with multi-stacked ZnO NW structure (*from Ref. [45] Copyright 2013 Wiley Publishing Group*).

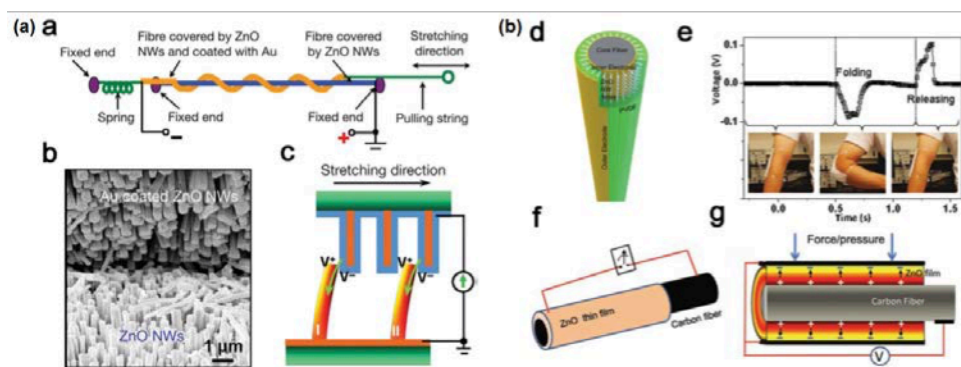


**Figure 2.26** ZnO fiber based flexible PENGs. (a) PENG with radially coiled ZnO NWs around textile fibers (*from Ref. [46] Copyright 2008 Nature Publishing Group*). (b) hybrid-fiber PENG consists of ZnO NWs and PVDF film for use as a human elbow patch (*from Ref. [47] Copyright 2012 Wiley Publishing Group*). (d) PENG with ZnO thin film arrays on the surface of carbon fiber (*from Ref. [48] Copyright 2011 Wiley Publishing Group*).

### 2.3.2.2 Sensors

With same principle as the NG, piezoelectric sensors also convert the mechanical energy into electricity using piezoelectrically active materials. However, depends on the magnitude of piezoelectric potential induced by the mechanical strain on the piezoelectric materials, the output power is differed and can be a signal of the intensity of the applied force or strain onto the piezoelectric devices. Using hollow structure of ZnO as shown in figure 2.27 (a), asymmetric ZnO structure can be fabricated and can detect the intensity difference of pressure stress.<sup>49</sup> The vertically aligned ZnO NW based device can be utilized as a deformation sensor by detecting the wrinkling of a human face (figure 2.27 (b)).<sup>50</sup> Moreover, vertically aligned configuration with PDMS filling can also utilized as a transportation monitoring system by detecting the load of passing cars on the road from the output difference (figure 2.27 (c)).<sup>51</sup> For unables, also researcher developed a piezoelectric sensor function as a hair cell to stimulate the auditory nerves in human ears (figure 2.27 (d)).<sup>52</sup> Finallym, the piezoelectric sensor can be applied as a sound sensor or climate sensor by detecting the sound frequencies and pressure of the water drops as shown in figure 2.27 (e) and (f).<sup>53,54</sup>

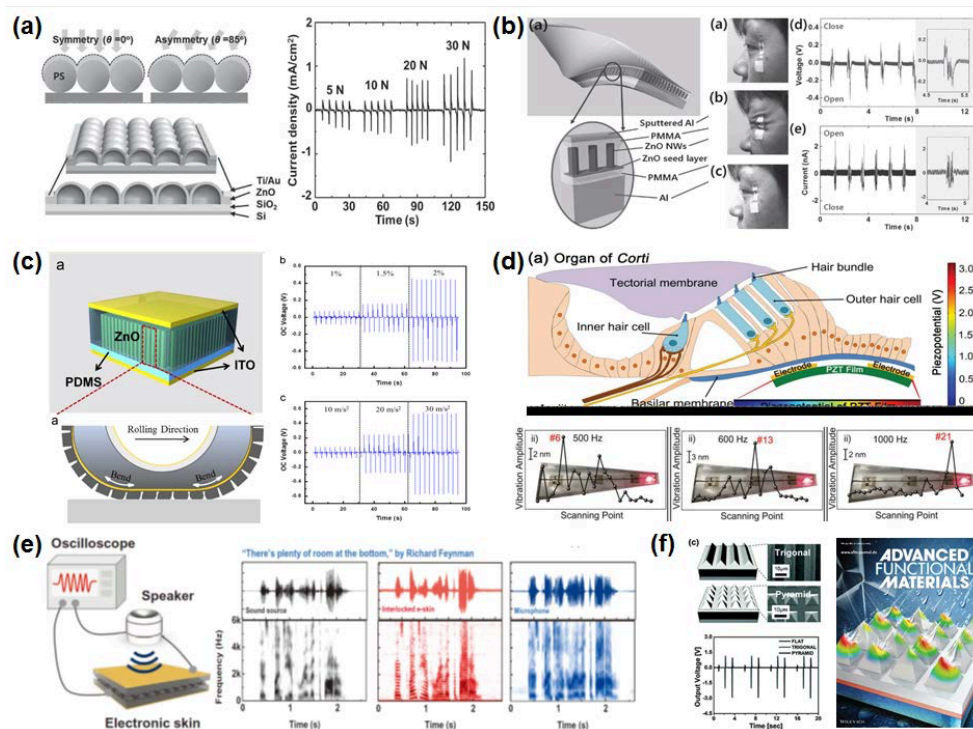


**Figure 2.27** Various piezoelectric sensors using diverse piezoelectric nanomaterials such as (a) pressure sensor (from Ref. [49] Copyright 2014 Wiley Publishing Group), (b) deformation sensor (from Ref. [50] Copyright 2013 Wiley Publishing Group), (c) transportation monitoring system (from Ref. [51] Copyright 2013 Elsevier Publishing Group), (d) biosensor (from Ref. [52] Copyright 2014 Wiley Publishing Group), (e) sound sensor (from Ref. [53] Copyright 2015 Science Publishing Group), and (f) climate sensor (from Ref. [54] Copyright 2015 Wiley Publishing Group).

## 2.4 References

- [1] J. P. Roberts, P. Popper, Piezoelectric ceramics, Academic press, LONDON and NEW YORK, London **2012**.
- [2] APC International, Ltd., Piezoelectric ceramics: principles and applications, APC International, Ltd., Pennsylvania, second edition.
- [3] J. Erhart, Phys. Educ. **2013**, 48, 438.
- [4] P. T. Moseley, A. J. Crocker, Sensor materials, IOP Publishing Ltd, UK, **1996**.
- [5] B. R. Singh, Global warming: impacts and future perspective, Intech, **2012**.
- [6] R. S. Dahiya, M. Valle, Robotic tactile sensing, Springer Dordrecht, Heidelberg New York London, **2013**.
- [7] C. A. Gallo, F. L. Tofoli, D. Rade, and V. Steffen Jr., J. Vib. Control **2012**, 18, 1650.
- [8] C. R. Bowen, H. A. Kim, P. M. Weaver, and S. Dunn, Energy Environ. Sci. **2014**, 7, 25.
- [9] F. Li, L. Wang, L. Jin, D. Lin, J. Li, S. Li, Z. Xu, S. Zhang, IEEE Trans. Ultrason. Ferroelectr. Freq. Control **2015**, 62, 18.
- [10] T. R. Shrout, W. Huebner, C. A. Randall, A. D. Hilton, Ferroelectrics **1989**, 93, 361.
- [11] T. S. Herng, A. Kumar, C. S. Ong, Y. P. Feng, Y. H. Liu, K. Y. Zeng, J. Ding, Sci. Rep. **2012**, 2, 587.
- [12] J. Zhang, C. Wang, C. Bowen, Nanoscale **2014**, 6, 13314.
- [13] J. Aufort, O. Aktas, M. A. Carpenter, E. K. H. Salje, Amer. Miner. **2015**, 100, 1165.
- [14] J. Chang, M. Dommer, C. Chang, L. Lin, Nano Energy **2012**, 1, 356.



- [15] K. S. Ramadan, D. Sameoto, S. Evoy, Smart Mater. Struct. **2014**, 23, 033001.
- [16] A. P. Barranco, Ferroelectric materials - synthesis and characterization, Intech, **2015**.
- [17] Y. Qi, M. C. McAlpine, Energy Environ. Sci. 2010, 3, 1275.
- [18] S. Xu, Z. L. Wang, Nano Res. **2011**, 4, 1013.
- [19] Z. L. Wang, Mat. Sci. Eng. R **2009**, 64, 33.
- [20] Z. L. Wang, MRS Bulletin **2012**, 37, 814.
- [21] C. Jagadish, S. J. Pearton, Zinc oxide bulk, thin film and nanostructures, Elsevier, **2006**.
- [22] B. Kumar, S. –W. Kim, Nano Energy **2012**, 1, 342.
- [23] Y. H. Zhang, J. W. Hong, B. Liu, D. N. Fang, Nanotechnology **2012**, 21, 015701.
- [24] K. Momeni, G. M. Odegard, R. S. Yassar, Acta. Mater. **2012**, 60, 5117.
- [25] R. Agarawal, H. D. Espinosa, Nano Lett. **2011**, 11, 786.
- [26] J. Zhang, C. Y. Wang, R. Chowdhury, S. Adhikari, Scr. Mater. **2013**, 68, 627.
- [27] M. H. Zhao, Z. L. Wang, S. X. Mao, Nano Lett. **2004**, 4, 587.
- [28] F. Xu, Q. Qin, A. Mishra, Y. Gu, Y. Zhu, Nano Res. **2010**, 3, 271.
- [29] J. H. He, C. H. Ho, C. W. Wang, Y. Ding, L. J. Chen, Z. L. Wang, Cryst. Growth Des. **2009**, 9, 17.
- [30] J. Zhang, L. D. Sun, J. L. Yin, H. L. Su, C. S. Liao, C. H. Yan, Chem. Mater. **2002**, 14, 4172.
- [31] B. Cheng, E.T. Samulski, Chem. Commun. **2004**, 986.
- [32] H. L. Cao, X. F. Qian, Q. Gong, W. M. Du, X. D. Ma, Z. K. Zhu, Nanotechnology **2006**, 17, 3632.
- [33] B. Liu, H. C. Zeng, J. Am. Chem. Soc. **2003**, 125, 4430.

- [34] X. M. Hou, F. Zhou, Y. B. Sun, W. M. Liu, *Mater. Lett.* **2007**, 61, 1789.
- [35] T. Alammari, A. V. Mudring, *Mater. Lett.* **2009**, 63, 732.
- [36] S. T. Meyers, J. T. Anderson, C. M. Hung, J. Thompson, J. F. Wager, D. A. Keszler, *J. Am. Chem. Soc.* **2008**, 130, 17605.
- [37] W. S. Jang, T. I. Lee, J. Y. Oh, S. H. Hwang, S. W. Shon, D. H. Kim, Y. Xia, J. M. Myoung, H. K. Baik, *J. Mater. Chem.* **2012**, 22, 20719
- [38] Y. Hu, Z. L. Wang, *Nano Energy* **2015**, 14, 3.
- [39] R. Yang, Y. Qin, L. Dai, Z. L. Wang, *Nat. Nanotechnol.* **2009**, 4, 34.
- [40] S. Xu, Y. Qin, D. Xu, Y. Wei, R. Yang, Z. L. Wang, *Nat. Nanotechnol.* **2010**, 5, 466.
- [41] G. Zhu, R. Yang, S. Wang, Z. L. Wang, *Nano Lett.* **2010**, 10, 3151.
- [42] Y. Hu, Y. Zhang, C. Xu, G. Zhu, Z. L. Wang, *Nano Lett.* **2010**, 10, 5025.
- [43] D. Choi, M. -Y. Choi, W. M. Choi, H. -J. Shin, H. -K. Park, J. -S. Seo, J. Park, S. -M. Yoon, S. J. Chae, Y. H. Lee, S. -W. Kim, J. -Y. Choi, S. Y. Lee, J. M. Kim, *Adv. Mater.* **2010**, 22, 2187.
- [44] Y. Hu, Y. Zhang, C. Xu, L. Lin, R. L. Snyder, Z. L. Wang, *Nano Lett.* **2011**, 11, 2572.
- [45] S. Lee, S. -H. Bae, L. Lin, Y. Yang, C. Park, S. -W. Kim, S. N. Cha, H. Kim, Y. J. Park, Z. L. Wang, *Adv. Funct. Mater.* **2013**, 23, 2445.
- [46] Y. Qin, X. Wang, Z. L. Wang, *Nature* **2008**, 451, 809.
- [47] M. Lee, C. Y. Chen, S. Wang, S. N. Cha, Y. J. Park, J. M. Kim, L. J. Chou, Z. L. Wang, *Adv. Mater.* **2012**, 24, 1759.
- [48] Z. Li, Z. L. Wang, *Adv. Mater.* **2011**, 23, 84.
- [49] J. Chun, K. Y. Lee, C. -Y. Kang, M. W. Kim, S. -W. Kim, J. M. Baik, *Adv. Funct. Mater.* **2014**, 24, 2038.

- [50] S. Lee, S. -H. Bae, L. Lin, Y. Yang, C. Park, S. -W. Kim, S. N. Cha, H. Kim, Y. J. Park, Z. L. Wang, *Adv. Funct. Mater.* **2013**, 23, 2445.
- [51] L. Lin, Y. Hu, C. Xu, Y. Zhang, R. Zhang, X. Wen, Z. L. Wang, *Nano Energy* **2013**, 2, 75.
- [52] H. S. Lee, J. Chung, G. -T. Hwang, C. K. Jeong, Y. Jung, J. -H. Kwak, H. Kang, M. Byun, W. D. Kim, S. Hur, S. -H. Oh, K. J. Lee, *Adv. Funct. Mater.* **2014**, 24, 6914.
- [53] J. Park, M. Kim, Y. Lee, H. S. Lee, H. Ko, *Sci. Adv.* **2015**, 1, e1500661.
- [54] J. -H. Lee, H. -J. Yoon, T. Y. Kim, M. K. Gupta, J. H. Lee, W. Seung, H. Ryu, S. -W. Kim, *Adv. Mater.* **2015**, 25, 3203.

## **Chapter 3. ZnO thin film piezoelectric nanogenerator**

### **3.1 Introduction**

Energy harvesting from ambient environments is an attractive issue in scientific and industrial fields for the purpose of building self-powered systems. A PENG is one promising way to scavenge the energy from various sources, including body movements, waves, sounds, air/liquid pressures, and heartbeats.<sup>1,2,3,4</sup> Converting system of these mechanical energies into electrical power can be applied for the fabrication of various advanced devices such as mobile electronics, muscle-driven elements and self-powered body-implantable devices.<sup>1,5</sup>

Bent or distortional force-changes such as bending or rolling motions of the piezoelectric element are required for future energy harvesters such as wearable human patches, flexible mobile electronics, and muscle-driven energy scavengers. Thin film based NGs have proven to be suitable for scavenging irregular mechanical sources from bending or rolling motions.<sup>6</sup> Recently, various kinds of perovskite thin films such as PZT and BT have been utilized for piezoelectric generation.<sup>7,8</sup> For example, a NG with thin film of BT was reported by Park et al. Perovskite BT thin films were deposited by radio frequency magnetron sputtering (rf-sputtering) and transferred to a flexible substrate after an annealing process at a high temperature (700°C).<sup>7</sup> Since such high temperature processes have not permitted direct application to flexible and plastic substrates, the transfer process of thin films is essential. On the other hand, low-temperature- treated thin film does not require the cumbersome transfer of a thin film from inorganic substrates such as silicon or sapphire wafers to plastics. Thus, there is a need for a low temperature process for thin film based PENGs.

Wurtzite nanostructures such as ZnO and GaN are the other piezoelectric materials that can be applied in piezoelectric energy generation by the non-centrosymmetric structure in the crystalline phase. ZnO is a particularly appealing material for nanostructure-based energy generators because of its coupling effect of piezoelectrical and semiconducting properties, abundant configurations of nanostructures, transparency, and biocompatibility.<sup>9</sup> Rf-sputtered room-temperature-treated ZnO thin film was recently utilized as a piezo-material in a piezoelectric nanounit.<sup>10,11</sup> However, the high energetic ions induced by the plasma sputtering process may cause surface damage as well as defect formation in the deposited film.<sup>12</sup> Additionally, vacuum process and high-cost equipment of sputtering system with complex optimum condition such as pressure, temperature and rf power are required for thin film PENG to perform well.

In this paper, we first demonstrate the fabrication of an all-solution-processed flexible thin film PENG using simple aqueous ZnO ink as a thin film. A low-temperature process was adopted to deposit piezoelectric ZnO thin film directly onto the plastic substrates without any thermal damage. Moreover, screen-printing of silver paste was applied on the top of the PENG for a top electrode formation.<sup>13</sup> This printing method has applicability on any irregular or cylindrical surface using a simple coating method through stencil mesh. Our all solution-processed flexible thin film PENG including the ZnO thin film and the silver electrode has several advantages: it is a simple and low-cost process, which can be deposited in large area with mass production, and the air- stable method does not require any cumbersome conditions.<sup>14</sup> Also, the flexible thin film PENG based on solution processed ZnO film in this study allowed the piezoelectric energy to be generated through rolling motion as well as muscle stretching because of its flexible ultrathin

structures. The ZnO thin film exhibits a high elasticity and resistance to mechanical fatigue of the devices. Solution- processed p-type polymer blend and hole transport layer were also interlaid to enhance the output power of the PENG.<sup>15</sup> The morphology and crystalline phase of the ZnO nanostructure were also investigated.

## 3.2 Experimental

Based on the previous report, the ZnO solution was prepared using the simple inorganic hydroxo-condensation method, which was conducted at a low temperature with rapid reactivity because of the intrinsic properties of aqueous ZnO chemistry.<sup>16,17</sup> The process and mechanism for ZnO thin film fabrication with solution-processibility and a low sintering temperature were previously reported (see Method S1). The ZnO solution was spin-coated to indium tin oxide (ITO)/polyethylene terephthalate (PET) film and annealed at 120°C. The spin-coating and heating processes were repeated one more time to fabricate enough dense film of ZnO for short-circuit prevention. Then, the blend of poly(3-hexylthiophene-2,5-diyl)/phenyl-C61-butyric acid methyl ester) P3HT/PCBM polymer solution was deposited to enhance both the piezoelectric potential by p-n junction formation and the effective electron pathway by nanoscale heterojunctions.

Poly(3,4-ethylenedioxythiophene)-poly(styrenesulfonate) (PEDOT:PSS) was spin-coated as a hole transport layer onto the top of the p-type polymer. Finally, silver paste was deposited using a screen printer for a formation of top electrode. All the process is depicted in figure 3.1.

### 3.2.1 Preparation of ZnO thin film

A Zn solution was prepared using 10ml of zinc nitrate hexahydrate ( $\text{Zn}(\text{NO}_3)_2 \cdot 6\text{H}_2\text{O}$ ) [Alfa Aesar, 99.9%] solution (0.5M) dissolved in de-ionized (DI) water. Titration of 10ml NaOH solution (2.5M) into the nitrate form was conducted for 10min with vigorous stirring. The sediment was then centrifuged four times with DI-water for 5min at 5000rpm in each step to reduce the concentrations of

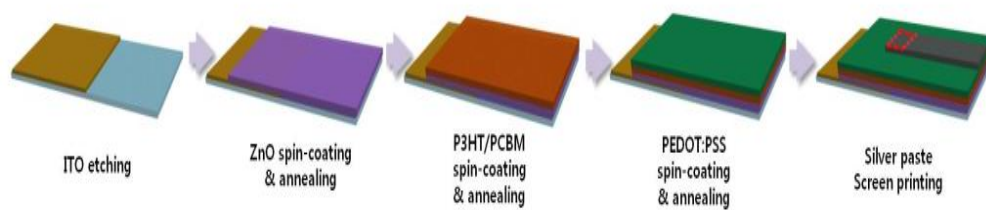
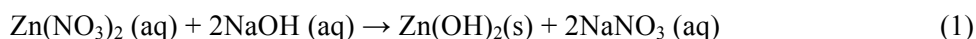


**Figure 3.1** Fabrication process of the all-solution-processed flexible thin film PENG with an active area of  $0.8 \times 0.5 \text{ cm}^2$ . Further details of this fabrication process are written in the experimental section.

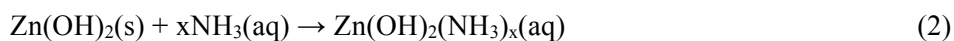


$\text{Na}^+$  and  $\text{NO}_3^-$  in minimal quantities. The final hydroxide form was suspended in 20ml of 6.6M ammonia water ( $\text{NH}_3$  (aq)) [Duksan Pure Chemicals Co., Ltd.] and 25ml of DI-water to obtain a ZnO precursor. Part of the ITO / PET [Sigma Aldrich, sheet resistance:  $60\Omega/\text{square}$ , ITO-film thickness: 100nm] was etched with hydrochloric acid to exclude it from the active area, causing a piezoelectric effect. The as-prepared precursor solution was spin-coated at 3000 rpm for 30 s onto ITO/PET film that had been treated in ultraviolet ozone. The spin-coated film was then sintered at 120 °C for 1h and the spin-coating and heating steps were repeated one more time to obtain dense film ZnO.

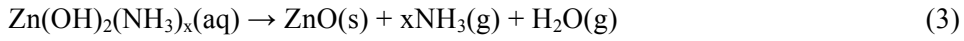
Based on the previous report, the ZnO solution was prepared using the simple inorganic hydroxo-condensation method that is conducted at a low temperature with rapid reactivity because of the intrinsic chemical properties of aqueous ZnO. The process and mechanism for ZnO thin film fabrication with solution-processibility and a low sintering temperature were previously reported.<sup>19</sup> Before obtaining a dissolved form of zinc oxide, aqueous sodium hydroxide was dropped into the zinc nitrate solution followed by this equation.



The hydroxide replaced the nitrate anion so that the purity of zinc hydroxide precipitate was increased. Then, the residual sodium and nitrate ions in the zinc-hydroxide sediment were removed by four-time centrifugations. In the final agitation step, the sediment was dissolved in the ammonium hydroxide solution to form the ZnO precursor as follows.



The ZnO solution was spin-coated to ITO/PET film and annealed at 120 °C for 1h to volatilize ammine and water from an ammine-hydroxo zinc solution.



Finally, the ZnO thin film could be obtained from the sintering process followed by equation (3). The whole process is presented in figure 3.2.

### **3.2.2 Fabrication of ZnO thin film piezoelectric nanogenerator**

ZnO film was deposited onto a bottom electrode, ITO/PET film as described above. The blend of P3HT/PCBM with 1:0.8 weight ratio in 2ml chlorobenzene solution (P3HT : PCBM : chlorobenzene = 15 mg : 12 mg : 2 ml) was spin-coated in a glove box to prevent any degradation of the P3HT/PCBM solution (3000rpm for 40s with an acceleration speed at 500 rpm for 2 s and dried at 120 °C for 10min). Then, the filtered hole transport layer PEDOT:PSS solution was spin-coated at 3000rpm for 40s (acceleration speed at 500 rpm for 2 s) and dried at 120 °C for 10min. The top electrode of the PENG was then prepared by screen printing of the silver paste on top of the PEDOT:PSS layer to form a Schottky- contact. The silver paste was coated on the stencil and then pressed through the mesh using a squeegee to force the ink into the mesh openings to transfer the silver paste. Electric wires were fixed to each top and bottom electrode to connect the PENG with the measurement devices.

### **3.2.3 Characterizations**

The morphology and crystalline phase of the ZnO nanostructure were investigated by a field-emission scanning electron microscope (FE-SEM) [Hitachi S-4800], an

atomic force microscope (AFM) [PSIA XE-150], a high resolution scanning transmission electron microscope (HRSTEM) [JEM-2100F] equipped with an energy dispersive X-ray spectrometer (EDX) and fast Fourier transform (FFT) analysis, X-ray diffraction (XRD) and grazing incidence X-ray diffraction (GIXRD). To detect currents and voltages generated by flexible ZnO PENG, a Keithley 6485 Picoammeter and Keithley 2182A Voltammeter were used. To ensure regular and continuous electricity generation, rolling and bending testers [Z-tec] were used.

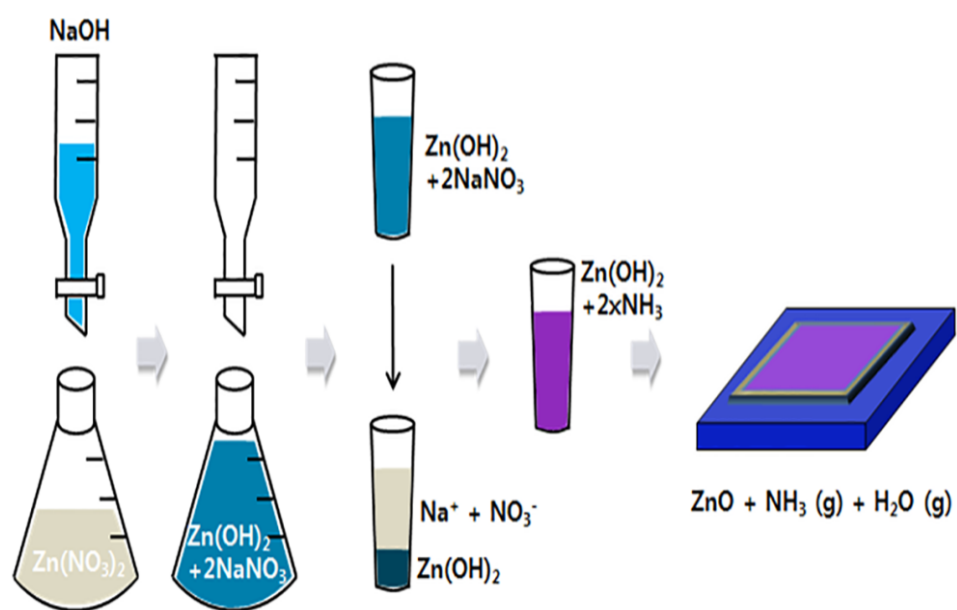


**Figure 3.2** Preparation of ZnO precursor and thin film.

### 3.3 Results and discussion

#### 3.3.1 Characteristics of ZnO thin film

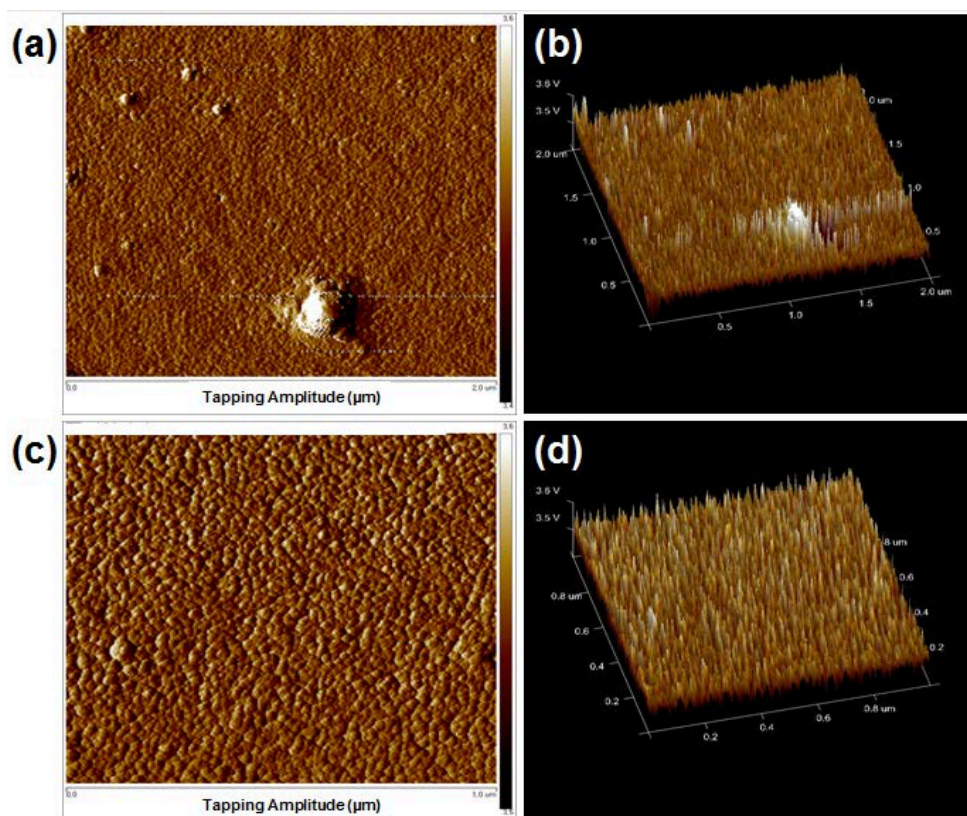
For flat and uniform ZnO thin film, spin-coating of ZnO precursor was conducted through preliminary experiments with several conditions. The ZnO precursor solution was spin-coated one and two times each and annealed at 120 °C for 1h to volatilize ammine and water from an ammine-hydroxo zinc solution. Non-uniform film of ZnO with protruding portion was observed as a result of the one-time spin-coating as shown in figure 3.3 (a) and (b). On the other hands, after two times spin-coating, the ZnO thin film was remarkably smooth with a small protruding surface structure, which indicates a c-axis favorable ZnO thin film (figure 3.3 (c) and (d)). Therefore, two-times spin-coating of ZnO precursor solution was conducted for formation of good conact with top layers of the p-type polymer and the hole transport layer as well as the top electrode.

Figure 3.4 shows a schematic of all-solution-processed PENG with the p-type polymer and the hole transport layer on a flexible substrate. Since the low-temperature, solution processed piezoelectric material and electrode could be directly deposited onto a plastic substrate, the piezoelectric nanounit was fully flexible without a transfer process. FE-SEM in figure 3.5 was conducted to observe the thickness of each layer in the PENG. The ZnO film was about 87 nm thick, and a thickness of about 25 nm of p-type polymer blend and 15 nm of hole transport layer were measured using scale bars. To characterize the surface morphology and crystalline phase of ZnO, an AFM and a HRSTEM were performed, as shown in figure 3.6 and 3.7. The AFM image in figure 3.6 shows the top view of a protruding surface structure, which indicates a configuration of a ZnO nano-grain

structure in the ZnO thin film. It can be shown from the HRSTEM images that crystal lattices of ZnO are obviously visible, which are mainly constituted of an (002)-oriented ZnO structure. From the result of fast FFT pattern in figure 3.7, ZnO NRs has the preferential growth direction along the c-axis orientation. An examination of an EDX in figure 3.8 was also conducted and denotes that the presence of only Zn and O atoms are detected from the ZnO layer. Therefore, the solution-processed ZnO thin film is constituted by a ZnO nano-grain structure with a protruding configuration on the top surface, which can be deformed by an external force in the same manner as the previously reported vertical ZnO NRs based PENGs with an alternating-current (AC) mode.<sup>18</sup> In addition, the dense and continuous structure of ZnO thin film diminishes the electrical leakage or loss resulting from poor contact between electrodes and piezoelectric materials.

Figure 3.9 (a) shows the XRD pattern of the ZnO thin film deposited onto ITO film. An increment of intensity of peak around  $35^\circ$  was observed, indicating the c-axis orientation in (002) direction. To confirm the crystalline phase of the ZnO thin film, we also profiled the GIXRD analysis at the ZnO deposited ITO layer with annealing temperature of  $90^\circ\text{C}$  and  $150^\circ\text{C}$  (black =  $90^\circ\text{C}$ , red =  $150^\circ\text{C}$ ) (figure 3.9 (b)). A diffraction peak near 2.4 was observed for both  $90^\circ\text{C}$  and  $150^\circ\text{C}$  annealing temperature and can assume that the ZnO thin film for  $120^\circ\text{C}$  heating treatment would have a diffraction peak at the same spot. Otherwise, the diffraction peak near 2.4 indicates that the ZnO thin film was deposited in an epitaxial direction along the c-axis orientation with a (002) lattice plane. Also, the HRSTEM image in figure 3.7 has already showed the crystalline lattice of ZnO film, presenting also the crystalline phase of ZnO thin film with the tendency for c-axis orientation. Therefore, we confirm that the ZnO thin film fabricated by our group have good

crystalline properties with one-direction oriented polarization despite of the low process temperature.



**Figure 3.3** AFM images of (a-b) one-time and (c-d) two-times spin-coated ZnO thin films.



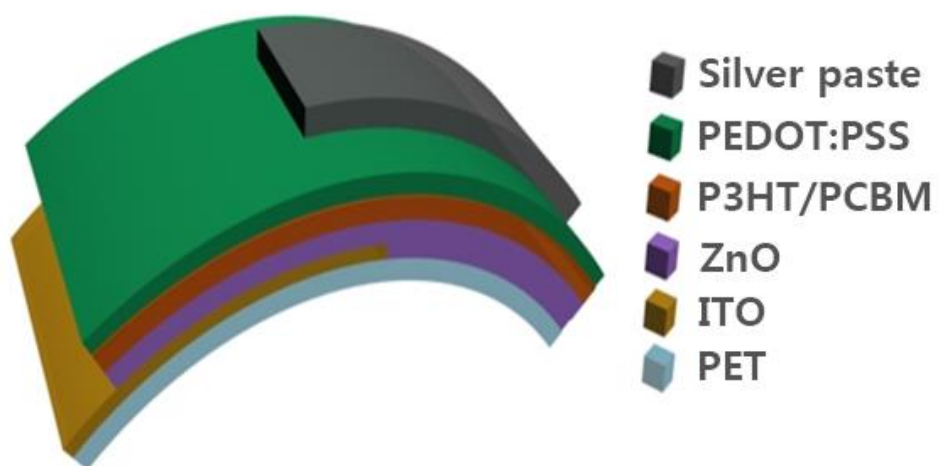


**Figure 3.4** A schematic diagram of the all-solution-processed flexible thin film PENG on a plastic substrate.

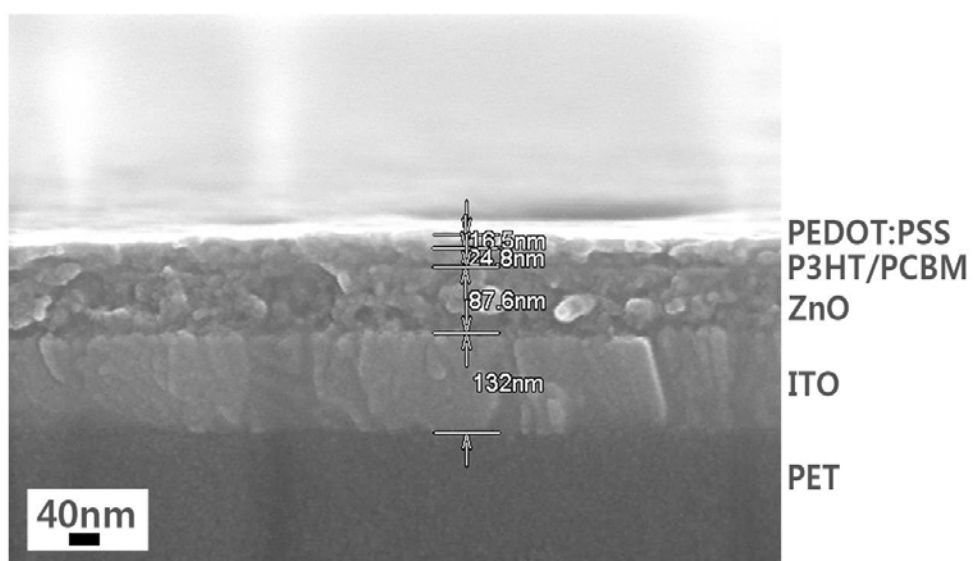


**Figure 3.5** Cross-sectional FE-SEM image of ITO-ZnO-P3HT/PCBM-PEDOT:PSS stacks.

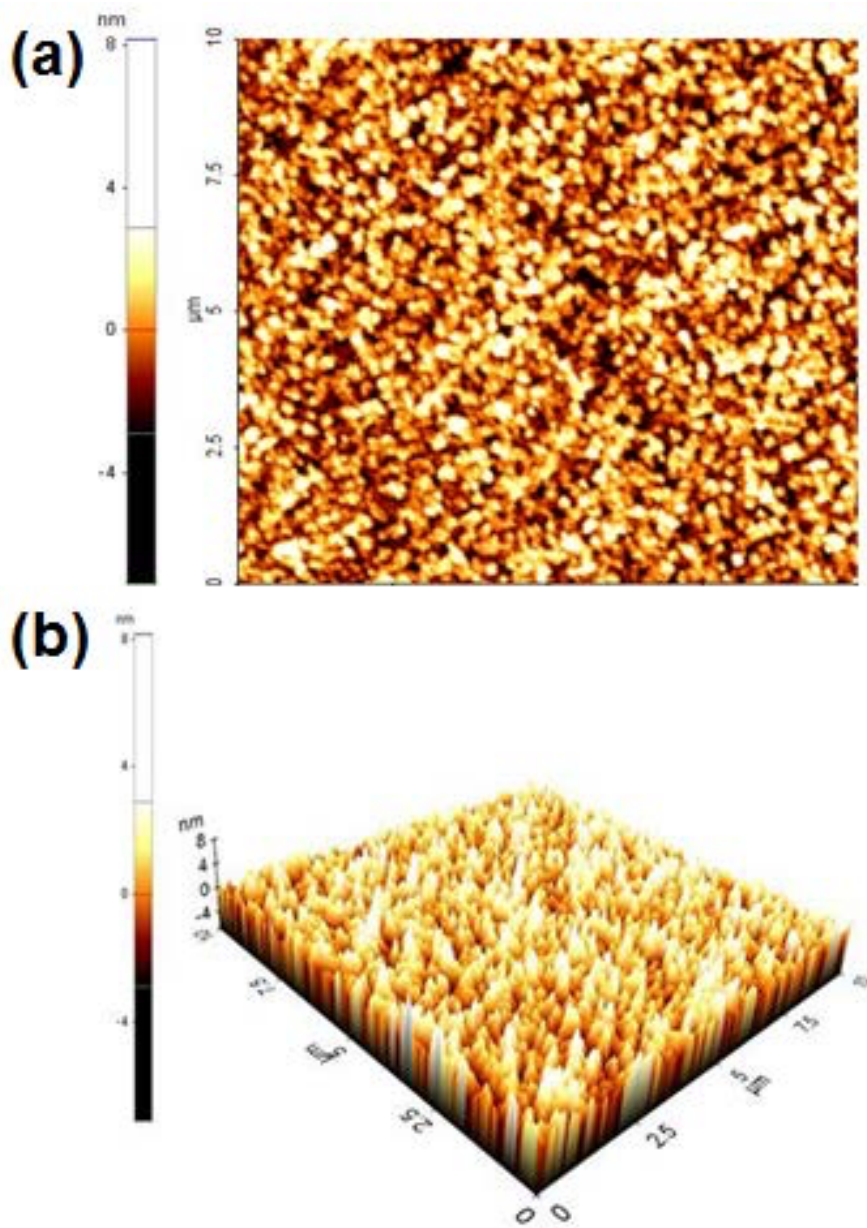


**Figure 3.6** AFM images of the ZnO thin film on ITO/PET film. Average surface roughness ( $R_a$ ) is 1.47nm.

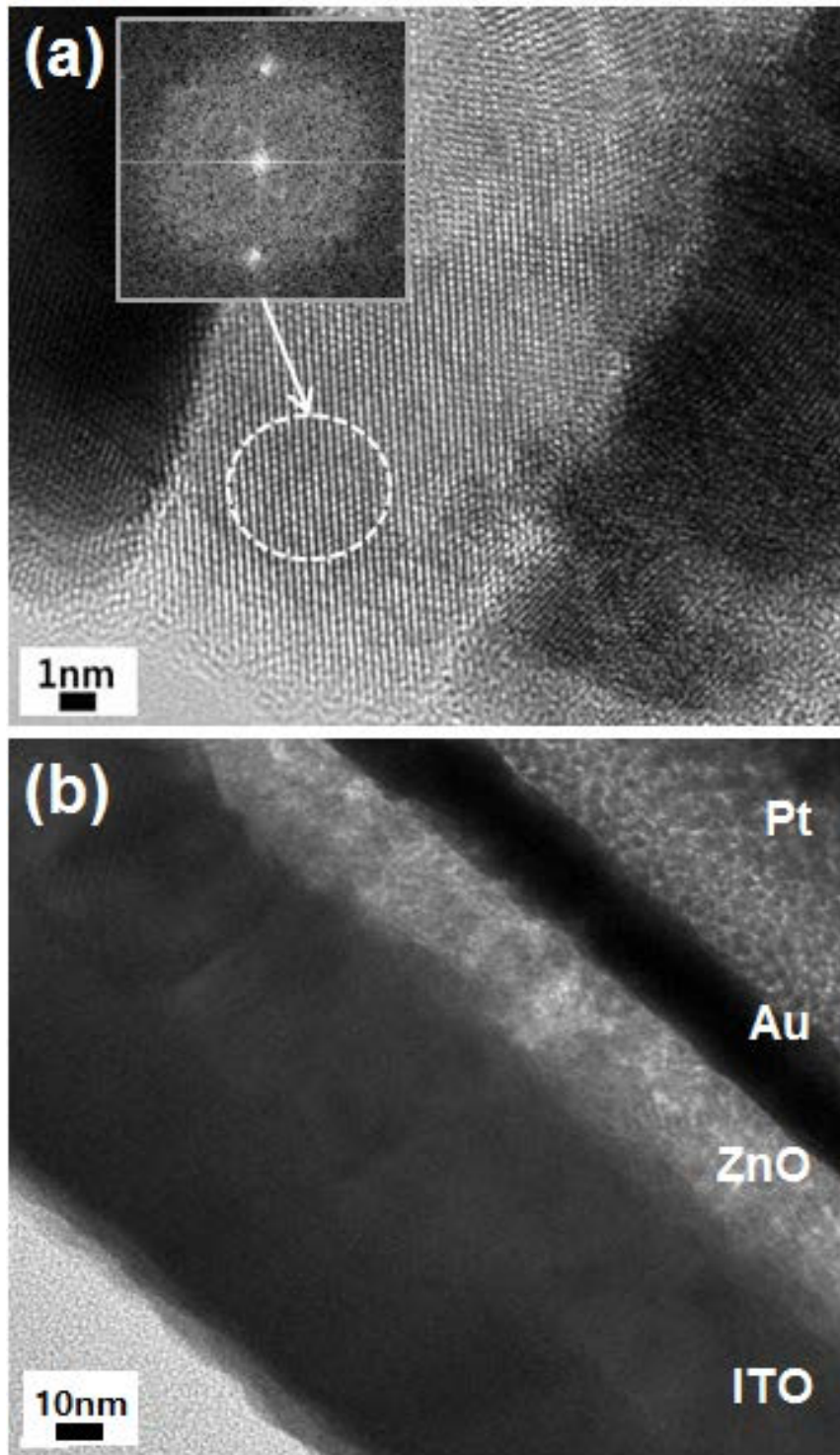


**Figure 3.7** The HRTEM image shows the deposition of the poly-crystalline ZnO nanostructure with the tendency for c-axis orientation with a (002) lattice plane.

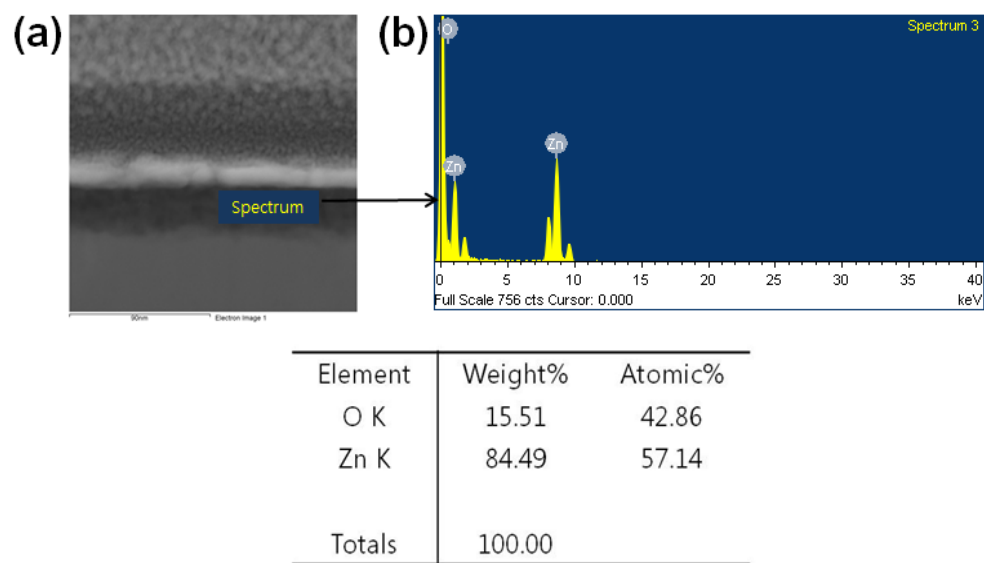


**Figure 3.8** EDX spectrum acquired from the layer of ZnO thin film in figure 3.7.

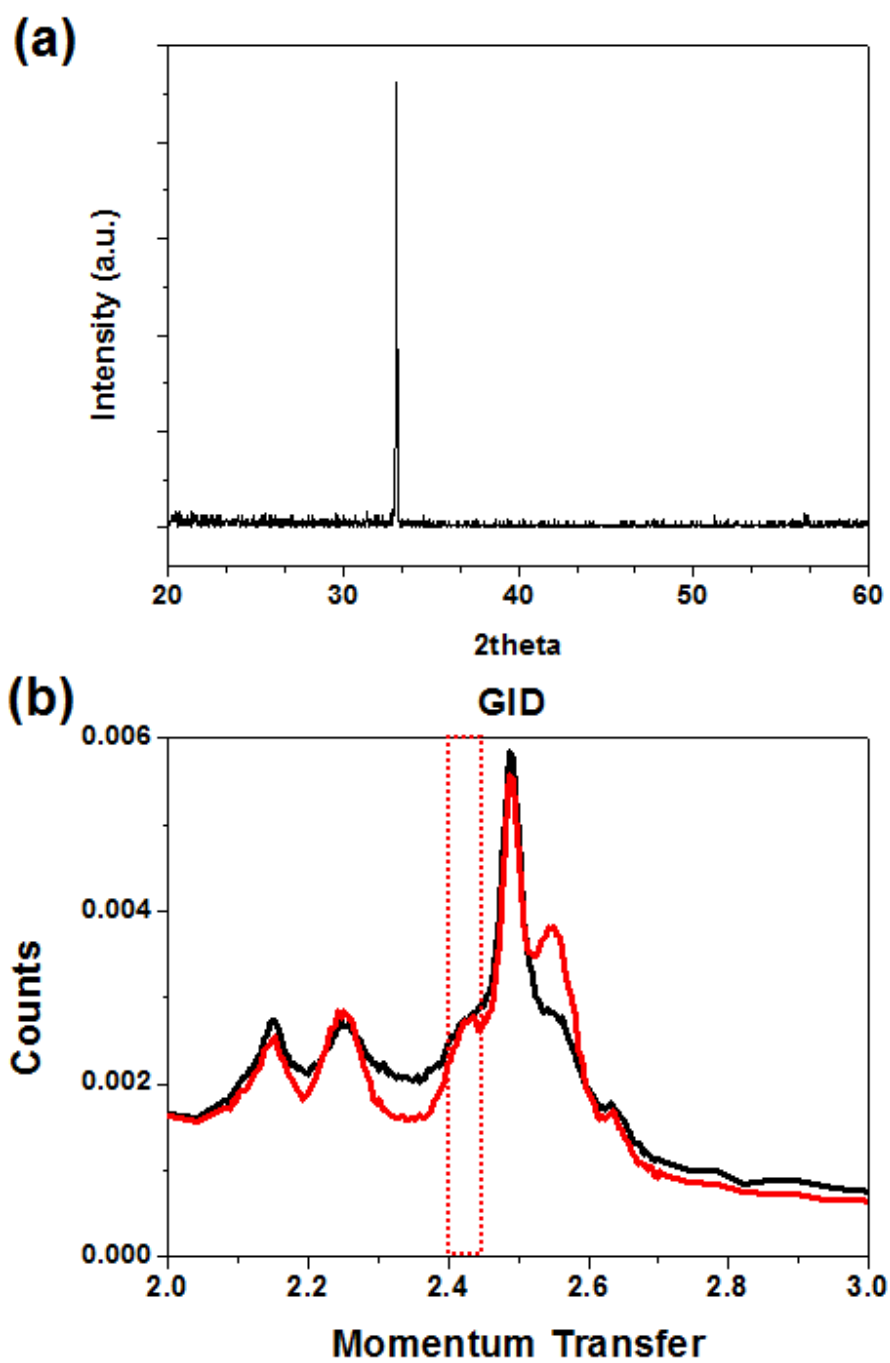


**Figure 3.9** (a) The XRD pattern of ZnO deposited on ITO layer with annealing temperature of 120 °C (b) The GIXRD analysis at the ZnO deposited ITO layer with annealing temperature of 90 °C and 150 °C (black = 90 °C, red= 150 °C).

### **3.3.2 Output performance of ZnO thin film piezoelectric nannogenerator**

The output voltage and current induced by periodic rolling motions were measured to characterize the piezoelectric effect of the all-solution-processed PENG. The rolling system of the PENG was firstly introduced to demonstrate a practical use as flexible nanounits such as mobile electronics, muscle-driven elements. One cycle of the rolling system went through three tighten-swap-release steps with a mechanical rolling machine (figure 3.10). The rolling rate was 150 mm/s and the rolling curvature radius was 2 cm. Persistent mechanical rolling was applied across the PENG using a rolling machine.

Three prominent peaks of output voltage and current in one cycle were observed from the measurement system as shown in figure 3.11. The initial tighten mode step induced small output voltage and current peaks of average 0.31 V and 30.5 nA/cm<sup>2</sup> with a slight decline at the end of this step. More rolling of the PENG was conducted in the swap mode while an interchanging of rolling direction followed to release the piezo-nanounit at the midpoint of this step. The most dominant output peaks of voltage and current density of average 0.66 V and 55.5 nA/cm<sup>2</sup> were recorded in this second process since the piezoelectric unit undergoes the highest rolling degree in its active area. The output pulses of voltage and current density for the release step were nearly identical at about 0.28 V and 26.6 nA/cm<sup>2</sup> with an alternative direction of the initial tighten step. A switching-polarity test of the PENG for forward- and reverse- connections (figure 3.13 (a) and (b)) with the current meter was performed under regular mechanical rolling to verify that the generated signals originated from the piezoelectric unit. The continuous AC mode

output signals of voltage and current peaks were detected from the measurement system. Each tighten-swap-release step traced the positive and negative pulse signals with different output power. The sequence of positive and negative output voltage and current pulse was in good accordance with the forward (black)- and reverse (red)-connections. Furthermore, almost identical average output signals from forward- and reverse- connections were observed for the each tighten-swap-release step, which noted that the output signals were generated by the PENG itself. The enhancement of negative output voltage generation for the forward-connection (positive output voltage in case of the reverse-connection) is attributed to the increased number of free carriers, which accumulated more into the Ag electrode due to the stronger Schottky contact formation after the deposition of the p-type and conducting polymers.<sup>15</sup>

PENG was also measured using periodic bending motions (figure 3.12). Precise alternative peaks were measured from one period of mechanical bending. A switching-polarity test was also carried out in the bending mode of the piezoelectric unit. The forward-connection of the PENG induced the initial appearance of positive current and voltage, while the negative current and voltage pulses were first examined when the PENG was connected reversely. The average output voltage and current density were 0.48 V and 38.0 nA/cm<sup>2</sup> for the both forward- and reverse- connections.

However, the p-type and conducting polymer, P3HT and PCBM were adopted from previous research to enhance the output power of our PENG. Since more free carriers flow through the Schottky barrier as a result of the interlaid p-type polymer blend for the enhancement of the piezoelectric potential, higher output power could be generated from the PENG. While the same p-type and conducting polymer was



utilized as-prepared in the previous report, another hole transport layer, PEDOT:PSS was used instead of the thermal evaporation of molybdenum oxide for the all-solution-process of the PENG. The solution-processed PEDOT:PSS layer functions as an efficient hole collecting layer at the interface of the P3HT/PCBM and the silver electrode. Moreover, since ZnO itself acts as a capacitance, the additional layers should be consider as capacitor. Thus, the other layers, ZnO-P3HT and also the P3HT-PCBM will reduce the overall capacitance because of connection in series. The experiemtal results of insertion of P3HT/PCBM and PEDOT:PSS is presented in figure 3.14. The output voltage of only consisted NG was about  $\sim 0.07$  V, otherwise, the output voltages of ZnO-P3HT/PCBM NG and ZnO-P3HG/PCBM-PEDOT:PSS were  $\sim 0.35$  and  $0.55$  V each. Therefore, the effect of p-n junction as well as the hole collecting layer make increment in output power of NG.

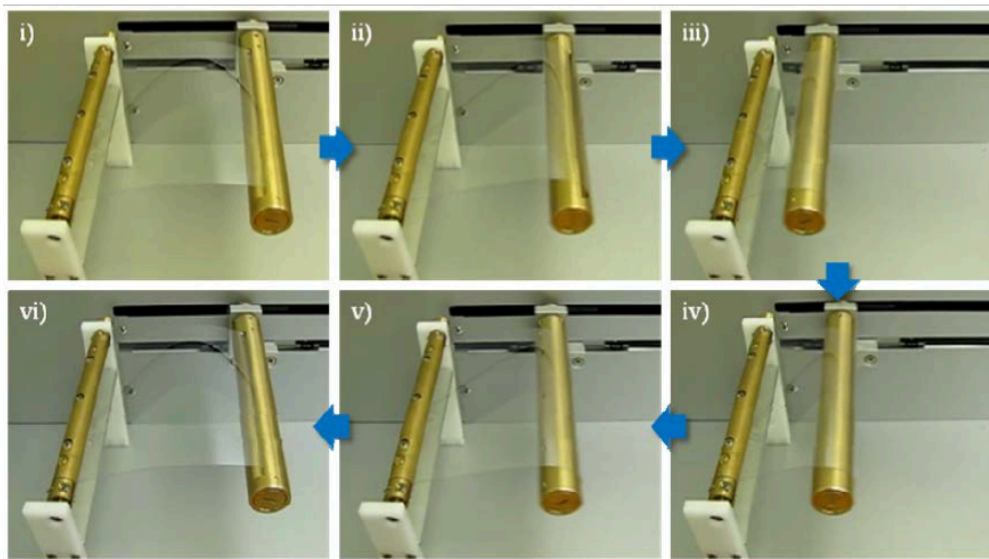


**Figure 3.10** One cycle of the rolling system went through three tighten (i-ii) – swap (iii-iv) – release (v-vi) steps with a mechanical rolling machine.

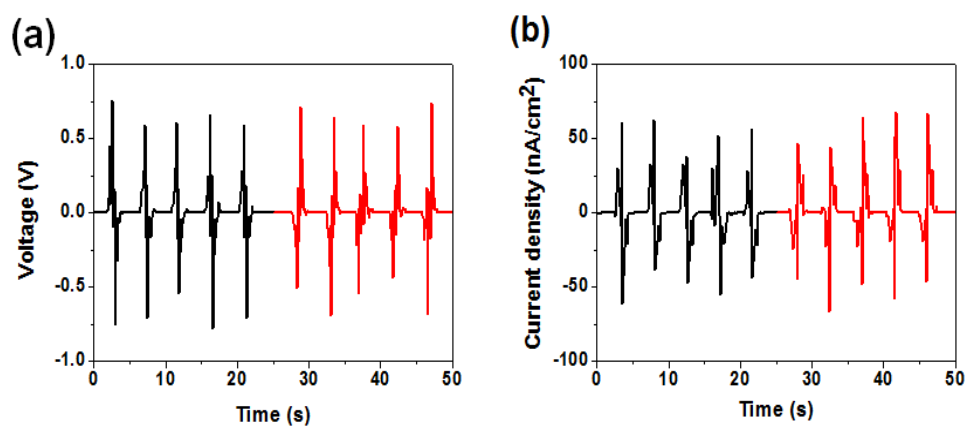


**Figure 3.11** Measured output voltage and current density of the all-solution-processed flexible thin film PENG from the mechanical rolling (a), (b).

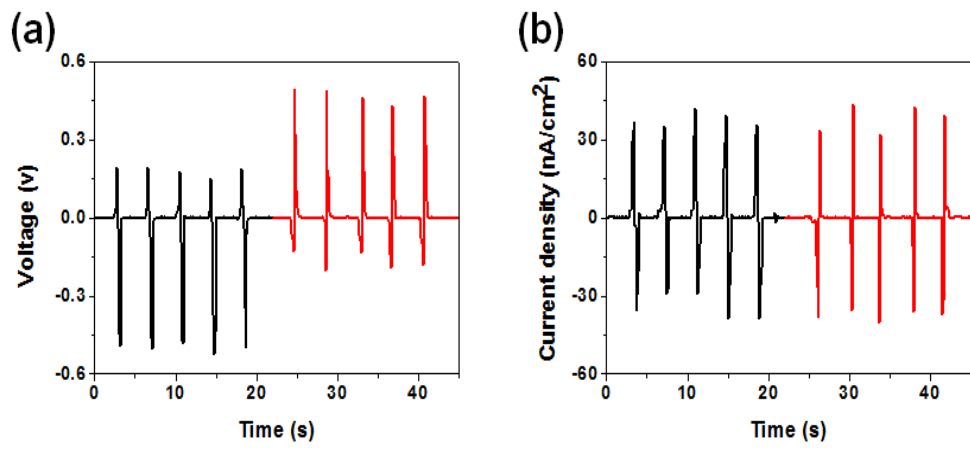


**Figure 3.12** Measured output voltage and current density of the all-solution-processed flexible thin film PENG from the mechanical bending motions (a), (b).

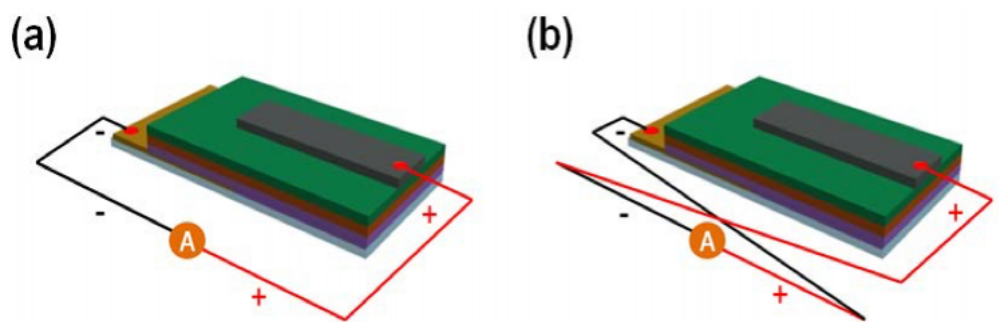


**Figure 3.13** The PENG was in (a) forward (black in graph) and (b) reverse (red in graph) connections with the measurement instrument for the switching- polarity tests.

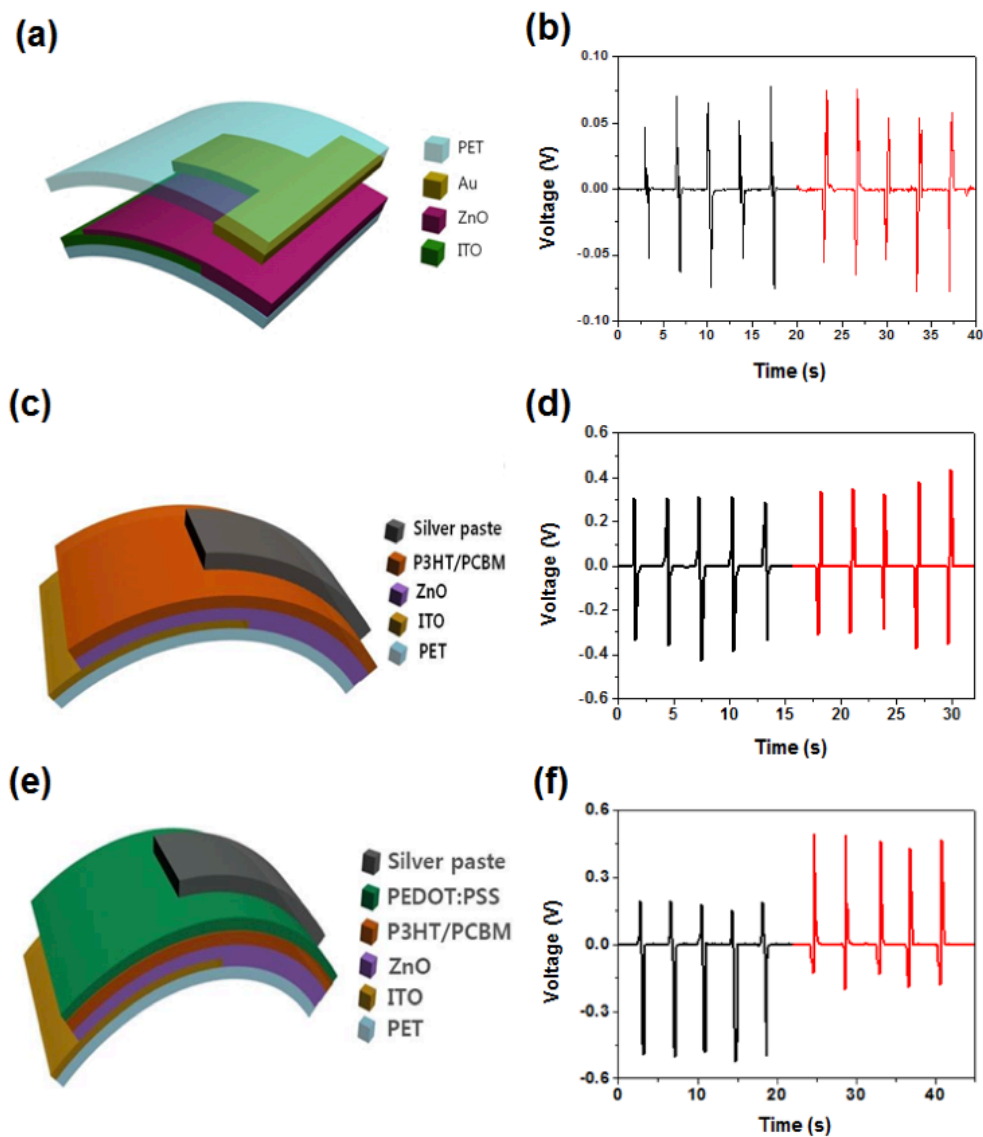


**Figure 3.14** (a) Schematic illustration of ZnO NG. (b) Measured output voltage from ZnO NG. (c) Schematic illustration of ZnO-P3HT/PCBM NG. (d) Measured output voltage from ZnO-P3HT/PCBM NG. (e) Schematic illustration of ZnO-P3HT/PCBM-PEDOT:PSS NG. (f) Measured output voltage from ZnO-P3HT/PCBM-PEDOT:PSS NG.

### 3.3.3 Operational mechanism

The mechanisms of the rolling and bending motions of our PENG were illustrated in figure 3.15 and 3.16. The p-type polymer P3HT was used to form a p-n junction diode with n-type piezo-semiconductor ZnO, otherwise the conductive polymer PCBM was mixed with the p-type polymer to organize so called 'blend' for better transportation of free carriers.<sup>15</sup> In addition, the hole transport layer, PEDOT-PSS was additionally deposited by spin-coating and finally a silver electrode was placed on top of the PENG for a formation of Schottky contact. The mechanical strain caused piezoelectric potential at the interface of the ZnO and adjacent materials. Positive piezoelectric potential at the interface between P3HT/ZnO and negative piezoelectric potential at the interface between ZnO/ITO were obtained in the first tighten mode of the mechanical rolling system (figure 3.10 i-ii). Negative piezoelectric potential at ITO/ZnO induced electrons to flow from the ITO electrode through the external circuit, while an output signal was generated in the opposite direction of the electron transport. The sudden changes in the first electrical peaks in figure 3.11 indicates transient flows of electrons that accumulated inside ZnO as shown in figure 3.15 i-ii. On the other hand, the static bending mode of the PENG can reduce the number of accumulated electrons at the interface between the silver and PEDOT:PSS since the sudden electron flow decreased. The swap mode was then carried out with a higher rolling degree of the piezoelectric nanounit (figure 3.15 ii-iv). The output voltage and current pulses enhanced as a result of the increased free electron flow through the Schottky barrier until the balance of the piezoelectric potential achieved equilibrium. Output power abruptly dropped to a lower level since the accumulated free electrons partly

flew through the external circuit because of the followed rolling motion in the opposite direction caused the lower strain of the PENG. Finally, the transported electrons flowed back to the bottom electrode to neutralize the current flow when the PENG was completely released from mechanical rolling (figure 3.15 iv-v)

The mechanism for the bending mode can be also explained in the same manner (figure 3.16). However, in the stretched state of the piezoelectric energy scavenger, only a small portion of the electrons compared to rolling system is piezo-potentially induced for output power generation. Therefore, our all-solution-processed flexible thin film PENG can generate more electrical output in a rolling mode than a bending mode since a bending motion induces only a portion of ZnO thin film compression while a rolling process is more likely to compress a broader range of ZnO thin film.



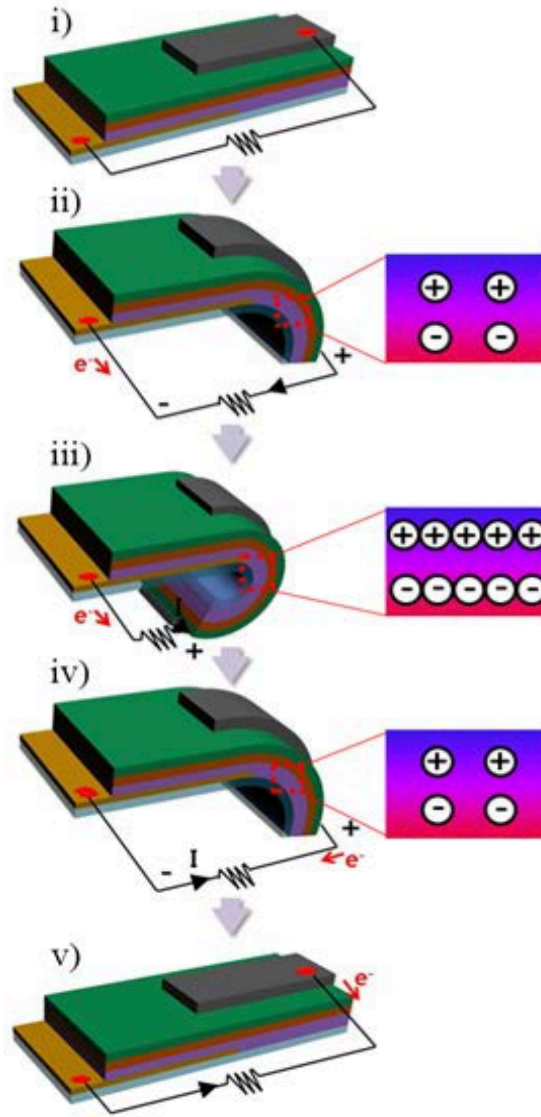


**Figure 3.15** Operational mechanism of the PENG. Rolling motion of the PENG through the three tighten-swap-release steps. The as-fabricated thin film based PENG with (i) no force applied. (i-ii) Tighten step of the PENG through the rolling motion undergoes the electron -flow from the ITO electrode through the external circuit. (ii-iv) The swap step of the PENG through the rolling motion induces more electron-flow through the Schottky barrier. (iv-v) The release step of the PENG with electron-flow back to the ITO electrode to neutralize the current flow.

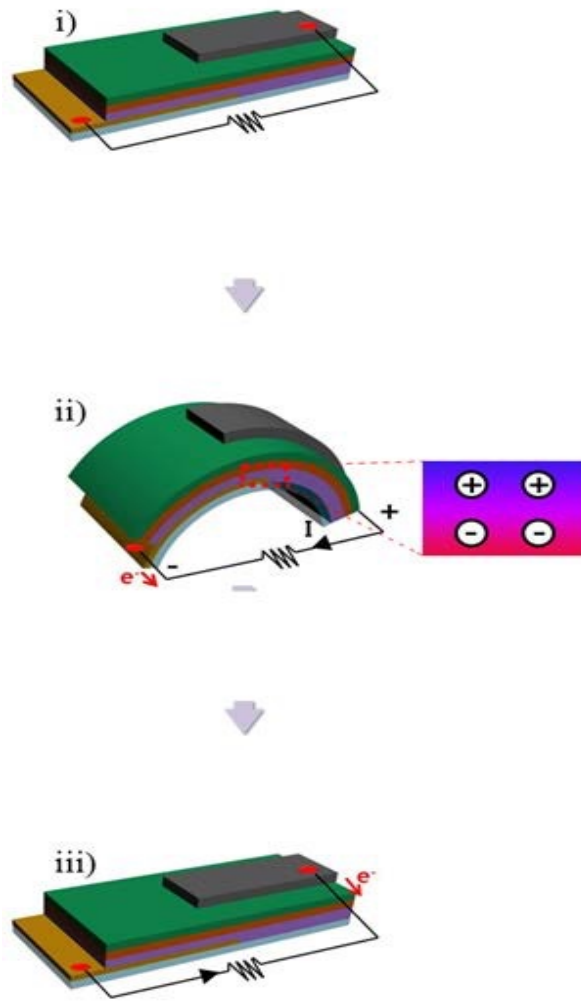


**Figure 3.16** Operational mechanism of the PENG. (b) Bending motion of the PENG with (i) static, (ii) bending and (iii) release steps. A small portion of electron-flow was induced from the bending step compared to swap step of the rolling motion.

### **3.3.4 Stability and muscle-driven test**

The long term-stability test for PENG operation was performed for 2000 seconds (about 666times) (Figure 3.17 (a) and (b)). The comparably stable output power demonstrates the mechanical stability of the flexible thin films fabricated by the all-solution process. The insets of figure 3.17 show the continuous peaks of output voltage and current density from the long-term endurance test.

The output voltage pulse was also detected from the muscle stretching of the human body (figure 3.18). Periodic arm-stretching stimulated the nanounit to generate output power of about 0.28V. It is anticipated to be feasible and practical for the embedded muscle or clothes scavengers or for the shoe-sole power generator to harvest low frequency energy.

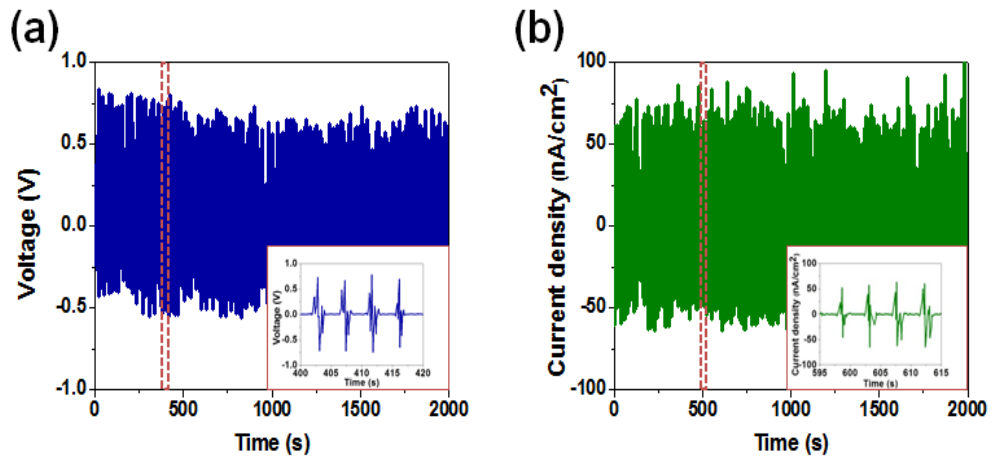


**Figure 3.17.** Long-term stability test to confirm the mechanical endurance of the PENG. (a) The output voltage and (b) current density for the period of 2000s (about 666times) operation of the PENG.

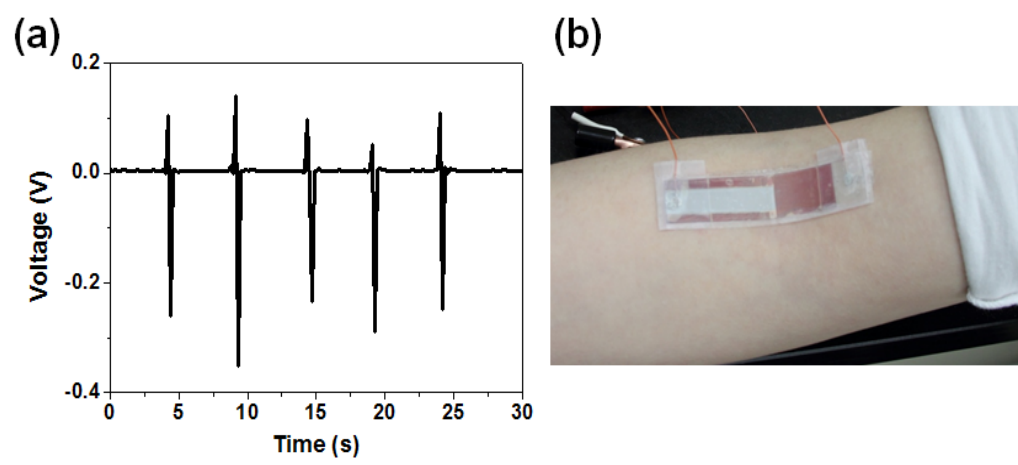


**Figure 3.18** (a) Measured output voltage from (b) the muscle-stretching of the PENG.

### 3.4 References

- [1] R. Yang, Y. Qin, C. Li, G. Zhu, X. D. Wang, Nano Lett. **2009**, 9, 1201.
- [2] X. Wang, J. Song, J. Liu, Z. L. Wang, Science **2007**, 316, 102.
- [3] S. N. Cha, J. -S. Seo, S. M. Kim, H. J. Kim, Y. J. Park, S. -W. Kim, J. M. Kim, Adv. Mat. **2010**, 22, 4726.
- [4] Z. Li, Z. L. Wang, Adv. Mater. **2011**, 23, 84.
- [5] Z. Li, G. Zhu, R. Yang, A. C. Wang, Z. L. Wang, Adv. Mater. **2010**, 22, 2534.
- [6] Z. L. Wang, R. Yang, J. Zhou, Y. Qin, C. Xu, Y. Hu, S. Xu, Mater. Sci. Eng. R **2010**, 70, 320.
- [7] K. -I. Park, S. Xu, Y. Liu, G. -T Hwang, S. -J. L. Kang, Z. L. Wang, K. J. Lee, Nano Lett. **2010**, 10, 4939.
- [8] (a) Y. Qi, N. T. Jafferis, K. Lyons, Jr., C. M. Lee, H. Ahmad, M. C. McAlphine, Nano Lett. **2010**, 10, 524.  
(b) Y. Qi, J. Kim, T. D. Nguyen, B. Lisko, P. K. Purohit, M. C. McAlphine, Nano Lett. **2011**, 11, 1331.
- [9] Z. L. Wang, J. H. Song, Science **2006**, 312, 242.
- [10] D. Choi, K. Y. Lee, M. -J. Jin, S. -G. Ihn, S. Yun, X. Bulliard, W. Choi, S. Y. Lee, S. -W. Kim, J. -Y. Choi, J. M. Kim, Z. L. Wang, Energy Environ. Sci. **2011**, 4, 4607.
- [11] D. Choi, K. Y. Lee, K. H. Lee, E. S. Kim, T. S. Kim, S. Y. Lee, S. -W. Kim, J. -Y. Choi, J. M. Kim, Nanotechnology **2010**, 21, 405503.
- [12] M. Yamada, M. Matsumura, Y. Maeda, Thin Solid Film. **2011**, 519, 3352
- [13] S. Bae, H. Kim, Y. Lee, X. Xu, J. -S. Park, Y. Zheng, J. Balakrishnan, T. Lei, H. R. Kim, Y. I. Song, Y. -J. Kim, K. S. Kim, B. Özilmaz, J. -H. Ahn, B. H. Hong

- & S. Iijima, *Nature Nanotech.* **2010**, 5, 574.
- [14] M. -Y. Choi, D. Choi, M. -J. Jin, I. Kim, S.-H. Kim, J. -Y. Choi, S. Y. Lee, J. M. Kim, S. -W. Kim, *Adv Mat.* **2009**, 21, 2185.
- [15] K. Y. Lee, B. Kumar, J. -S. Seo, K. -H. Kim, J. I. Sohn, S. N. Cha, D. Choi, Z. L. Wang, S. -W. Kim, *Nano lett.* **2012**, 12, 1959.
- [16] S. T. Meyers, J. T. Anderson, C. M. Hung, J. Thomson, J. F. Wager, D. A. Keszler, *J. Am. Chem. Soc.* **2008**, 130, 17603.
- [17] K. Kim, S. Park, J.-B. Seon, K.-H. Lim, K. Char, K. Shin and Y. S. Kim, *Adv. Func. Mater.* **2011**, 21, 3546.
- [18] H. -K. Park, K. Y. Lee, J. -S. Seo, J. -A. Jeong, H. -K. Kim, D. Choi, S. -W. Kim, *Adv. Funct. Mat.* **2011**, 21, 1187.
- [19] K. Kim, S. Park, J.-B. Seon, K.-H. Lim, K. Char, K. Shin and Y. S. Kim, *Adv. Func. Mater.* **2011**, 21, 3546.

# Chapter 4. ZnO nanorod piezoelectric bending motion sensor

## 4.1 Introduction

Development of flexible and portable bending motion sensor has recently been flourished for diverse applications including human artificial skin,<sup>1</sup> wearable electronics,<sup>2,3</sup> and biomimetic robot system.<sup>4</sup> Among diverse transduction mechanisms for bending sensors such as resistivity,<sup>5-10</sup> capacitance change,<sup>11</sup> optical power,<sup>12,13</sup> and piezoelectric output potential,<sup>14,15</sup> piezoelectric potential change is desirable for the self-powered active system as well as the benefits in portability, environmentally compatibility, and persistent utilization. Moreover, oxide based wurzite piezoelectric materials have advantages in flexibility, low cost, and availability for wearable manufacturing.

Sensing of bending curvature and speed in a simultaneous manner enables an accurate tracking of bending motions across the piezoelectric sensor. However, most researches have simply been focused on the change of piezoelectric outputs as a function of bending curvatures.<sup>14,15</sup> For instance, piezoelectric sensor demonstrated by Nour *et al.*, which has double-sided ZnO NW configuration, simply presented different output voltages according to only bending curvature.<sup>15</sup> However, the generated piezoelectric outputs affected by bending speed as well as the bending curvature.<sup>16</sup> More precisely, the piezoelectric bending motion sensor during the same bending curvature operation with different bending speed will have apparent different signal values. Therefore, two factors, bending curvature and speed, need to be considered together in one bending motion for the piezoelectric sensor as experimental conditions. Through this step, bending



motions across the piezoelectric sensor could be accurately speculated with awareness of the bending curvature and speed.

Herein, the wearable piezoelectric bending motion sensor was demonstrated with simultaneous analysis on bending curvature and speed. To recognize the bending motions, the output voltages and voltage area were presented according to the bending curvature and speed and the correlation between the voltage area and these two factors was analyzed. For bendability, a PDMS sandwiched ZnO NR layer was used as an active layer as well as the hybrid electrode of Ag NW-SWCNT was utilized. While large majority of other researches on piezoelectric sensors or NGs adopted metals as conducting electrodes, this study utilized a flexible hybrid electrode of Ag NW and SWCNT for assurance of bendability without any mechanical cracks and maintenance of electrical conductivity during the prolonged operation of sensing units. From the element structures, real-flexibility of the piezoelectric device was actualized for practical bending motion sensing system.

## 4.2 Experimental

Figure 4.1 shows the experimental procedure of the piezoelectric bending motion sensor. Ultraviolet ozone (UVO) treatment of PET film was conducted for the formation of hydrophilic surface prior to the electrode depositions (figure 4.1 (a)). Then, the Ag NW-SWCNT solution with a certain weight ratio was spray-coated onto the PET film at 100 °C (figure 4.1 (b)). Before rubbing ZnO NRs, PDMS solution was spin-coated and cured at 85 °C, as shown in figure 4.1 (c). Using a brush, bi-axially grown ZnO NRs were randomly spread out onto PDMS layer through rubbing process until a monolayer of ZnO NRs were obtained (figure 4.1

(d)). Another PDMS layer was then covered the monolayer, subsequently followed by the UVO treatment after the PDMS curing (figure 4.1 (e)). Finally, the spray-coating of Ag NW-SWCNT was carried out for top electrodes in the same weight ratio of the bottom one and Cu wire was connected to the both electrodes for electric measurement (figure 4.1 (f)).

#### **4.2.1 Synthesis of bi-axially grown ZnO nanorods**

ZnO NRs were synthesized by a hydrothermal method. Typical chemical reagents for a hydrothermal growth of ZnO NRs were used; Zinc nitrate hexahydrate ( $\text{Zn}(\text{NO}_3)_2 \cdot 6\text{H}_2\text{O}$ ) [Sigma Aldrich,  $\geq 99.0\%$ ] and HMTA ( $\text{C}_6\text{H}_{12}\text{N}_4$ ) [Sigma Aldrich,  $\geq 99.0\%$ ]. 0.42 g of zinc nitrate hexahydrate and 0.21 g of HMTA were dissolved in 100 ml DI water each and vigorously stirred using a vortex. The hydrothermal method of ZnO NRs was conducted in three steps; heating, injecting, and filtering. Firstly, the HMTA solution in a 250 ml round flask was heated into  $85\text{ }^\circ\text{C}$  using a heating mantle with vigorous stirring at 400 rpm for 10 min. Secondly, two separately divided zinc nitrate solutions were injected simultaneously into the hot HMTA solution via a syringe pump at an injection rate of 2 ml/min for 25 min. Finally, the milky precipitate of ZnO solution was percolated with ethanol via vacuum filtration through  $0.2\text{ }\mu\text{m}$  pore size of a membrane filter [Macherey-Nagel, Porafil-CA] and dried at  $80\text{ }^\circ\text{C}$  for hours to obtain off-white powders of ZnO NRs.

#### **4.2.2 Fabrication of Ag NW-SWCNT electrodes**

For flexible and ultrathin film, hybrid electrodes of silver nanowires and single-

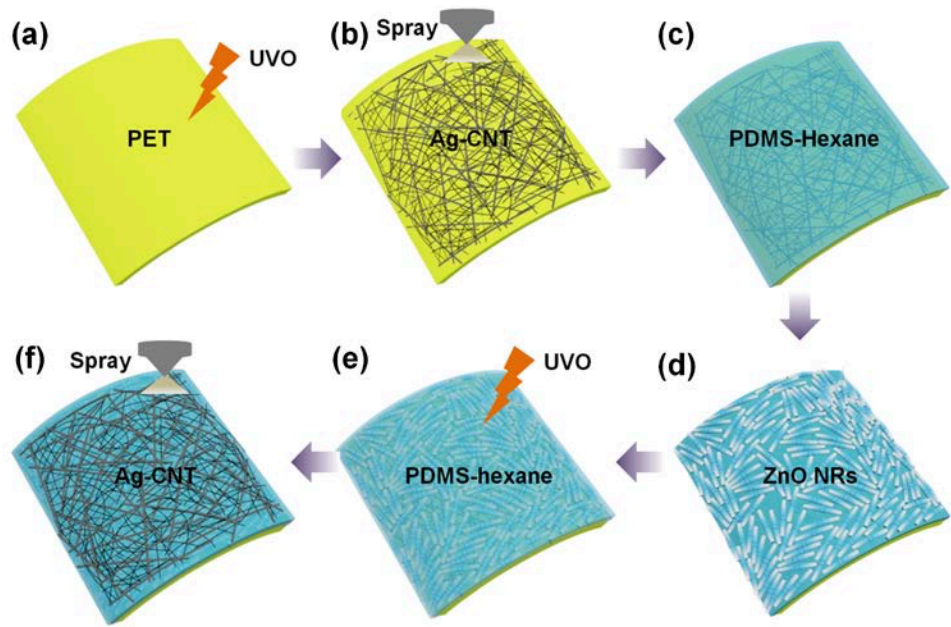


**Figure 4.1** A schematic procedure of the bi-axially grown ZnO NRs based piezoelectric bending motion sensor. (a) UVO treatment of PET substrate. (b) Spray-coating of Ag NW-SWCNT onto PET substrate. (c) Spin-coating of PDMS-hexane solution and post-annealing at 85 °C for 30 min. (d) Rubbing ZnO NR using a brush onto the PDMS layer. (e) The spin-coating and annealing process of PDMS-hexane. (f) The spray-coating of Ag NW-SWCNT electrode.

wall carbon nanotubes were adopted through preliminary experiments. The spray-coating of Ag NW-SWCNT was attempted with several experimental conditions to find out optimal component value of hybridized Ag NWs and SWCNT. Firstly, the 1% Ag NWs solution [Nanopyxis, 1wt% in distilled water] in distilled water was diluted with deionized water to a concentration of 5wt% (total concentration in 0.05% in water solution) by vigorous sonication. The SWCNT [Nano Solution Co. Ltd. 1.3 wt% in distilled water stabilized by sodium dodecyl sulfonate (SDS) surfactants] was used as received without any further purification. 9, 8 and 7 g of 0.05wt% Ag NWs and 1, 2 and 3g of 1.3wt% SWCNT were mixed respectively via vigorous sonication to find out adequate weight ratio of Ag NWs and SWCNT for formation of flexible and conductive hybrid electrode.

Prior to the spray-coating, an UVO treatment onto a PET film was conducted for 30 min to form hydrophilic surfaces. The spray-coating was set in a hand-made cage with spray nozzle on the top connected to air and syringe pump for continuous supply of Ag NW-SWCNT source with continuous air flow. The UVO treated PET film was then placed in bottom with distance 30 cm away from the spray nozzle and also onto a hot plate. The 9:1, 8:2, 7:3 weight ratio of 0.05wt% Ag NW:1.3wt% SWCNT solutions each was spray-coated onto the surface of UVO treated PET film with continuous feeding of the Ag NW-SWCNT sources through a syringe pump. The spray-coating was conducted at an injection rate of 0.2ml/min with an air pressure of 2 bar for 5min and the hot plate was set at temperature of 100°C for evaporation of the water solvent. The spray-coated PET substrate finally washed with DI water for a removal of the SDS surfactant.

### **4.2.3 Fabrications of piezoelectric bending motion sensor**

The piezoelectric bending motion sensors were constituted in simple metal : insulator : metal (MIM) structures of Ag NW-SWCNT : ZnO NRs : Ag NWs-SWCNT. UVO treatments of plastic substrates were essentially conducted for the formation of hydrophilic surface prior to the electrode depositions. After the deposition of the Ag NWs-SWCNT bottom electrodes followed by the above experimental procedure, PDMS (PDMS : hexane mixture in 5:5 weight ratio) layer was spin-coated at 3000 rpm for 30 s onto the electrodes, annealed at 85 °C for 30 min. The ZnO NRs were then rubbed using a brush and nitrogen blowing was applied for neat and tidy layer of ZnO NRs. Another layer of PDMS is covered the ZnO NRs under the same spin-coating conditions above. Also, the UVO treatment of the substrate was required before the spray-coating of the electrode. Finally, the top electrodes were formulated by spray-coating and Cu wire connection with spray-coated Ag NW-SWCNT electrodes was conducted for electric measurement.

### **4.2.4 Characterizations**

The crystallinity and morphology of ZnO NRs were investigated by an XRD [Bruker New D8 Advance] and a FE-SEM [Hitachi S-4800], respectively. For surface structure and compositional information, X-ray photoelectron spectrometry (XPS) was conducted. In addition, thermal stability and decomposition temperature were observed by (TGA-DSC). Moreover, the morphology and electrical conductivity of Ag NW-SWCNT hybrid electrodes were observed by an optical microscope (OM) [Olympus U-CMAD3], a HRSTEM [JEM-2100F] and four-point probe resistivity measurement system [sourcimeter: Keithley 2400 and multimeter:

Agilent 34410A]. Finally, the output voltages of the piezoelectric bending motion sensors were measured using an oscilloscope [Tektronix MDO3024].

## 4.3 Results and discussion

### 4.3.1 Characteristics of bi-axially grown ZnO nanorods

The ZnO NRs were grown by colloidal phase synthesis, which makes the ZnO NRs configuration in bi-axial structure. In the colloidal phase synthesis, the Zn seed were floated on the water making ZnO NRs in bi-axial configuration.<sup>1</sup> Generally, ZnO NRs for piezoelectricity are grown on a seed layer, which is usually formed by spin-casting or sputtering system of seed solution. Contrary to the unidirectionally grown ZnO NRs by substrate-based growth method, this made the ZnO NRs in bi-axial configuration, which makes the piezoelectric material favorable to the bending system. The bi-axial ZnO NRs were uniformly grown from a hydrothermal synthesis as shown in FE-SEM image of figure 4.2 (a). The average diameter and length were 373.5 nm and 3.52  $\mu\text{m}$  each. The hydrothermally grown ZnO NR powder was poured onto PDMS layer and rubbed using a soft paint brush to be spread out until a thin monolayer of ZnO NRs was completely filled out the bare PDMS layer as shown in figure 4.2 (c). The dense and continuous monolayer of bi-axially grown ZnO NRs was formed as a result of the rubbing process as shown in figure 4.2 (b). Since the rubbing of ZnO NRs using a soft paint brush took only small forces, the ZnO NRs could be spread onto PDMS layer without any mechanical cracks. The main mechanism for the attachment of ZnO NRs onto PDMS is the Van der Waals forces, which is the intermolecular forces between the molecules and surfaces.<sup>18</sup> The rubbing direction of ZnO NRs onto the PDMS was random for identical output performance of piezoelectric bending motion sensor for any direction of bending.

In addition, the bi-axially grown ZnO NRs fabricated by a colloidal phase

synthesis is remarkably favorable for bending motion operation as following the finite element method (figure 4.3). The bi-axially grown ZnO NRs were symmetrically bent with crystal center in the middle. As a result, the ZnO NR could be symmetrically bent with c-axis growth, which was parallel to the center-axis according to the simulation.<sup>18</sup> Piezoelectric potential distribution was calculated using the finite element method in our previous research. According to the simulation, mechanical load was applied along the y-direction at the line boundary of the NR. Accordingly, the positively polarized upper region and negatively polarized lower region were observed, which was substantial result for generation of electric charges at both electrodes. Therefore, the bi-axially grown c-axis oriented ZnO NRs were eligible for lateral bending of piezoelectric sensor comprehensively. However, the generally used uni-axially grown ZnO NR was piezopotentially null under bending motion as a result of the finite element method. Therefore, the bilaterally oriented c-axis ZnO NR we used is superior in harsh bending condition with flexibility and notability in piezoelectric potential generation.

To characterize the crystalline phase of ZnO NRs, powder XRD was carried out as shown in figure 4.4. The major XRD patterns were indexed in (100), (002), (101), (102), (110), (103), (201), indicating the Wurtzite structure of crystalline ZnO.<sup>19</sup> Especially, the high intensity of (101) diffraction peak indicates increased growth along the  $\langle 2\bar{1}\bar{1}0 \rangle$ , but there was still a tendency for growth direction along the  $\langle 0001 \rangle$  according to the (002) peak.<sup>2</sup> Thus, the XRD pattern indicates that the growth direction of the ZnO NRs was along c-axis orientation.

To analyze the surface structure and compositional information, XPS was conducted as shown in figure 4.5. The high-resolution Zn-2p<sub>3/2</sub> and Zn-2p<sub>1/2</sub>



photoelectron spectra indicated the two peaks at 1020.5 eV ( $2p_{3/2}$ ) and 1043.8 eV ( $2p_{1/2}$ ), which prove the existence of zinc in  $Zn^{2+}$  form. The XPS spectra of O-1s were fitted in three peaks. The first peak at lower binding energy of 529.8 eV indicated the O atom in ZnO matrix. The second peak at 531.3 eV is attributed to the strongly anchored hydroxyl groups (Zn-OH) caused by oxygen deficiency. Finally, the third peak was at 531.6 eV is ascribed to the chemisorbed oxygen or OH species on the surface of the ZnO.

Finally, thermal stability and decomposition temperature of ZnO NRs were characterized by TGA-DSC curves as shown in figure 4.6. The TGA-DSC curves was measured in nitrogen atmosphere with a heating ratio of  $5\text{ }^{\circ}\text{C min}^{-1}$ . Endothermic reaction with only 2.88% weight loss of ZnO NRs was observed as a result of TGA-DSC. Thus, as-synthesized ZnO NRs are superior in stability and comparable to previous research, which used a template-free synthesis method for growth of ZnO NRs.<sup>1</sup>

Therefore, in the view of mechanical and piezoelectric properties, the bi-axially grown ZnO NRs we used are favorable for piezoelectric operation in bending system compared to other brittle perovskite materials. Generally, to use the perovskite materials for piezoelectric operation, patterning process for acquisition of flexibility and high temperature treatment for crystalline phase for piezoelectric properties are required. Therefore, the use of Wurzite nanostructure such as ZnO NR is simple and allowed the piezoelectric sensing operation under harsh bending condition because of its flexible structure. The ZnO NR exhibits high elasticity and resistance to mechanical fatigue.

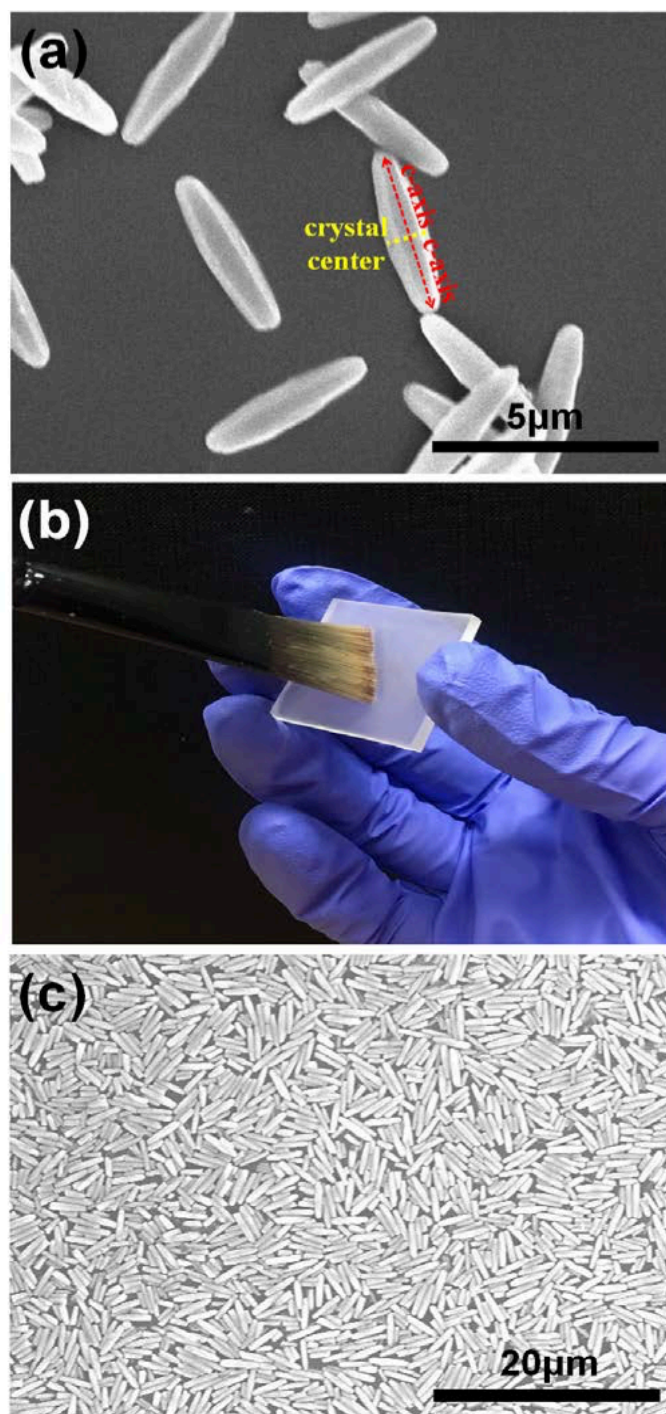


**Figure 4.2** (a) FE-SEM image of bi-axially grown ZnO NRs. (b) Photograph of rubbing process for ZnO deposition onto PDMS layer using a soft paint brush. (c) Randomly rubbed bi-axially grown ZnO NRs onto PDMS layer.

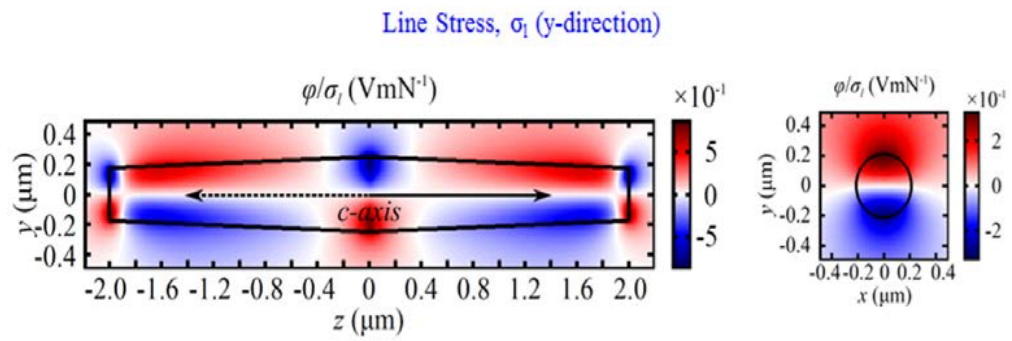


**Figure 4.3** Piezoelectric potential simulation results of bi-axially grown ZnO NR  
(Reference: *Energy Environ. Sci.*, 2014, **7**, 3994).

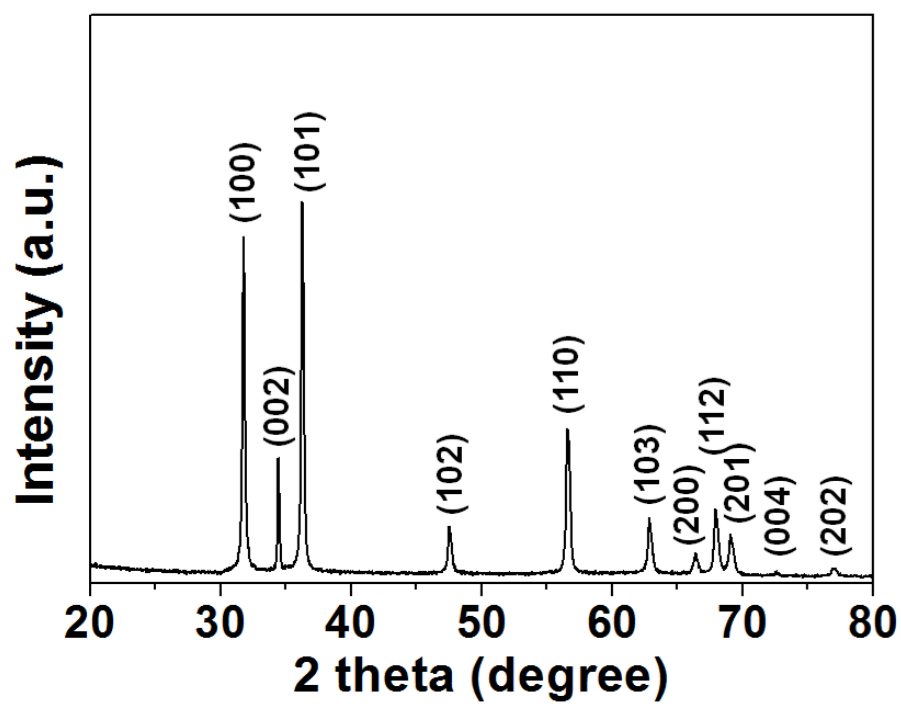


**Figure 4.4** Powder XRD pattern of bi-axially grown ZnO NRs.

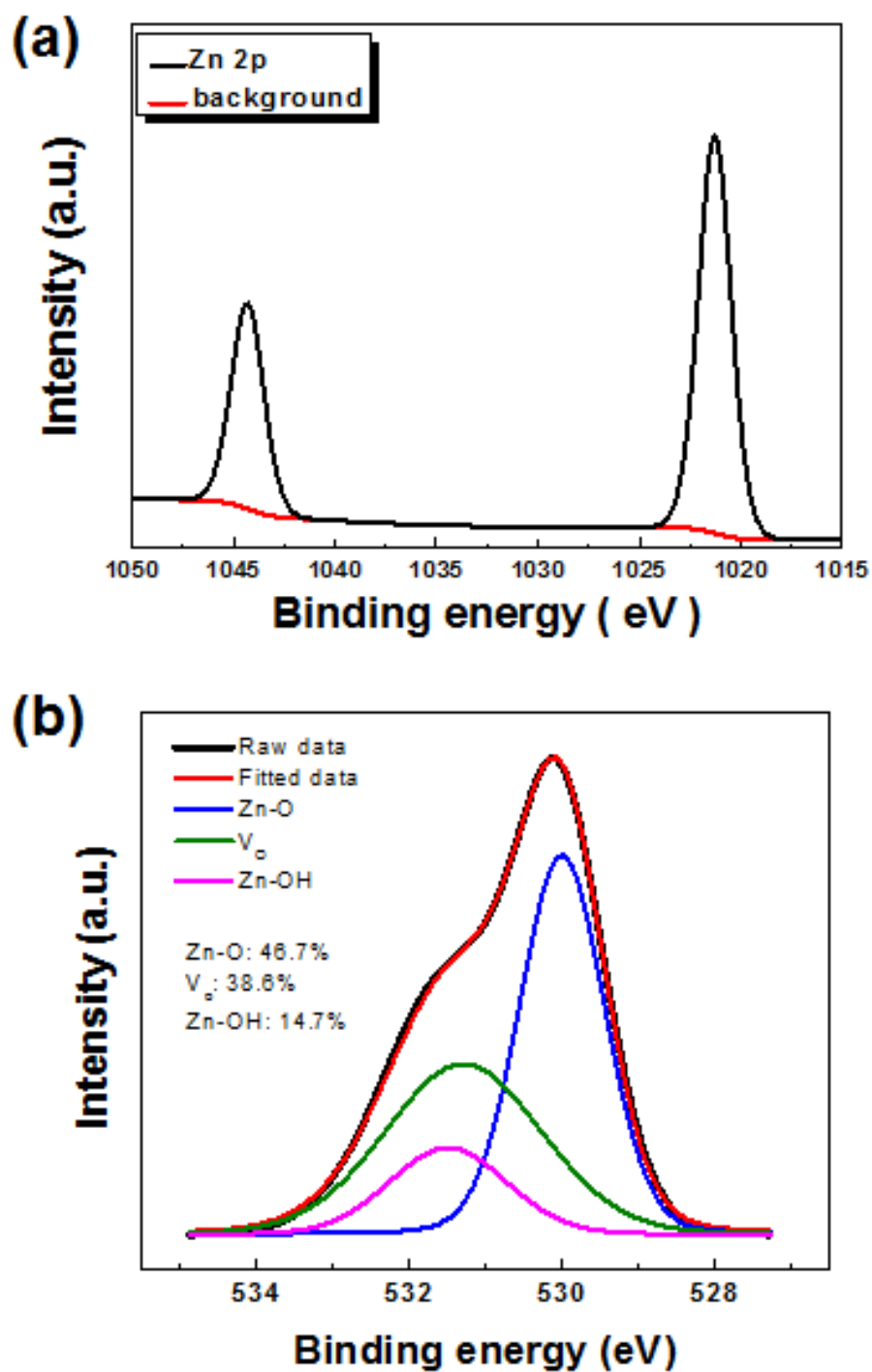


Figure 4.5 XPS spectra of (a) Zn-2p and (b) O-1s peaks.

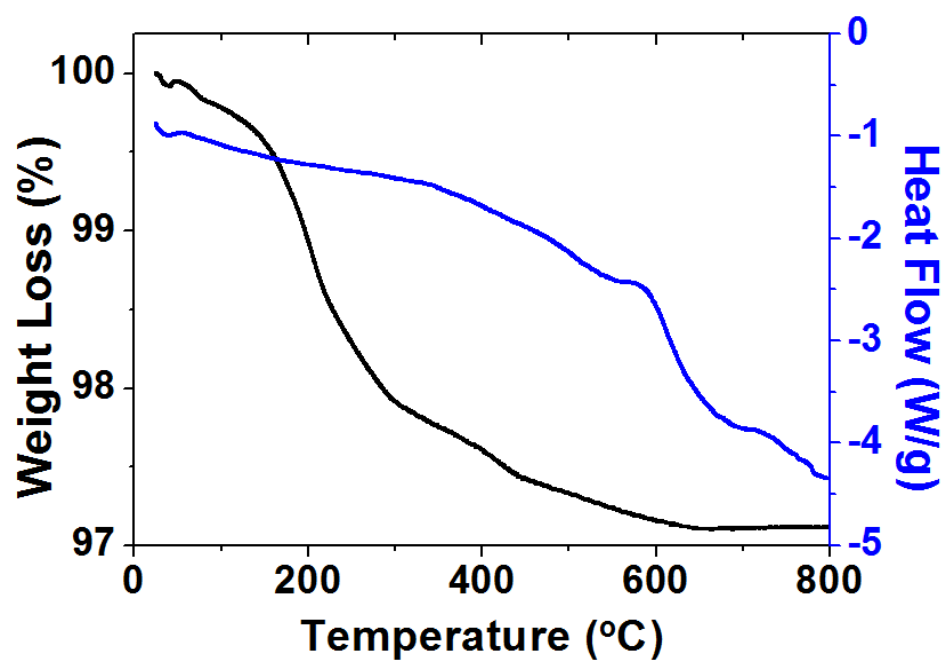


Figure 4.6 TGA-DSC curves of the ZnO NRs.

### 4.3.2 Characteristics of hybrid Ag NW-SWCNT

The spray-coating of Ag NW-SWCNT was attempted with several experimental conditions to find out optimal component value of hybridized Ag NWs and SWCNT. 9, 8, and 7 g of 0.05 wt% Ag NWs in DI water and 1, 2, and 3 g of 1.3 wt% SWCNT also in DI water were mixed respectively via vigorous sonication and prepared for spray-coating. With customized spray coating setup as shown in figure 4.7, the Ag NW-SWCNT composite film was spray-coated without agglomeration. The Ag NWs-SWCNT electrodes were spray-coated with feeding of the Ag NWs-SWCNT sources through a syringe pump with a constant air injection for the formation of uniform hybrid electrodes. The hybrid solution then spray-coated via a syringe pump at an injection rate of 0.2 ml/min with an air pressure of 2 bar onto the UVO-treated PET films for 5 min, annealing at 100 °C for evaporation of the water solvent.

The spray-coated hybridized Ag NW-SWCNT electrodes were tested before and after 10 times mechanical bending through OM observation. As shown in figure 4.8 and figure 4.9, the mechanical cracks were observed after the bending of electrodes in both case of bottom and top electrodes in weight ratio of 9:1 and 8:2 (g:g) of 0.05 wt% Ag NW : 1.3 wt% SWCNT. This is because of the unstable inter-connection between Ag NWs and also the poor adhesion of Ag NWs onto the PET due to the lack of SWCNT content.<sup>20</sup> Otherwise, the continuous morphology of Ag NW-SWCNT was observed in case of 7:3 (g:g), indicating the effect of SWCNT content in the hybridized electrode. Accordingly, this indicates that the SWCNT functioned as an inter-connector between the Ag NWs for continuous morphology. Moreover, the SWCNT functioned also as an adhesion agent for

better cohesion of Ag NWs to the PET substrate. The spray-coated Ag NW-SWCNT hybrid electrode onto PET substrate with optimal component ratio of 7:3 (0.05 wt% Ag NW : 1.3 wt% SWCNT) was observed through FE-SEM as shown in figure 4.10. The Ag NW-SWCNT composite film was uniformly coated without agglomeration. The Ag NW-SWCNT electrode was also observed by HRSTEM for better observation (figure 4.11). The Ag NWs were dark color column and the ash-colored SWCNT was entangled in gap of the Ag NWs, filling up the vacant room between the Ag NWs and making an inter-connection of Ag NWs. Figure 4.11 (b) shows the central region image of Ag NW-SWCNT, indicating the crystalline lattice of Ag NWs and electron diffraction pattern of individual Ag NWs in figure 4.11 (c) revealed the pentagonal rotational periodicity.

The examination of sheet resistance in figure 4.12 was conducted to measure the electrical conductivity of Ag NW-SWCNT electrodes at an optimized weight ratio (7:3 of 0.05 wt% Ag NW : 1.3 wt% SWCNT) according to the different bending curvature using the four-point probe measurement method (figure 4.12 (a)). To measure the sheet resistance of bent electrode, a multimeter was used during the bending of the piezoelectric bending motion sensors. This is because of the difficulty in use of four point probe during the bending of the piezoelectric elements. Finally, the multiply value of the ratio of ohms between the bent and no bending value (no unit) to the sheet resistance ( $\Omega/\square$ ) is in unit of  $\Omega/\square$ . It is notable that the value of sheet resistance is considerably consistent according to the applied bending curvature with average values of 15.13 and 18.14  $\Omega/\square$  for both bottom and top electrodes (figure 4.12 (b)). This mechanically stable and robust hybridized Ag NW-SWCNT is adequate as an electrode for practical bending motion sensor system.



Since the bending motion sensor is required to be bendable in large incurvation state without any cracks or deformation, the entire consisted layers in the integrated device should be all flexible. The Ag NW electrode is eligible because of the favorable properties of flexibility. This Ag NW electrode can be highly conductive under bending process as it formed network junctions between the NWs. These networks between Ag NWs are of critical importance for efficient electron transfer. In this point of view, the Ag NW electrode can maintain the electrical conductivity under bending conditions

Moreover, to reinforce the flexibility at larger incurvation of Ag NW electrode, the single wall carbon nanotube contents were added and filled the junction gaps between the Ag NWs. In actual test, the 7:3 (g:g) of 0.5 wt% Ag NW : 1.3 wt% SWCNT hybridized electrodes compared to less SWCNT contained Ag NW electrodes showed better mechanical endurance during the bending process Since the SWCNT contents filled the vacant room between the Ag NWs, the Ag NW networks became tightly connected. As the wire-wire contact became tighter and stronger, lower sheet resistance were measured under bending motions with hybridized Ag NW-SWCNT electrode. However, bending process of the 9:1 and 8:2 of (g:g) of 0.5 wt% Ag NW : 1.3 wt% SWCNT hybridized electrodes led dislocation of the contact points with the absence of SWCNT, leading to mechanical cracks. Therefore, for harsh bending conditions, the hybrid electrode of Ag NW-SWCNT was essential in bending motion sensor system.

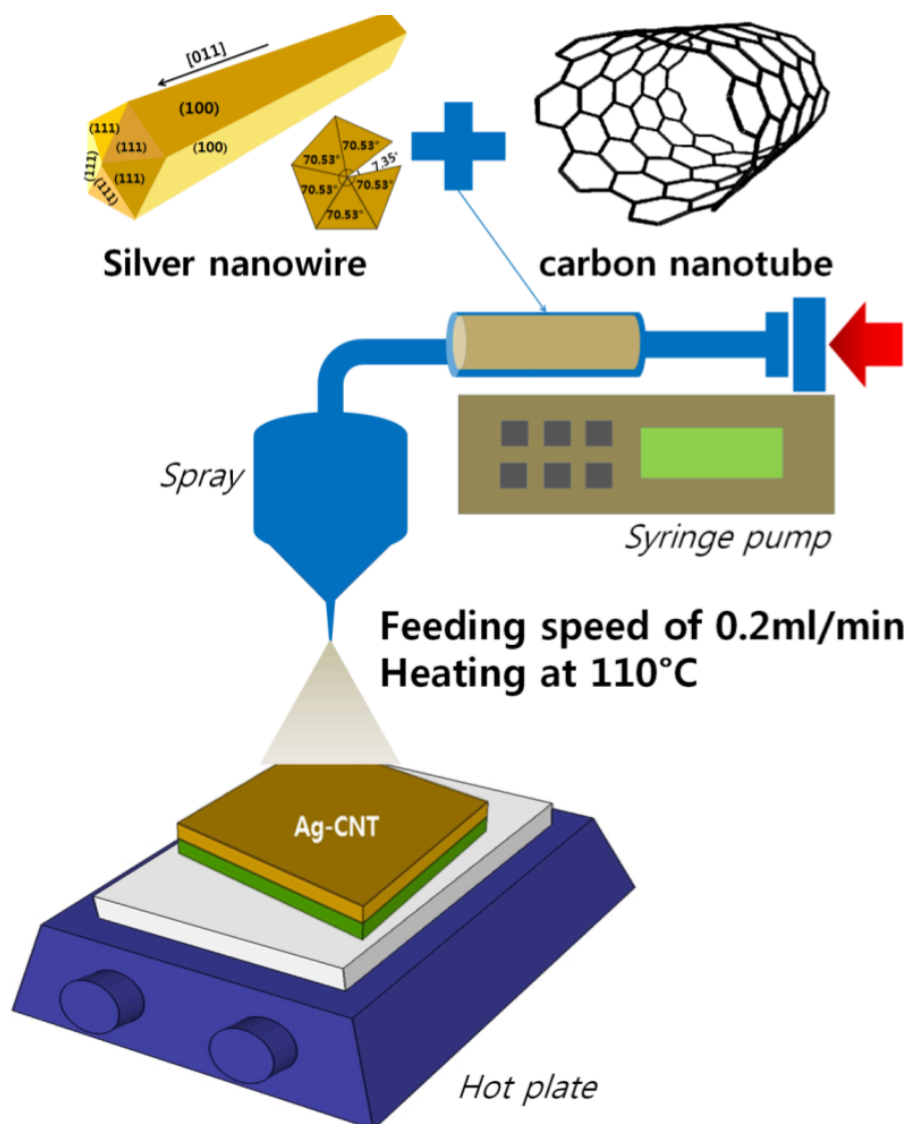


**Figure 4.7** Customized spray-coating setup for Ag NW-SWCNT composite film. The Ag NW-SWCNT solution was injected at feeding rate of 0.2 ml/min with an air pressure of 2 bar onto the UVO-treated PET films for 5 min, annealing at 100 °C.

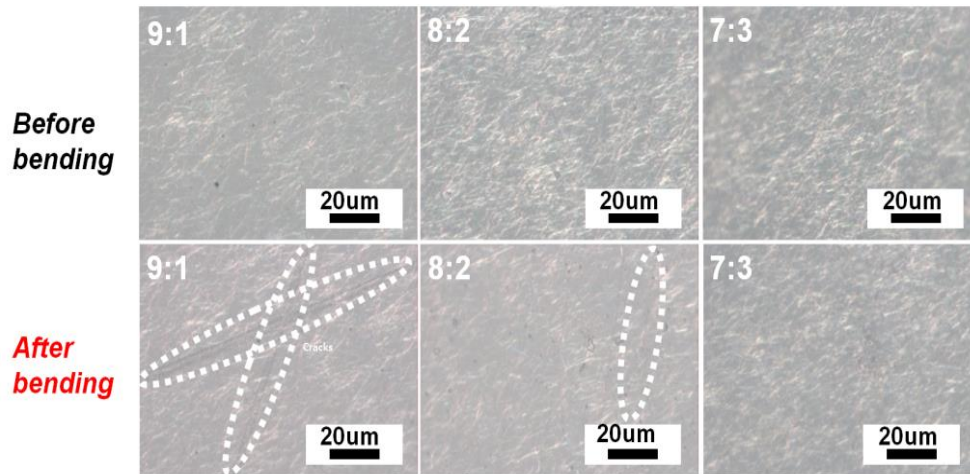


**Figure 4.8** 9:1, 8:2, 7:3 (g : g) of 0.05 wt% Ag NWs and g of 1.3 wt% SWCNT were mixed to investigate any deformation or cracks before and after mechanical bending. Optical microscope images of bottom electrodes according to the different weight ratio of Ag NW-SWCNT.

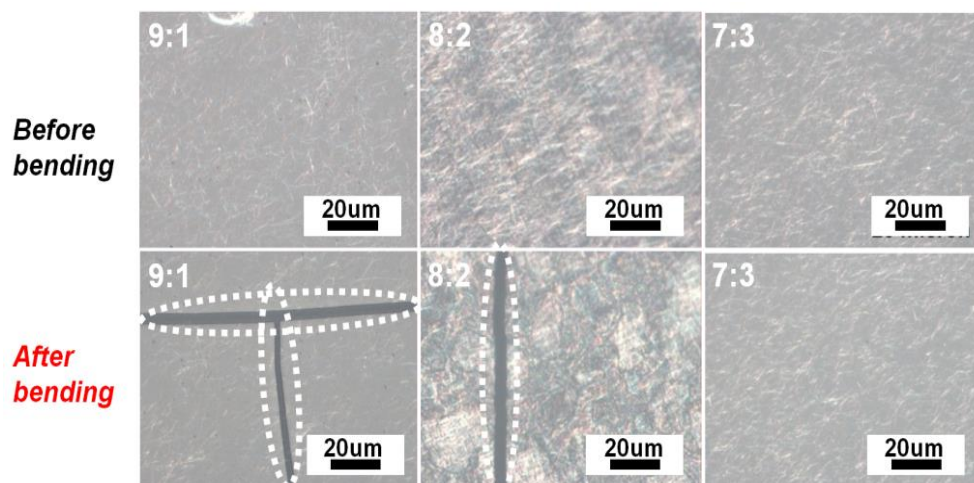


**Figure 4.9** 9:1, 8:2, 7:3 (g : g) of 0.05 wt% Ag NWs and g of 1.3 wt% SWCNT were mixed to investigate any deformation or cracks before and after mechanical bending. Optical microscope images of top electrodes according to the different weight ratio of Ag NW-SWCNT.

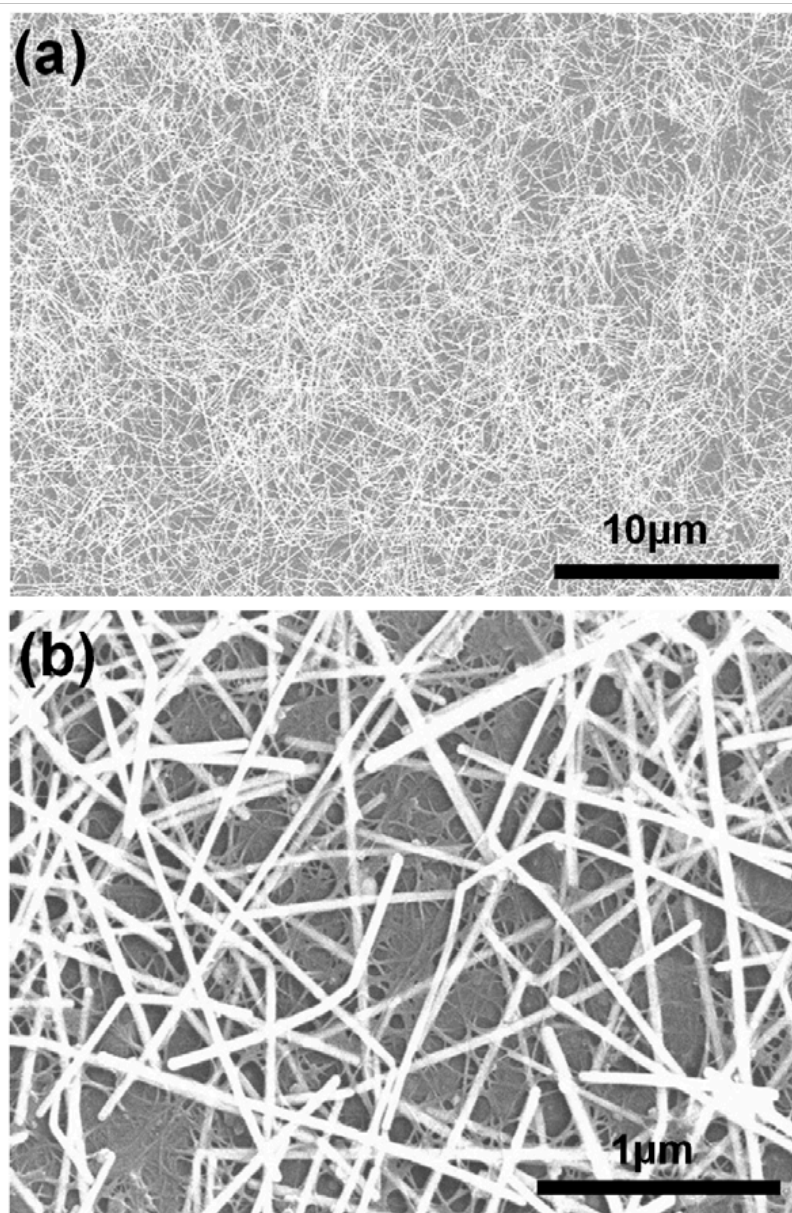


**Figure 4.10** (a) FE-SEM image of uniformly spray-coated Ag NW-SWCNT. (b) Magnified FE-SEM image of the Ag NW-SWCNT.

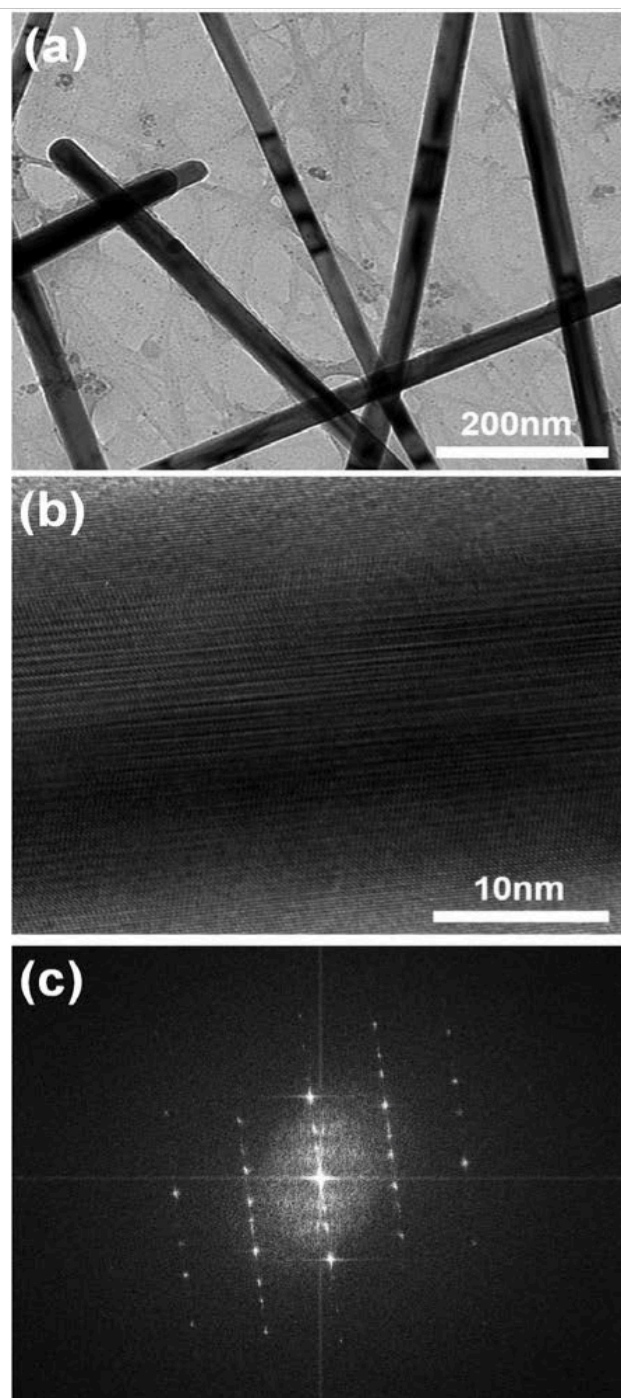


**Figure 4.11** (a) HRSTEM image of spray-coated Ag NW-SWCNT (b) The crsytalline lattice of Ag NW-SWCNT in its central region and (c) its FFT patterns.



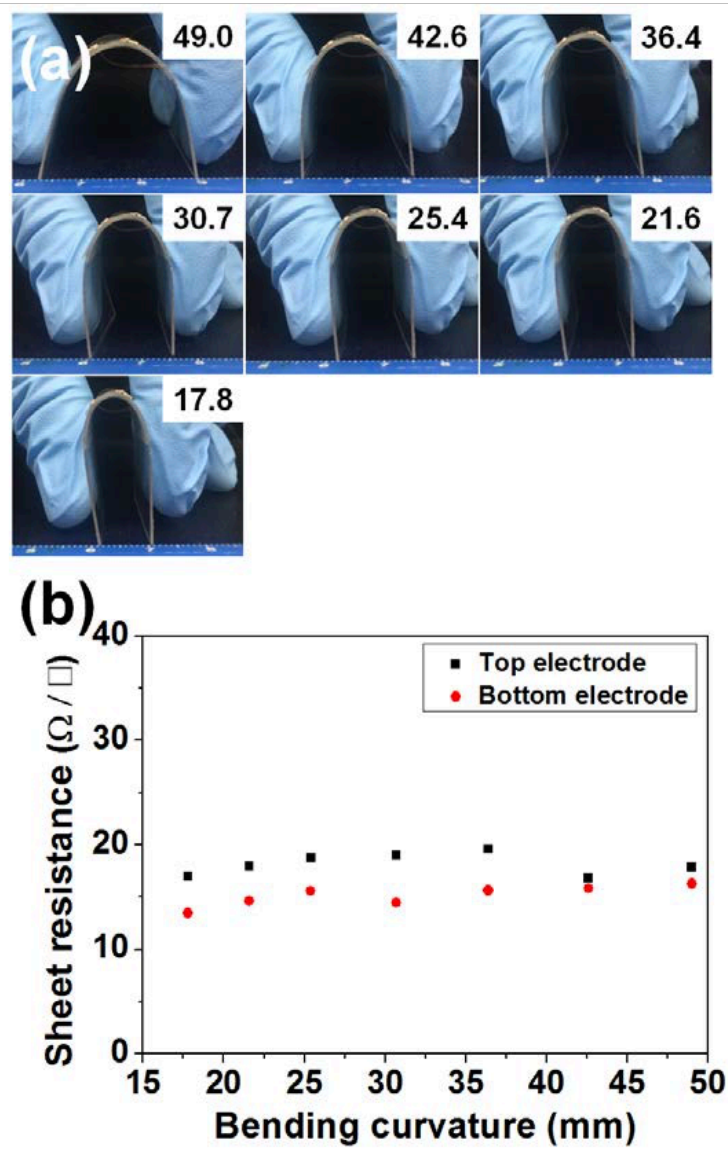


**Figure 4.12** (a) Differently applied bending curvature. (b) Sheet resistance of top and bottom electrodes as a function of bending curvature.

### 4.3.3 Measurement of output voltage signals

The standard output voltage signals were measured as shown in figure 4.13. The measurement condition for the standard output was set in bending curvature of 17.8 mm and speed of 150 mm/sec. As previous shown in figure 4.12 (a), conditions for the bending curvature is separated as 49.0, 42.6, 36.4, 30.7, 25.4, 21.6 and 17.8 mm. The bending speed was also divided into five values with reduction of 20 mm/sec from the maximum value of 150 mm/sec, 150, 130, 110, 90 and 70 mm/sec each. However, performance of the piezoelectric bending motion sensor under bending speed lower than 70 mm/sec had difficulty in classification of the output signals because too slow bending operation vanished the part of piezoelectric potential generation. Figure 4.14 show the output performance of piezoelectric bending motion sensor according to different bending speed and curvature at constant bending curvature and speed. At constant bending curvature of 17.8 mm, the output voltages were measured according to the bending speed as shown in figure 4.14 (a). From the graph, it is notable that the bending speed is a factor deciding the peak voltages of output power. At constant bending speed of 150 mm/sec, the peak voltage was increased with decreasing bending curvature (more bending incurvation in smaller value of bending curvature) (figure 4.14 (b)). However, the area of output voltages was also increased with decreasing bending curvature. This indicates that the voltage area is a factor depending on the value of bending curvature. Accordingly, the applied bending curvature across the piezoelectric bending motion sensor affects both the voltage peak and area and therefore, the output performance is needed to be considered in aspects of voltage area not only in voltage peak. Accordingly, if the voltage area according to the bending curvature



and speed is presented respectively, the correlation between these factors will be enabled to be ratiocinated. Therefore, the voltage area was calculated and presented as a function of applied bending curvature and speed. The values of voltage area were positively transformed in case of negative output voltage peaks. In this report, concave bending was applied to the piezoelectric bending motion sensor and therefore negative output voltages were initially measured during the bending motion, otherwise positive values were reversely examined during release motion. Since only bending motions was considered in whole bending and release motions for the applicability of both bending and release modes, the values of voltage area for bending motion were all transformed to positive one in case of the concave bending.

To verify that the electrical outputs were generated by piezoelectric properties of ZnO NRs, non-ZnO NRs contained PDMS and Ag NW-SWCNT bending device was taken into an experiment (figure 4.15). The output voltage shown by the non-ZnO NR bending device (figure 4.15 (b)) was only noise level, indicating that the output signals came from the piezoelectric effect of the ZnO NRs. However, the small possibility for the friction between the PDMS layers was also observed as a result of the output measurement.

Meanwhile, for the confirmation of PDMS thickness effect, experimental in accordance with different weight ratio of PDMS solution (PDMS : hexane) was conducted. The PDMS : hexane solution were mixed in ratio of 5:5, 6:4 and 7:3wt% to obtain different thickness of PDMS layer. The thickness of each device for 5:5, 6:4 and 7:3 (wt %) was 25.3, 32.0 and 39.0  $\mu\text{m}$  as shown in FE-SEM images of figure 4.16 (a-c). The output voltages were measured using an oscilloscope to find out how the thickness of PDMS layer affects the output performance of the

piezoelectric bending motion sensor. As a result, the voltage height of the bending motion sensors were 0.029, 0.0149, 0.012 V each with weight ratio of 5:5, 6:4 and 7:3 (figure 4.16 (d-f)). Therefore, the thinner PDMS : hexane layered piezoelectric bending motion sensor has better output characteristics compared to the 6:4 and 7:3 of thicker piezoelectric devices. The weight ratio less than 50% of PDMS based devices were also fabricated, but had short-circuit problem because of its thin PDMS layer. The effect of thickness of PDMS solution was plotted as a function of voltage height as shown in figure 4.17. Therefore, the weight ratio of 5:5 of PDMS solution (PDMS : hexane) was selected as a composite layer as well as a platform for the rubbing substrate of ZnO NRs.

The total thickness of the piezoelectric bending motion sensor was measured. From the FE-SEM image, ZnO monolayer is about 0.3  $\mu\text{m}$  which coincides well with the diameter of ZnO NRs (373.5 nm). However, the two bottom and top spray-coated electrodes were under 100nm thin and the PET film was 130  $\mu\text{m}$  thick. Therefore the total thickness of the device was  $\sim 155.5 \mu\text{m}$ .

Finally, the measurement was attempted with five different bending motion sensors at the same experimental conditions in each case for accuracy. In addition, to secure the reliability of piezoelectric bending motion sensor, measurement of the output performance was conducted for every 1000 times during 4000 times bending motions of the piezoelectric sensor to insure the constant power generation (figure 4.18).

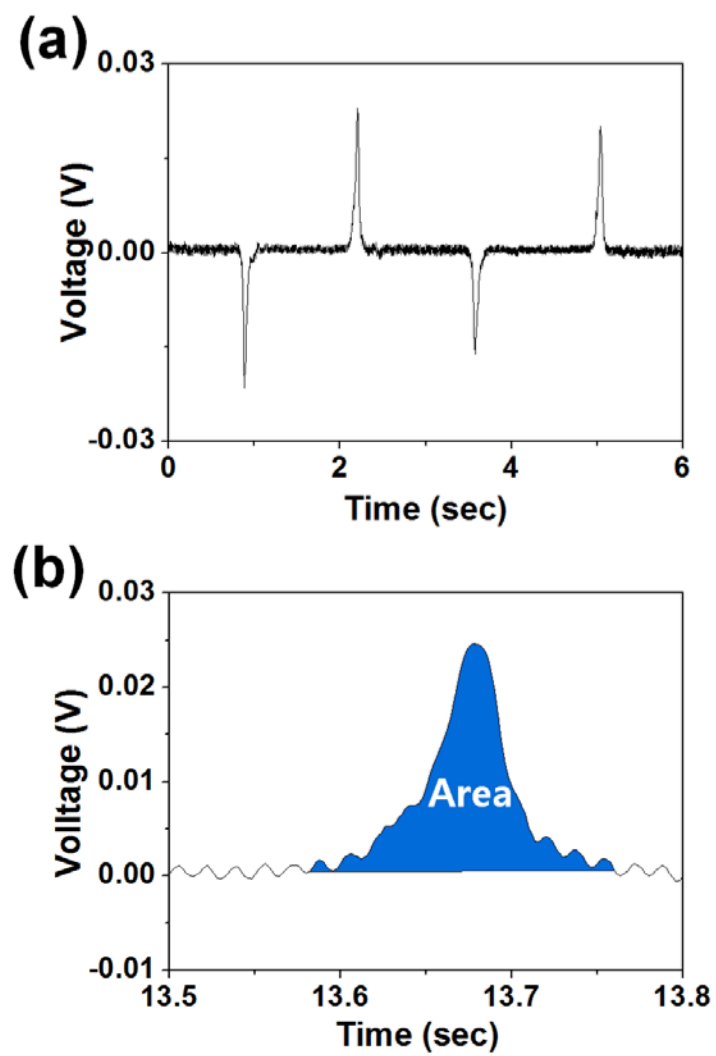


**Figure 4.13** (a) Standard output voltage. (b) Definition of a voltage area.

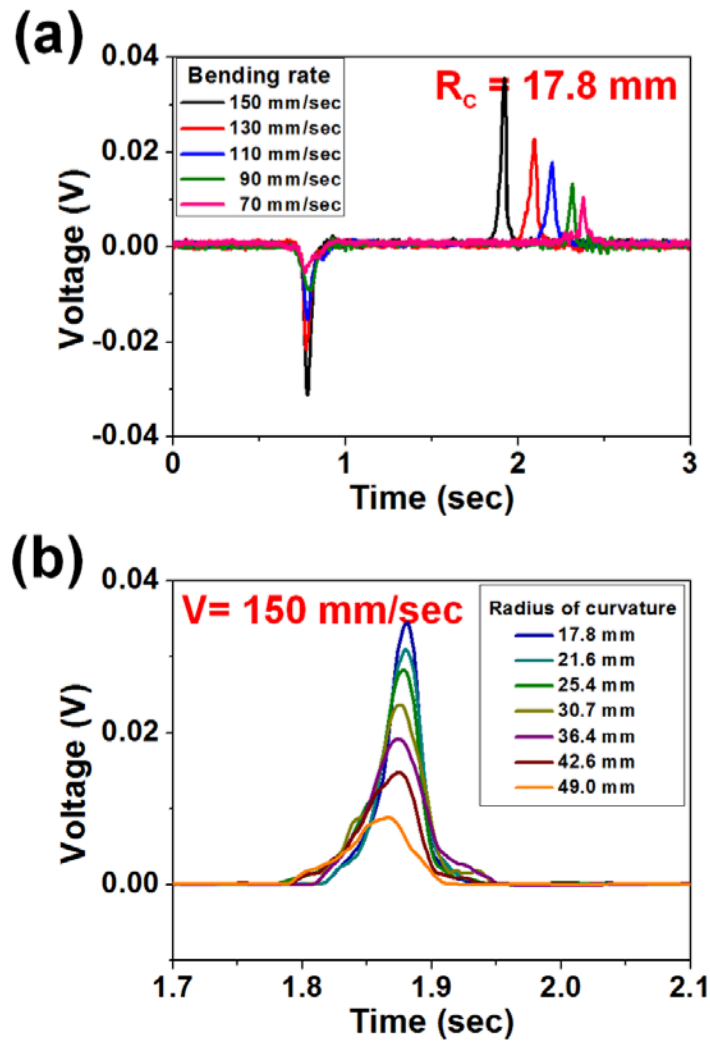


**Figure 4.14** The output voltages of the piezoelectric bending motion sensor with (b) different bending speed at constant bending curvature and with (c) different bending curvature at constant bending speed.

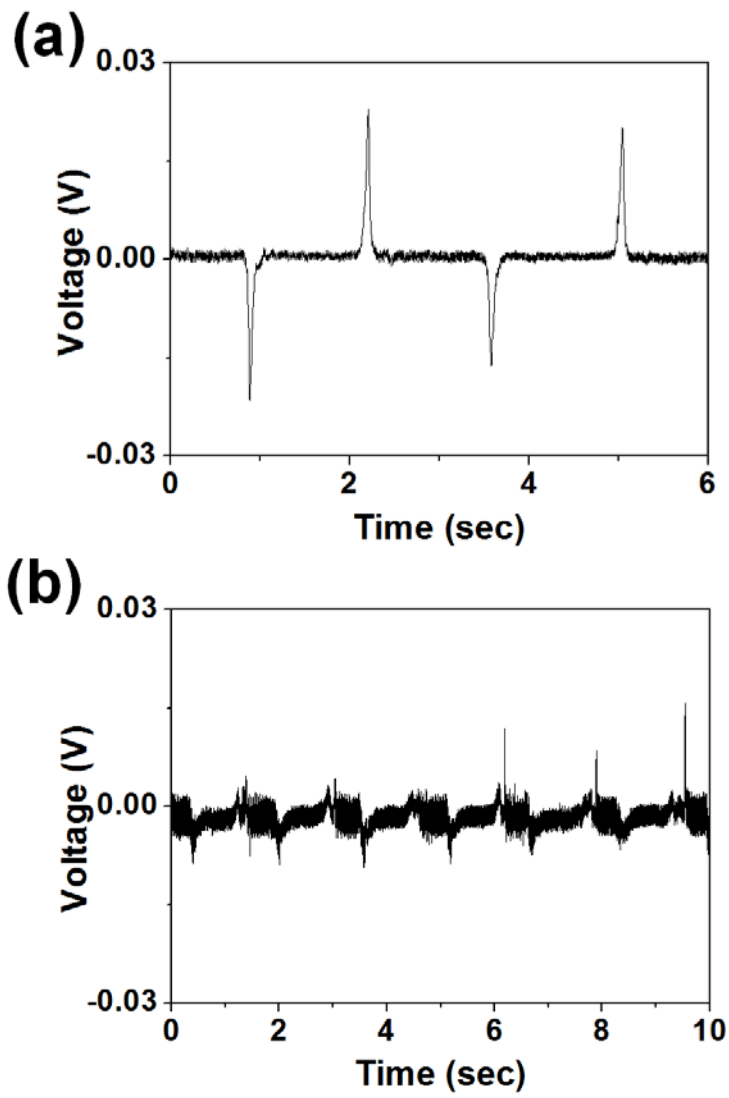


**Figure 4.15** The output voltages of the piezoelectric bending motion sensor with (b) different bending speed at constant bending curvature and with (c) different bending curvature at constant bending speed.

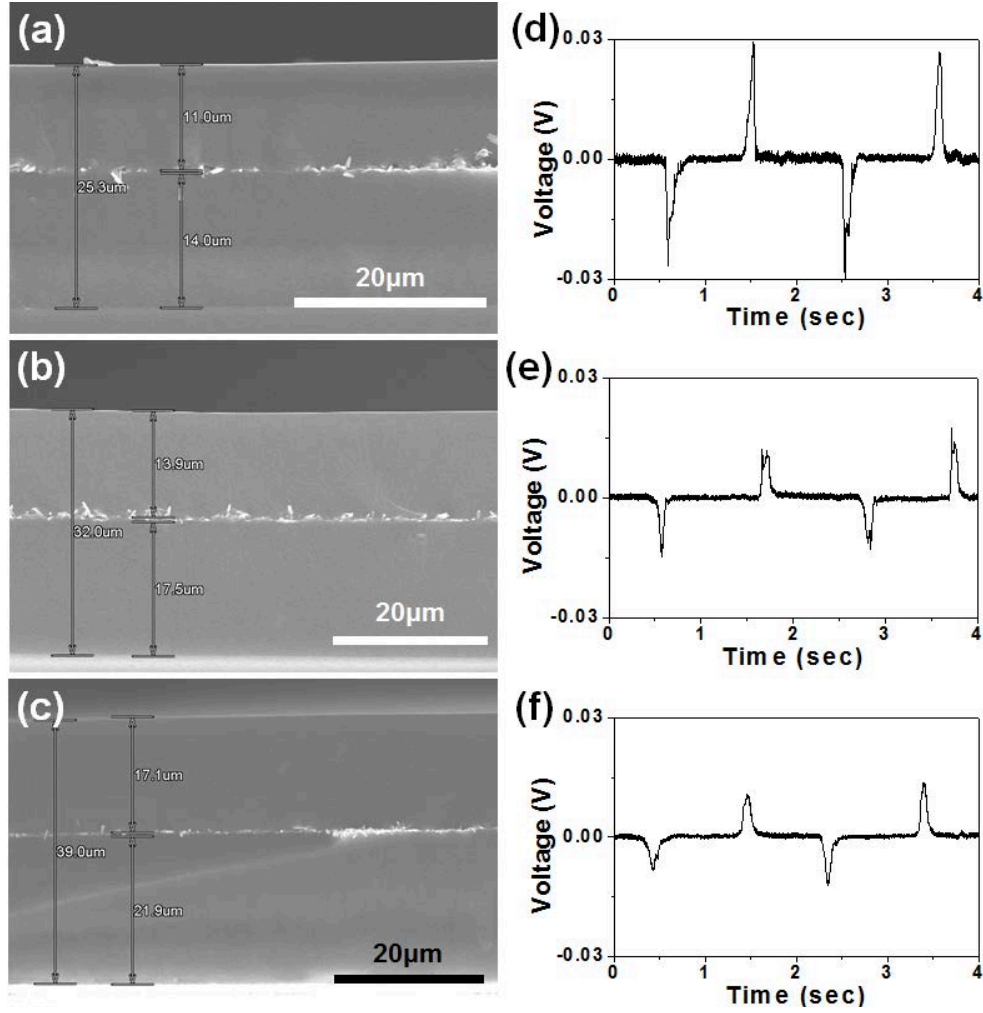


**Figure 4.16** Thickness of PDMS-ZnO NRs sandwiched structure with different weight ratio of 5:5, 6:4 and 7:3 of PDMS : hexane. Total thickness of the PDMS-ZnO NRs was 25.3, 32 and 39  $\mu\text{m}$  each.

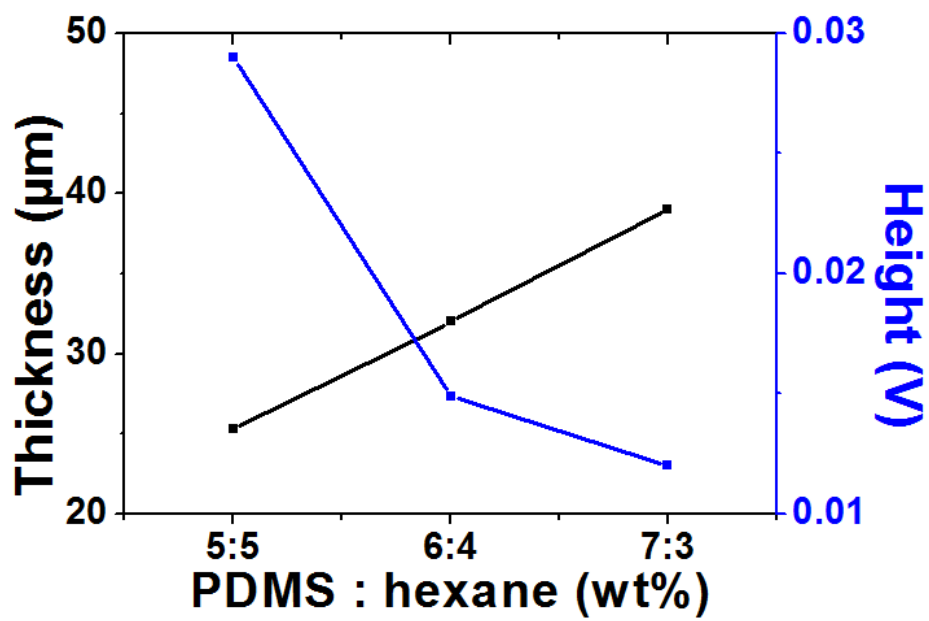


**Figure 4.17** Thickness and voltage height of the piezoelectric bending motion sensor with different weight ratio (5:5, 6:4 and 7:3) of PDMS : hexane solution.

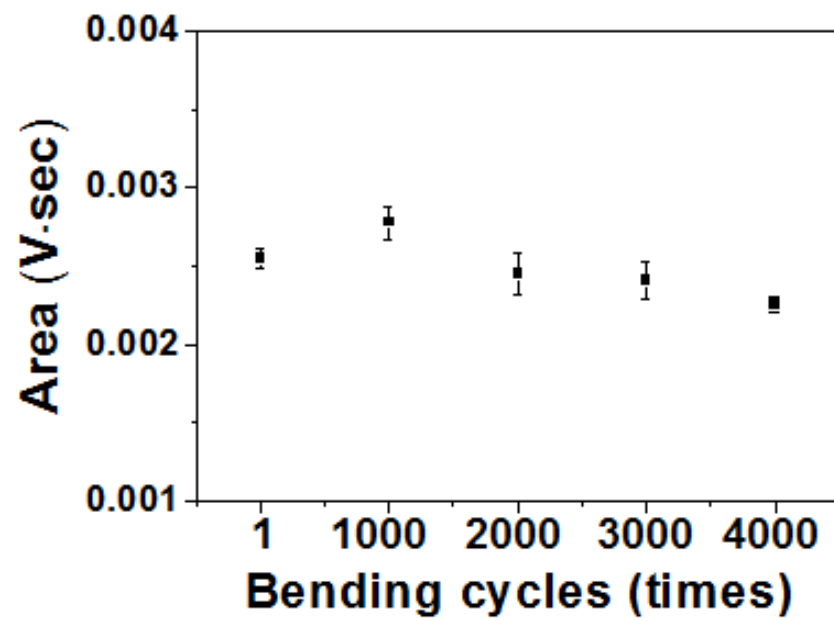


**Figure 4.18** The voltage area of the piezoelectric bending motion sensor measured at every 1000 times for 4000 times.



### 4.3.4 Output analysis based on piezoelectric effect

The values of voltage area as a function of bending curvature and rate ( $dR_c/dt$ ) were presented in figure 4.19 (a) and (b). The relative bending rate for bending of piezoelectric motion sensor can be calculated as

$$\frac{dR}{dt} = \frac{df(L)}{dL} \cdot \frac{dL}{dt} = \frac{\Delta f(L)}{\Delta L} \cdot \frac{dL}{dt} = \frac{\Delta R}{\Delta L} \cdot \frac{dL}{dt} \quad (1)$$

where  $\Delta R$  and  $\Delta L$  are the change of radius and length of the piezoelectric bending motion sensor as the bending curvatures were applied and  $dL/dt$  is the bending speed. Hence, all the bending modes of the piezoelectric sensor have different bending rates although the applied bending speed is the same. This bending rate was used to consider the change of bending curvature according to the length change of the piezoelectric bending motion sensor. In figure 4.19 (a), the values of voltage area have a tendency to be decreased with increasing bending curvature and reduced with bending speed. However, from figure 4.19 (b), linearly increased values of voltage area were observed through the increase of bending rate in one specific value of bending curvature. This indicates increase in bending rates of the piezoelectric sensors made increase in values of voltage area. The physical meaning of voltage area is an absolute integration value of voltage peaks. Thus, the area of voltage can be expressed as

$$\text{Area of voltage} = \int_0^t V(t) dt \quad (\Delta t = t - 0) \quad (2)$$

where the  $\Delta t$  is the interval of integration meaning the bending process time. Thus, the average voltage is able to be expressed as an equation as follows.

$$V_{avg} = \frac{1}{\Delta t} \int_0^t V(t) dt = \int_0^t \frac{q(t)}{c} dt = \frac{Q_{avg}}{c} \quad (3)$$

Accordingly, the integration value of piezoelectric charge over capacitance indicates the average charge generated by the external bending motion of the

piezoelectric sensor over capacitance. Therefore, since the capacitance value is consistent, the generated charge is proportional to the voltage area value.

Generally, an area of voltage signals is consistent with piezoelectric charges and charges are dependent on bending curvature. In other words, under the same applied bending curvature, the peak area values should be the same. However, discrepancy in voltage area value at the same bending curvature under different bending speed was observed. This discordance in piezoelectric charge values is attributed to resistor-capacitor (RC) time constant, which allows charge leakage during bending operations in case of different bending speed conditions. Since more leakages in piezoelectric charges occurred in mode of slower bending speed of the piezoelectric units, the resultant piezoelectric charges, which can be substituted to the area values were smaller. This theory is fundamentally based on a piezoelectric effect,

$$\dot{q} = d_{33}EA\varepsilon \quad (4)$$

where  $\dot{q}$  is the piezoelectric charge divided by period of time,  $d_{33}$  is the piezoelectric charge constant,  $\varepsilon$  is the bending speed, and E, A are the Young's modulus and the applied area each.<sup>21</sup> Therefore, the absolute area values of output voltages also change with applied bending speed across the piezoelectric bending motion sensor. Due to this reason, the piezoelectric output performance is needed to be analyzed in consideration of bending speed as well as the bending curvature for accurate sensing system. Based on this theory, our group actually tested the piezoelectric bending motion sensor via simultaneous observation of bending curvature and speed and verified that the database of the voltage area values was somewhat consistent according bending curvature and speed.

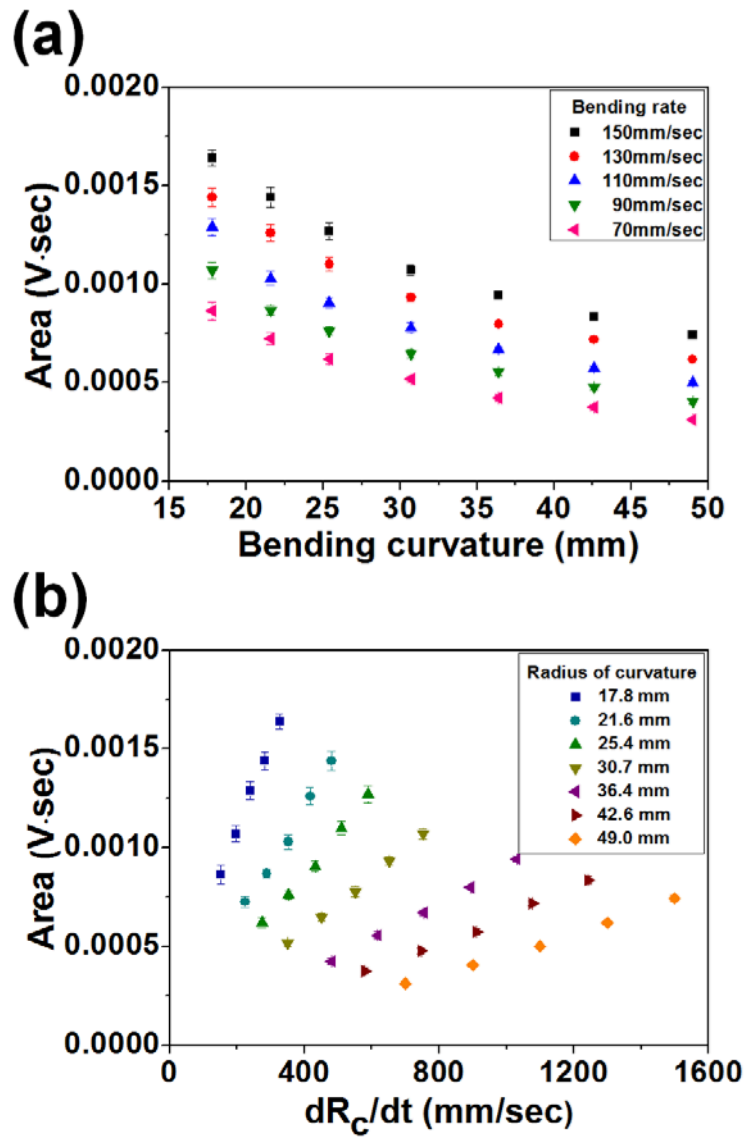


**Figure 4.19** The voltage area according to (d) the bending curvature and (e) rate ( $dR_c/dt$ ) according to the different bending speed and curvature.

### 4.3.5 Sensing of bending curvature and speed

The strategy for detection of bending motions is shown in figure 4.20. Firstly, measurement of output voltages across the piezoelectric bending motion sensor is needed to be conducted. Secondly, calculation of voltage area is required and the area values are needed to be indicated in graphs, which display x versus y values as bending curvature or bending rate versus voltage area. Finally, collation of the original database from the statistical measurement of output performance with experimental data is needed to be conducted to find out the values of bending curvature and speed.

Practically, the piezoelectric bending motion sensors experienced finger bending with random bending curvatures and speeds among the experimental conditions set-up. The output voltages were measured using an oscilloscope as can be seen in figure 4.21 (a-c). From the calculation of voltage area based on values of output voltage across the piezoelectric bending motion sensor, the experimental data of voltage area was presented. The information of bending rate from the graph of bending curvature versus voltage area, and bending curvature from the graph of bending rate versus voltage area was able to be obtained. For example, the voltage area value, 0.001665 V·sec was obtained and the 0.00167 V·sec for bending curvature of 17.8 mm and bending speed 150 mm/sec from the database of the output performance was almost the same. Therefore, from the voltage area value, the bending curvature and speed for figure 4.21 (a) could be speculated, which were 17.8 mm and 150 mm/sec. However, due to the small scale of the database, the random bending curvature and speed were restricted to several values only. Accordingly, diverse range of bending curvature and speed values from

experimental set-up is required for the future study. Continuously, the another point of voltage area value was 0.001078 V·sec which coincided with voltage area value of 0.00107 V·sec for bending curvature of 30.7 mm and bending speed of 150 mm/sec from the database as shown in figure 4.21 (d) and (e). Finally, bending curvature and speed of 49 mm and 90 mm/sec for voltage area value of 0.000485 V·sec from the database and experimental value of 0.000478 V·sec were found to be almost identical. As a result, the bending curvature and speed for figure 4.21 (b) and (c) were 30.7 mm & 150 mm/sec and 17.8 mm & 90 mm/sec. Actually, the applied bending curvatures were measured from the photographs of piezoelectric sensors during bending operation and the values were about 49, 31 and 18 mm each. Hence, the applied bending curvatures were good accordance with the speculated bending curvatures. Therefore, under specific conditions of bending curvatures and speeds of the piezoelectric sensor, the bending motions are predictable from the simple correlation of voltage area and bending curvature and speed. Beyond presenting the output results according only by different bending curvatures, this result discerned the bending curvature and speed in simultaneous manner for perspicacious analysis, which was based on the theory of piezoelectric effect.

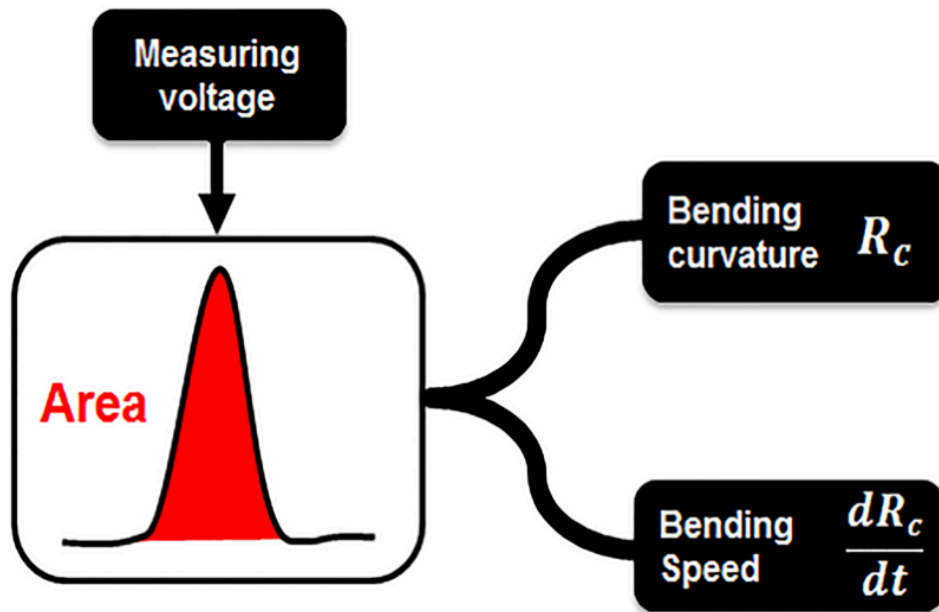


**Figure 4.20** Diagram for detection of bending curvature and speed by measuring the voltage area from bending motion of the piezoelectric sensor.

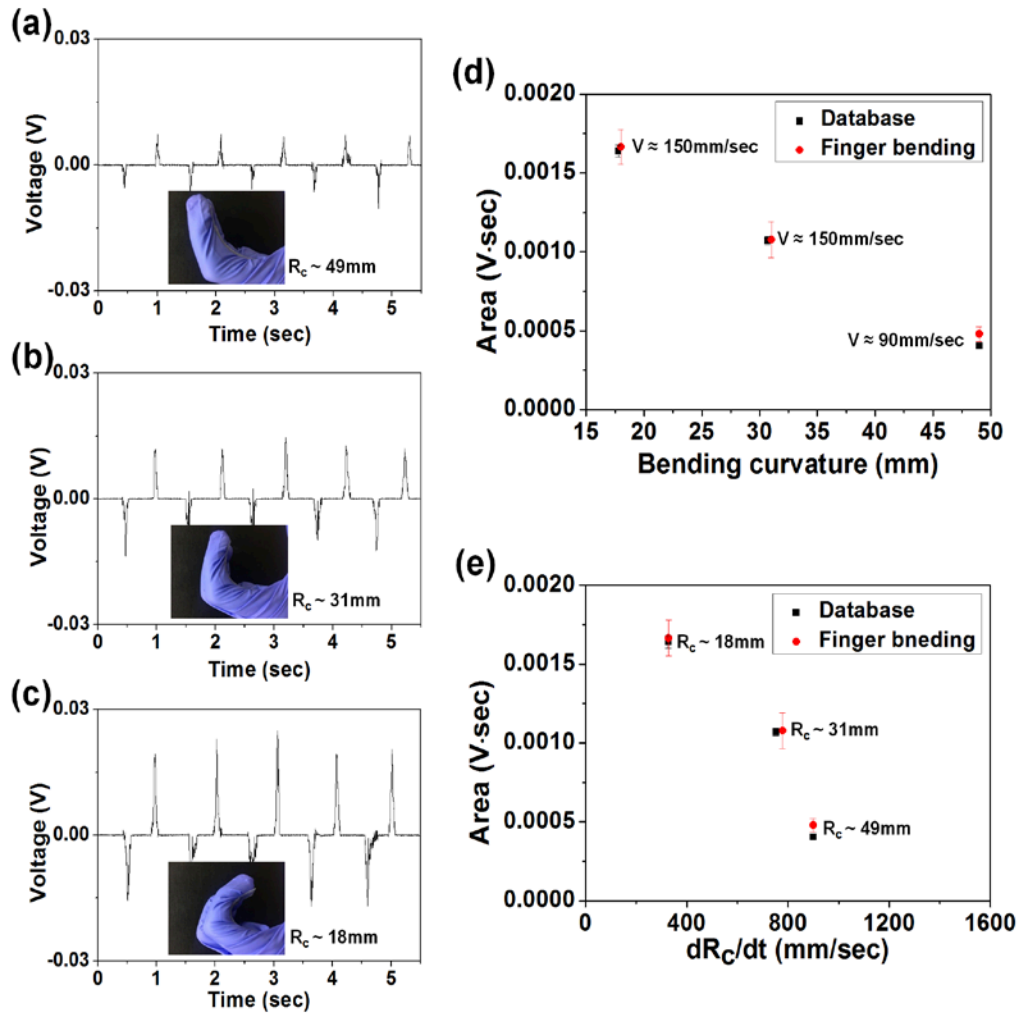


**Figure 4.21** (a-c) Output voltages of the piezoelectric bending motion sensor by finger bending with various bending curvature and speed. Voltage areas according to (d) the bending curvature and (e) rate ( $dR_c/dt$ ) for detection of bending speed and curvature.

## 4.4 References

- [1] D. -H. Kim, N. Lu, R. Ma, Y. -S. Kim, R. -H. Kim, S. Wang, J. Wu, S. M. Won, H. Tao, A. Islam, K. J. Yu, T. Kim, R. Chowdhury, M. Ying, L. Xu, M. Li, H. -J. Chung, H. Keum, M. McCormick, P. Liu, Y. -W. Zhang, F. G. Omenetto, Y. Huang , T. Coleman, J. A. Rogers, *Science* **2011**, 333, .838.
- [2] Y. Khan, A. E. Ostfeld, C.M. Lochner, A. Pierre, A. C. Arias, *Adv. Mater.* **2016**, 28, 4373.
- [3] G. Schwartz, B. C. -K. Tee, J. Mei, A. L. Appleton, D. H. Kim, H. Wang, Z. Bao, *Nat. Commun.* **2013**, 4, 1859.
- [4] F. Ilievski, A. D. Mazzeo, R. F. Shepherd, X. Chen, G. M. Whitesides, *Angew. Chem Int. Ed.* **2011**, 50, 1890.
- [5] T. Yamada, Y. Hayamizu, Y. Yamamoto, Y. Yomogida, A. I. -Najafabadi, D. N. Futaba, K. Hata, *Nature Nanotech.* **2011**, 6, .296.
- [6] C. Pang, G. -Y. Lee, T. Kim, S. M. Kim, H. N. Kim, S. -H. Ahn, K. -Y. Suh, *Nat. Mater.* **2012**, 11, 795.
- [7] J. Park, Y. Lee, J. Hong, Y. Lee, M. Ha, Y. Jung, H. Lim, S. Y. Kim, H. Ko, *ACS Nano* **2014**, 8, 12020.
- [8] S. Gong, D. T. H. Lai, B. Su, K. J. Si, Z. Ma, L. W. Yap, P. Guo, W. Cheng *Adv. Electron. Mater.* **2015**, 1, 1400063.
- [9] Y. Cheng, R. Wang, J. Sun, L. Gao, *Adv. Mater.* **2015**, 27, 7365.
- [10] M. H. G. Wichmann, S. T. Buschhorn, L. Böger, R. Adelung, K. Schulte, *Nanotechnology* **2008**, 19, 475503.
- [11] L. Cai, L. Song, P. Luan, Q. Zhang, N. Zhang, Q. Gao, D. Zhao, X. Zhang, M. Tu, F. Yang, W. Zhou, Q. Fan, J. Luo, W. Zhou, P. M. Ajayan, S. Xie, *Sci. Rep.*



**2013**, 3, 3048.

- [12] J. -S. Heo, J. -H. Chung, J. -J. Lee, *Sensor Actuat. A-phys.* **2006**, 126, 312.
- [13] M. Ramuz, B. C. -K. Tee, J. B. -H. Tok, Z. Bao, *Adv. Mater.* **2012**, 24, 3223.
- [14] J. Chun, N. -R, Kang, J. -Y Kim, M. -S. Noh, C. -Y. Kang, D. Choi, S. -W, Kim, Z. L. Wang, J. M. Baik, *Nano Energy* **2015**, 11, 1.
- [15] E. S. Nour, C. O. Chey, M. Willander, O. Nur, *Nanotechnology* **2015**, 26, 095502.
- [16] C. Chang, V. H. Tran, J. Wang, Y. -K. Fuh, L. Lin, *Nano Lett.* **2010**, 10, 726.
- [17] W. S. Jang, T. I. Lee, J. Y. Oh, S. H. Hwang, S. W. Shon, D. H. Kim, Y. Xia, J. M. Myoung, H. K. Baik, *J. Mater. Chem.* **2012**, 22, 20719.
- [18] T. I. Lee, W. S. Jang, E. Lee, Y. S. Kim, Z. L. Wang, H. K. Baik, J. M. Myoung, *Energy Environ. Sci.* **2014**, 7, 3994.
- [19] X. Hou, L. Wang, G. He, J. Hao, *Cryst. Eng. Comm.* **2012**, 14, 5158.
- [20] J. Lee, J. Y. Woo, J. T. Kim, B. Y. Lee, C. -S. Han, *ACS Appl. Mater. Inter.* **2014**, 6, 10974.
- [21] J. Sirohi, I. Chopra, *J. Intell. Mater. Syst. Struct.* **2000**, 11, 246.

## Chapter 5. Conclusion

In conclusion, simple solution-processed piezoelectric materials were suggested and adopted beyond the cumbersome high-temperature, vacuum processed piezoelectric active materials. Through simple process of ZnO nanomaterials, new ultra-flexible self-powered piezoelectric patches and sensors were suggested.

First, we have demonstrated an all-solution-processed flexible thin film PENG in a plastic substrate. The simple reactive zinc hydroxo-condensation process was adopted to fabricate the solution-processed ZnO thin film and the screen-printing method of the silver electrode was conducted for the flexible electrode. The solution-based method provides a simple and low-cost process. The polycrystalline ZnO thin film with the tendency for c-axis orientation was detected in several characterizations, indicating that the operational mechanism of our PENG can be explained via the inductance of the piezoelectrical potential through the whole layers of the PENG by the crystalline phase of ZnO thin film. The highly elastic thin film allowed the piezoelectric energy to be generated through the mechanical rolling and muscle stretching of the piezoelectric unit. In addition, the mechanically stable piezoelectric thin film is appropriate for the long-term energy generation from the rolling motion of the nanounit. This flexible all solution-processed PENG is promising for use in future energy harvesters such as wearable human patches and mobile electronics.

Second, a piezoelectric bending motion sensor to determine simultaneously bending curvature and speed from random bending motions has been developed via ratiocinative algorithm system. The standardization of the bending motion output signals through simultaneous detection of bending curvature and speed within the

piezoelectric bending motion sensors was an effective way for establishment of the algorithm system. From the algorithm tracking of random external stimuli is available, resulting in recognition of bending motion values with high accuracy. Moreover, high elasticity of the piezoelectric bending motion sensor is attributed to the flexible element of piezoelectric composite material of ZnO NR-PDMS and hybrid Ag NW-SWCNT electrode. Therefore, the reciprocal set-up of piezoelectric bending motion sensor : algorithm is expectable to be a standard sensing methodology for any piezoelectric elements with self-powered active system.

In summary, solution-processed ZnO nanomaterials adapted piezoelectric devices could be demonstrated with ultra-flexible configuration in self-powered active system. The piezoelectric patches and sensors can be structural elements for integration into nanosystem. Therefore, lots of applications such as wearable human patches, artificial skins and nanorobotic sensor system can be the candidate for these piezoelectric devices.

## 국문초록

# 용액 공정 산화아연 나노물질 자가 발전 압전 유연 패치 및 센서의 제작 및 분석

정성운

융합과학부

융합과학기술대학원

서울대학교

세계적으로 에너지 자원 고갈 및 온난화 현상이 발생하면서 최근 과학분야에서는 재생 그린 에너지 연구에 대한 관심이 급증하고 있다. 대규모적으로는 석유, 석탄, 천연가스, 수력발전, 원자력 발전이 현재 전세계적으로 잘 알려진 에너지 원으로서 에너지 고갈로 인한 심각한 위기에 처해 있다. 한편 대체 에너지로서 태양, 풍력, 지열, 수소, 바이오매스 등의 에너지의 개발이 활발히 이루어지고 있다. 한편, 전체 패키지가 나노크기를 요구하는 매우 작은 소규모의 나노 에너지 시스템은 개인 휴대용 전자 장비, 마이크로 전자 기계 시스템 (MEMS), 나노로봇, 인체 삽입형 소자 등에 응용될 수 있을 것으로 보인다. 따라서 배터리 없이 영구적으로 사용 가능하면서도 휴대가 가능하며 가벼운 소자 제작을

위해 서는 에너지 하베스팅과 센서 기술에 자가발전 시스템의 도입이 필수불가결하다. 이러한 관점에서, 무선 및 휴대용 전자 장비의 세계적으로 에너지 자원 고갈 및 온난화 현상이 발생하면서 최근 과학분야에서는 재생 그린 구동을 위해서는 압전 나노 소자가 근본적인 해결책이 될 수 있다.

압전 나노소자는 기계적 에너지를 전기로 바꾸는 소자로서 주변 환경에서 버려지는 에너지를 활용할 수 있는 점 때문에 최근 에너지 연구분야에서 각광받고 있다. 이러한 압전 에너지 전환 원리를 차용하는 것은 미래 에너지 자원의 새로운 형태로서 유망하다고 전망된다. 첫 번째 압전소자는 2006년 Zhong lin wang 그룹에 의해 산화아연 나노선을 이용한 소자의 구현을 통해 개발되었다. 산화아연은 압전과 반도체의 두가지 효과를 나타내면서 높은 유연성, 다양한 나노구조의 구현, 투명함과 생물학적으로 무해하다는 특징을 가지고 있다. 그러나 산화아연 나노물질의 경우 대부분 기상-액상-고상 성장법이나 스퍼터링을 통해 진공공정으로 합성되는데 이는 고비용과 복잡한 장비 시스템을 요구한다. 한편, 산화아연 나노물질의 용액공정은 간단하고 저비용, 대면적, 대량생산이 가능하다는 장점을 가지고 있다. 이러한 관점에서 용액공정으로 제작된 산화아연 나노물질을 자가발전 압전 나노소자에 적용하고 출력 성능과 압전 현상의 메커니즘을 분석하는 것을 이 연구의 목적으로 둔다.

첫째로는 용액공정으로 제작된 산화아연 박막을 이용하여 근육이나 천에 삽입

가능한 유연 압전 패치를 제작하였다. 압전 패치 또는 나노제너레이터의 전체 공정은 압전물질, 전극, 압전효율을 높이기 위한 p형 폴리머 혼합반도체를 포함하여 전 공정 모두 용액공정으로 진행되었다. 이렇게 제작된 매우 유연한 박막형 나노제너레이터는 기계적 롤링이나 사람의 근육 운동을 통해서 압전 에너지가 생산 가능하였다.

두번째로는 용액공정으로 제작된 산화아연 나노로드를 이용하여 실험을 통해 체계적으로 구축된 알고리즘을 바탕으로 한 벤딩 곡률 및 속도 동시 측정이 가능한 자가발전 압전 벤딩 모션 센서가 개발되었다. 유연성 확보를 위하여 PDMS와 산화아연 나노로드의 합성물과 은나노와이어와 단일벽탄소나노튜브의 합성전극이 차용되었다. 압전 벤딩 모션 센서와 알고리즘의 상호 구축은 자가발전을 하는 어떠한 압전소자라도 센싱이 가능한 기준방법이 될 것으로 예측된다. 요약하자면, 용액 공정으로 제작된 산화아연 나노물질을 이용하여 압전 물질이 합성되었고 이를 활용하여 자가 발전형 유연 패치나 센서를 개발하여 유용하고 저가의 나노시스템으로 구축가능한 압전 나노소자를 구현할 수 있었다.

Keywords : 산화아연, 용액 공정, 압전 나노제너레이터, 압전 센서, 자가 발전 소자, 산화아연 박막, 산화아연 나노로드, 압전패치, 벤딩 곡률 및 속도, 알고리즘

Student Number: 2010-22677